

DOKUZ EYLÜL UNIVERSITY
GRADUATE SCHOOL OF NATURAL AND APPLIED SCIENCES

SPIN - ORBIT INTERACTION IN
NANOSTRUCTURES: SPIN MANIPULATION
AND TRANSPORT



by
Bircan GİŞİ

July, 2017
İZMİR

**SPIN- ORBIT INTERACTION IN
NANOSTRUCTURES: SPIN MANIPULATION
AND TRANSPORT**

**A Thesis Submitted to the
Graduate School of Natural And Applied Sciences of Dokuz Eylül University In
Partial Fulfillment of the Requirements for the Degree of Doctor of
Philosophy in Physics**

**by
Bircan GİŞİ**

**July, 2017
İZMİR**

Ph.D. THESIS EXAMINATION RESULT FORM

We have read the thesis entitled “SPIN-ORBIT INTERACTIN IN NANOSTRUCTURES: SPIN MANIPULATION AND TRANSPORT” completed by **BİRCAN GİŞİ** under supervision of **ASSOS. PROF. DR SERPİL ŞAKİROĞLU** and we certify that in our opinion it is fully adequate, in scope and in quality, as a thesis for the degree of Doctor of Philosophy.



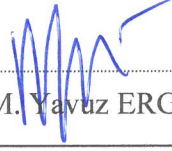
Assoc. Prof. Dr. Serpil ŞAKİROĞLU

Supervisor



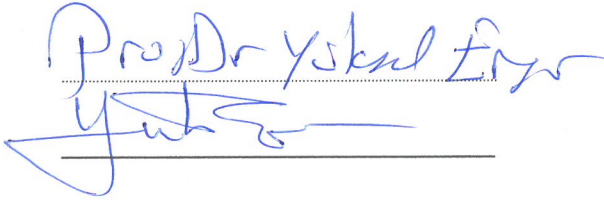
Prof. Dr. Fevzi BÜYÜKKILIÇ

Thesis Committee Member

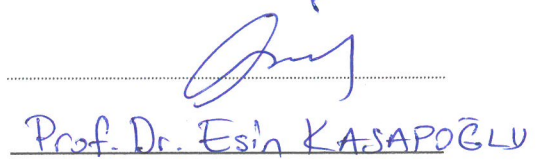


Prof. Dr. M. Yavuz ERGÜN

Thesis Committee Member



Examining Committee Member



Prof. Dr. Esin KASAPOĞLU

Examining Committee Member



Prof. Dr. Emine İlknur CÖCEN
Director
Graduate School of Natural and Applied Sciences

ACKNOWLEDGEMENTS

The work would not have been possible without the guidance and the help of several individuals who in one way or another contributed and extended their valuable assistance in the preparation and completion of this thesis.

Firstly, I wish to express my utmost gratitude to my supervisor Assoc. Prof. Dr. Serpil ŞAKİROĞLU, for her excellent guidance, endless patience during this research as well as giving me extraordinary experiences throughout the work. Above all and the most needed, she provided me unflinching encouragement and support in various ways. She exceptionally inspired and enriched my growth as a student, as a researcher and a scientist want to be. I am indebted to her more than she knows.

I gratefully acknowledge Prof. Dr. İsmail SÖKMEN for much support, excellent motivation, fruitful discussions, valuable recommendations and crucial contribution which made him a backbone of this research and so to this thesis. He shared his thorough knowledge and expertise in semiconductor and computational physics.

My thanks to go in particular to my thesis committee Prof. Dr. Doğan DEMİRHAN, Prof. Dr. Fevzi BÜYÜKKILIÇ and Prof. Dr. M. Yavuz ERGÜN for their valuable advice in science discussions, recommendations and contributions.

I would like to express my thanks to The Scientific and Technological Research Council of Turkey (TÜBİTAK BİDEB 2211) for supporting me during my thesis.

My special thanks to my peerless family. Without their love, continual encouragement and endless support this work would not have been possible. Sevcan, Canan, Çağla thank you for being my sister and thanks to Nihat for being as my brother. And I have no words to thank to my parents Sabiha and Nurettin for their unconditional love and support through out my life. And lastly my greatest thanks to my nephew Alp for being joy of living.

Bircan GİŞİ

SPIN - ORBIT INTERACTION IN NANOSTRUCTURES : SPIN MANIPULATION AND TRANSPORT

ABSTRACT

In this thesis, we investigate the effect of in-plane magnetic field onto the electronic structure, spin and magnetotransport properties of double quantum wires formed by a symmetric, double quartic-well potential taking into account Rashba and Dresselhaus spin-orbit couplings and considering the presence of electric field. The energy dispersion relation of the system is analyzed for different strengths of spin-orbit interactions, magnitude and direction of magnetic field and electric field. Our numerical results reveal that in the presence of in-plane magnetic field, the competition between spin-orbit couplings and electric field modify strongly the energy band structure, introduce a wave vector dependence to subband energies and also leads to crossings and anticrossings between subbands. This complex energy dispersion structure gives rise to the appearance of square-wave like oscillations in the conductance. The aforementioned parameters, potential profile and Fermi energy significantly affect the depth and the width of conductance steps. Moreover, we found that the competing effect between spin-orbit couplings and in-plane magnetic and electric fields leaves its marks on the spin texturing. Especially, in weak coupling limit, the electric field affects significantly spin dynamics.

Besides, we devote a part of the thesis to search ballistic conductance of quantum wire subjected to harmonic potential in the presence of Rashba and Dresselhaus spin-orbit couplings and considering various strengths and directions of an in-plane magnetic field. The conductance of a parabolic quantum wire is calculated by using transfer matrix method. The obtained results reveal that the conductance depends strongly on these internal mechanisms and external magnetic field.

Keywords: Rashba and Dresselhaus couplings, in-plane magnetic field, electric field, quantum wire, anharmonic potential

NANOYAPILARDA SPİN-YÖRÜNGE ETKİLEŞİMLERİ: SPİN MANİPÜLASYONU VE TAŞINIM

ÖZ

Bu tezde, Rashba ve Dresselhaus spin-yörünge çiftlenimleri hesaba katılarak ve elektrik alan varlığı düşünülerek simetrik, çift dördüncü dereceden kuyu potansiyeli ile oluşturulan kuantum tellerinin elektronik yapısı, spin ve manyetotransport özellikleri üzerine düzlem-içi manyetik alanın etkisini inceledik. Sistemin enerji dağılım ilişkisi farklı spin-yörünge etkileşiminin farklı büyüklükleri, manyetik alanın farklı büyüklüğü ve yönü ve farklı elektrik alan için analiz edilmiştir. Sayısal sonuçlarımız düzlem-içi manyetik alan varlığında, spin-yörünge çiftlenimleri ile elektrik alan arasındaki yarışın enerji altband yapısını güçlü bir şekilde değiştirdiğini, altband enerjilerine bir dalga vektör bağımlılığı getirdiğini ve ayrıca altbandlar arasında kesişmelere yol açmaktadır. Bu kompleks enerji dağılım yapısı iletkenlikte kare-dalga şeklinde osilasyonlar görülmesine sebep olmaktadır. Sözü geçen parametreler, potansiyel profili ve Fermi enerjisi iletkenlik basamaklarının derinliğini ve genişliğini önemli şekilde etkilemektedir. Bundan başka, spin-yörünge çiftlenimleri ile manyetik ve elektrik alan arasındaki rekabetin spin desenleri üzerinde izini bıraktığını bulduk. Özellikle, zayıf çiftlenim rejimlerinde, elektrik alan spin dinamiğini önemli şekilde etkilemektedir.

Ayrıca, tezin bir kısmını Rashba ve Dresselhaus spin-yörünge çiftlenimleri varlığında ve düzlem-içi manyetik alanın çeşitli büyüklük ve yönelimlerini düşünerek harmonik potansiyele maruz bırakılmış kuantum telinin balistik iletkenliğini araştırmaya ayırdık. Manyetik alanı farklı büyüklük ve yönelimlerini düşündük. Parabolik kuantum telinin iletkenliği transfer matris metodu kullanılarak hesaplandı. Elde edilen sonuçlar iletkenliğin bu içsel mekanizmalara ve dış manyetik alana güçlü bir şekilde bağlı olduğunu göstermiştir.

Anahtar kelimeler : Rashba ve Dresselhaus çiftlenimleri, düzlem-içi manyetik alan, elektrik alan, kuantum teli, anharmonik potansiyel

CONTENTS

	Page
THESIS EXAMINATION RESULT FORM	ii
ACKNOWLEDGEMENTS	iii
ABSTRACT	iv
ÖZ	v
LIST OF FIGURES	viii
CHAPTER ONE – INTRODUCTION	1
CHAPTER TWO – THEORETICAL BACKGROUND	5
2.1 Low-Dimensional Systems	5
2.2 Quantum Wires	7
2.3 Introduction to Spintronics	9
2.4 Spin-Orbit Interactions	10
2.4.1 Rashba Spin-Orbit Interactions	14
2.4.2 Dresselhaus Spin-Orbit Interactions	14
2.5 Effect of External Static Fields	15
2.6 Quantum Transport	17
2.6.1 Landauer-Büttiker Formalism	20
CHAPTER THREE –RESULTS AND DISCUSSIONS	25
3.1 Motivation	25
3.2 System and Its Variables	27
3.3 Numerical Results	31
3.3.1 Energy Dispersion	32
3.3.2 Spin Textures	41
3.3.3 Conductance	50

CHAPTER FOUR – CONDUCTANCE OF PARABOLIC QUANTUM WIRE 57

4.1 Formalism 57
4.2 Numerical Results 66

CHAPTER FIVE – CONCLUSIONS 74

REFERENCES 76



LIST OF FIGURES

	Page
Figure 2.1 Schematic illustration of two-dimensional electron gas which is located in the interface between two heterostructures.	6
Figure 2.2 Schematic representation of semiconductor nanostructures with reduced dimensionality: bulk semiconductor, quantum well, quantum wire and quantum dot.	7
Figure 2.3 Schematic of the system used to study electron transport.	21
Figure 2.4 Schematic illustration of the chemical potentials μ_L and μ_R , the Fermi energy E_F , the direction of the k dependent electron velocities in the bands.	23
Figure 3.1 The model of the double quantum wire structure and orientation of magnetic and electric fields.	28
Figure 3.2 The potential profile of double quantum well potential for different values of structure parameter.	31
Figure 3.3 Variation of the energy dispersion curves of electrons in a double QWR for different strength of Rashba spin-orbit interaction in the absence of magnetic/electric fields. The structural parameter is set $\tilde{\mu} = 1$. The strength of Rashba spin-orbit coupling is increased such as a) $\Delta_R = 0.01$, b) $\Delta_R = 0.05$, c) $\Delta_R = 0.1$ and d) $\Delta_R = 0.2$. The dashed lines correspond the case of $\Delta_R = \Delta_D = 0$ and $B = \tilde{F} = 0$	33
Figure 3.4 Subband energy spectra as a function of linear momentum $k_x l_0$ for different spin-orbit coupling regimes when magnetic and electric fields are nor considered. a) Strong Rashba and weak Dresslhaus spin-orbit couplings $\Delta_R = 0.2$ and $\Delta_D = 0.01$ b) Both of spin-orbit interactions are in strong regime $\Delta_R = 0.2$ and $\Delta_D = 0.1$. The dashed lines correspond the case of $\Delta_R = \Delta_D = 0$ and $B = \tilde{F} = 0$	35
Figure 3.5 Energy dispersion curves of electrons in a double QWR with different orientation of magnetic field: a) $\phi = 0$, b) $\phi = \pi/6$, c) $\phi = \pi/3$, and d) $\phi = \pi/2$. The magnitude of magnetic field and the strength	

of spin-orbit interactions are fixed at $B = 1$ T, $\Delta_R = 0.2$ and $\Delta_D = 0.1$. The dashed lines correspond the case of $\Delta_R = 0.2$, $\Delta_D = 0.1$ and $B = 0$.
 36

Figure 3.6 The Stark effect on the energy subband structure of double quantum wire for different directions of magnetic field in the presence of strong spin-orbit interactions in the strong coupling limit, namely $\Delta_R = 0.2$, $\Delta_D = 0.1$ $B = 1$ T, $\tilde{\mu} = 1$, $\tilde{F} = 1$. The dashed lines correspond the zero electric field case. 38

Figure 3.7 Energy spectrum of double QWR in the presence of strong spin-orbit interaction ($\Delta_R = 0.2$, $\Delta_D = 0.05$) and an external magnetic field ($B = 1$ T). The orientation angle is chosen as $\phi = \pi/4$ where different values of $\tilde{\mu}$ are taken: a) 1, b) 1.5, c) 2, and d) 2.5. The dashed lines correspond the case of $\Delta_R = \Delta_D = 0$ and $B = 0$ 39

Figure 3.8 Variation of the energy dispersion curves of electrons in a double quantum wire in the presence of strong spin-orbit interaction ($\Delta_R = 0.2$, $\Delta_D = 0.05$) and an external magnetic field ($B = 1$ T) and electric field ($\tilde{F} = 1$). The orientation angle is chosen as $\phi = \pi/4$ where different values of $\tilde{\mu}$ are taken: a) 1, b) 1.5, c) 2, and d) 2.5. The dashed lines correspond the case $\tilde{F} = 0$ 40

Figure 3.9 Spin textures across the wire (y direction in l_0 units) in the presence of both type of spin-orbit couplings ($\Delta_R = 0.05$, $\Delta_D = 0.2$) and external magnetic field (3 T) oriented along the wire axis (left panel) and perpendicular to the wire axis (right panel). Plots from the top to down correspond to momentum $k_x l_0 = -0.69, 0.0, 0.69$ where arrow length is proportional to spin density. Blue solid lines correspond to the z component of magnetization. 43

Figure 3.10 Same as Fig. 3.9 for the second level of the lowest spin-split subband. 45

Figure 3.11 Spin textures across the wire subjected to external magnetic field $B = 1$ T with the angle $\phi = \pi/4$ in the presence of spin-orbit coupling characterized by $\Delta_R = 0.2$, $\Delta_D = 0.1$. The left panel corresponds to the zero electric field case, and the right panel presents the effect of electric

- field $\tilde{F} = 1$. Plots from the top to down correspond to momentum $k_x l_0 = -0.74, 0.0, 0.74$ where arrow length is proportional to spin density. Blue and black solid lines correspond to the z component of magnetization. 46
- Figure 3.12 Same as Fig. 3.11 for the second level of the lowest spin-split subband. 47
- Figure 3.13 Spin textures across the wire corresponding to the parameters: $\Delta_R = 0.2$, $\Delta_D = 0.1$, $B = 1$ T directed with angle $\phi = \pi/4$. Plots from top to bottom correspond to $\tilde{\mu} = 1, 1.5, 2$ when external electric field is zero (left panel) and electric field is not zero $\tilde{F} = 1$ (right panel). 48
- Figure 3.14 The spin projections of eigenstates in the lowest spin-split subbands for the parameters: $\Delta_R = 0.05$, $\Delta_D = 0.2$, $B = 3$ T. Left panel presents $\phi = 0$ case where the right panel shows $\phi = \pi/2$. The solid (dashed) lines show first (second) level of the lowest spin-split subband. Blue lines indicate $\langle \sigma_x \rangle$ whereas red lines represent $\langle \sigma_y \rangle$ 49
- Figure 3.15 The spin projections of eigenstates in the lowest spin-split subbands for the parameters: $\Delta_R = 0.2$, $\Delta_D = 0.1$, $B = 1$ T and $\phi = \pi/4$. Left panel presents $\tilde{F} = 0$ case where the right panel shows $\tilde{F} = 1$. The solid (dashed) lines show first (second) level of the lowest spin-split subband. Blue lines indicate $\langle \sigma_x \rangle$ whereas red lines represent $\langle \sigma_y \rangle$ 50
- Figure 3.16 Schematic representation of $\beta^{(n,s)}$. It is +1 for the minimum point and -1 for the maximum point in the energy subband. 52
- Figure 3.17 The conductance of double quantum wire as a function of Fermi energy in the presence of spin-orbit couplings for different direction of magnetic field with pink lines: a) $\phi = 0$, b) $\phi = \pi/3$, c) $\phi = \pi/6$ and d) $\phi = \pi/2$. The strengths of spin-orbit interaction and magnetic field are set $\Delta_R = 0.2$, $\Delta_D = 0.1$, $B = 1$, respectively. The structural parameter is chosen $\tilde{\mu} = 1$. The green lines correspond the pure case where $\Delta_R = \Delta_D = 0$ and $B = 0$ 53
- Figure 3.18 Conductance of double quantum wires as a function function of Fermi energy for different values of structural parameter a) $\tilde{\mu} = 1$ b) $\tilde{\mu} = 1.5$ c) $\tilde{\mu} = 2$ and d) $\tilde{\mu} = 2$ with pink lines in a constant magnetic field B

$= 1$, $\phi = \pi/4$ and in the presence of spin-orbit couplings $\Delta_R = 0.2$, $\Delta_D = 0.05$. The green lines correspond the case pure case where $\Delta_R = \Delta_D = 0$ and $B = 0$ 54

Figure 3.19 Calculated conductance as a function of Fermi energy in the presence of internal and external agents for different values of $\tilde{\mu}$. a) 1, b) 1.5, c) 2 and d) 2.5. The strength of spin-orbit interactions, magnetic field and electric field are: $\Delta_R = 0.2$, $\Delta_D = 0.05$, $B = 1$, $\phi = \pi/4$, $\tilde{F} = 1$ 56

Figure 4.1 The schematic illustration of quantum wire structure used in transport calculations. 57

Figure 4.2 The calculated a) total, b) and c) spin-split energy levels conductance as a function of Fermi energy. The spin-orbit coupling parameters are chosen as: in the first and third region $\alpha_{R1} = 2$ meV nm, $\alpha_{D1} = 1$ meV nm and in the second region $\alpha_{R2} = 10$ meV nm, $\alpha_{D2} = 5$ meV nm. In all regions magnetic field is zero. 67

Figure 4.3 The energy spin-split levels conductance as a function of Fermi energy for three different orientations of a constant magnetic field (0.5 T) with the same spin-orbit coupling constants with Fig. 4.2. 68

Figure 4.4 The calculated spin-split energy levels conductance a) G_{++} and G_{+-} , b) G_{-+} and G_{--} as a function of applied magnetic field along the wire axis. The spin-orbit coupling parameters are chosen as: in the first and third region $\alpha_{R1} = 2$ meV nm, $\alpha_{D1} = 1$ meV nm and in the second region $\alpha_{R2} = 10$ meV nm, $\alpha_{D2} = 5$ meV nm. The length of conductor is 300 nm and the Fermi energy is 1 meV. 69

Figure 4.5 Conductance as a function of Fermi energy for three lengths of conductor $L = 100, 200, 300$ nm. The spin-orbit coupling is zero at identical regions and $\alpha_{R2} = 10$ meV nm and $\alpha_{D2} = 5$ meV nm are chosen in the conductor. The magnetic field with strength $B = 0.5$ T is applied along the wire axis in all regions. 71

Figure 4.6 The total and mode dependent conductance as a function of conductor length for different Fermi energies $E_F = 0.56, 1.55, 2.55$ meV. The spin-orbit interaction is zero in identical regions, in the conductor the strength

of spin-orbit couplings are chosen as $\alpha_{R2} = 10$ meV nm and $\alpha_{D2} = 5$ meV. The magnetic field is $B = 0.5$ T and $\phi = 0$ 72

Figure 4.7 The calculated mode dependent conductance a) G_{++} and G_{+-} , b) G_{-+} and G_{--} as a function of orientation of magnetic field ($B = 0.5$ T). In region *I* and region *III*, the spin-orbit interaction is absent. The spin-orbit coupling parameters in the conductor are chosen as: $\alpha_{R2} = 10$ meV nm, $\alpha_{D2} = 5$ meV nm. The length of conductor is 300 nm and the Fermi energy is 2 meV. 73



CHAPTER ONE

INTRODUCTION

One of the most important aspects of the current technological revolution is the ever-decreasing size of the electronic device components which consist of the basis of the building blocks of future new technology. Great amount of attention has been devoted to investigate electronic behaviors of these devices to tackle the problems which stem from increasing miniaturization (Marsh & Inkson, 1986). Many new structures currently being investigated reveal that the junction between different semiconductors plays an important role in determining the behavior of device (Sze, 1981). These devices find in applications in semiconductor technology by offering the possibility of devices with higher speed and very low power dissipation. The technological applications of these structures reorient two main areas. The first is in the production of semiconductor lasers that will revolutionize the telecommunications industry with fiber optic cables. On the other hand, they serve as the building blocks for future devices which are faster and more powerful than those existing. From the point of view of research, heterojunctions are ideal systems for investigation of quantum mechanical properties of electrons and so provide a deeper insight into fundamental physics.

In recent years, increasing perfection in modern semiconductor growth techniques allows to obtain high quality low-dimensional quantum confined systems such as quantum wells (QWs), quantum wires (QWRs), and quantum dots (QDs) with varying sizes and shapes (Yu & Cardona, 2010). The electronic, spin and transport properties of these nanostructures are the key ingredients in the search of new devices with the advantages as increased data processing speed, lower electric power consumption in electronic and optical modulation technology (Kasapoglu et al., 2009; Zhang et al., 2006). Besides, the nonlinear effects in these low-dimensional systems can be enhanced significantly over those in bulk materials due to the existence of strong quantum confinement effect (Vaseghi et al., 2006). The confinement of electrons in these nanostructures modifies the electronic, spintronic and transport properties. Therefore, understanding of the electronic, spin and transport properties

of these systems is imperative because they have potential for a wide range of device applications based on inter-subband transitions of electrons such as laser amplifiers, photodetectors, high speed electro-optical modulation, quantum computing, and so forth (Capasso et al., 1986; Loss & DiVincenzo, 1998; Miller, 1990).

Furthermore, a great deal of effort has been dedicated to understand the basic properties of double semiconductor structures which play an essential role for the explanation of many physical phenomena such as tunneling and doublet splitting (Shi & Gu, 1997). Effects of external fields on the electronic and transport properties of double QWRs, consisting of two parallel long wires coupled through a potential barrier which allows the tunneling of the electrons between them, have been investigated both theoretically (Wang et al., 2005; Thomas et al., 1999) and experimentally (Moon et al., 1999; Yamamoto et al., 2005). The influence of magnetic field on the energy dispersion and magnetotransport properties of dual QWRs has been reported by Shi et al. (Shi & Gu, 1997). The energy spectrum, magnetization and conductivity of tunnel-coupled double QWRs subjected to an external magnetic field have been searched theoretically by Lyo and his collaborators (Lyo & Huang, 2001). Korepov et al. (Korepov & Liberman, 1999) studied the electronic transport properties of double QWRs by considering impurity, perpendicular magnetic field and correlated disorder.

Spin-orbit coupling is a manifestation of special relativity (Lorenz et al., 2007). When an electron moves in the reference frame, electric fields transform into magnetic fields. These fields interact with the spin of electron and lift the degeneracy between spin-up and down levels. The resulting spin-orbit fields are called as Rashba and Dresselhaus fields, if the electric field arises from structure or bulk inversion asymmetry, respectively (Jalil et al., 2008). Recent years, Rashba and Dresselhaus spin-orbit interactions have been the subject of numerous studies beyond semiconductors (Wrinkler, 2003). Also a vast number of creative research has been devoted to the discovery and designing of novel devices with the realization of manipulating spin orientation by moving electrons, controlling electron trajectories using spin as a steering wheel (Manchon et al., 2015). Recently, considerable interest has been focused on the spin-dependent phenomena in low-dimensional

semiconductors (Zhang et al., 2005). The key process in the device functionality relies on the generation or manipulation of spin-polarized electronic population which designate an excess of spin up or spin down electrons (Datta & Das, 1990). Efficient spin control can be achieved by means of spin-orbit interactions which arise from inversion asymmetry properties of semiconductor structures. Bulk inversion asymmetry gives rise to Dresselhaus spin-orbit interaction (Dresselhaus, 1955), whereas structural inversion asymmetry induces Rashba spin-orbit interaction (Rashba, 1960). Increasing number of works have surveyed the effects of external fields and spin-orbit couplings on the band structure behavior and transport properties of low-dimensional systems (Debald & Kramer, 2005; Gisi et al., 2016a; Governale & Zülicke, 2002; Karaaslan et al., 2015; Malet et al., 2007; Moroz & Barnes, 1999; Sarikurt et al., 2014; Zhang et al., 2009).

Understanding of the electronic properties of double QWRs is imperative because the electrical, spin and transport properties of devices made by these materials show exotic behaviors in the presence of different external agents (Gisi et al., 2016b). External fields and internal mechanisms are effective tools for studying the physical properties of double QWRs. Applying an external electric field to QWR is the simplest way by which the system can be used to design tunable devices (Sun, 1998). The interplay of different strength of spin-orbit couplings and magnetic and electric fields brings out the modification of the energy dispersion and consequently the conductance and phase shift between the modulations of the spin density components (Governale & Zülicke, 2002). An in-plane magnetic field is more appropriate to obtain a prominent spin resonance (Serra et al., 2005). Spin-orbit interactions generate an effective in-plane magnetic field which gives rise to a drift-driven in-plane spin polarization, and the summation of an external magnetic field and spin-orbit induced effective magnetic field leads to observation surprising spin polarization (Kato et al., 2004; Edelstein, 1990). Furthermore, the aforementioned effects cause considerable changes in the energy spectrum of the carriers which exhibit its mark on the spin textures and conductance of double QWR. In the light of these findings, in this thesis we aimed to investigate the combined effects of an external electric and in-plane magnetic field

on the electronic, spin and transport properties of double QWR incorporating the spin-orbit interaction. Moreover the part of the thesis is devoted to investigate zero-temperature ballistic conductance of a parabolic QWR subjected to in-plane magnetic field in the presence of Rashba and Dresselhaus spin-orbit interactions.

The structure of the thesis is as follows. In Chapter 2, we briefly present the properties of semiconductor wires and fabrication techniques and introduce spin-orbit interactions, Zeeman effect, Stark effect and quantum transport phenomena. The numerical results and discussions of the thesis are reported in Chapter 3. We give results of the ballistic transport of QWR formed by harmonic potential in Chapter 4. Finally, a short concluding chapter summarizes our findings.

CHAPTER TWO

THEORETICAL BACKGROUND

2.1 Low-Dimensional Systems

In 1970s semiconductor QWs and superlattices were investigated by Esaki and Tsu (Esaki & Tsu, 1970). After this investigation these structures have evolved from scientific interest into designing semiconductor devices. After the 1980s, with the improvement in growth techniques the fabrication of lower dimensional systems has been possible. One of the main goals of modern semiconductor physics is the study of low-dimensional systems in order to materialize devices which utilize quantum confinement effects (Sidor, 2007). The possibility of modulating the physical properties of these systems by reducing the dimensions from the macroscopic scale to nanoscale has been studied intensively. In low-dimensional semiconductors quantum confinement can be carried out in two different ways. The first one is growth of inhomogeneous layer structures which result in a perpendicular quantization to the substrate surface. The other one is lateral patterning using ultrafine lithography techniques (Ferry et al., 2009). The quantum confined systems developed in heterolayer structures which grow on semiconducting substrates. The artificial confinement leads to quantization of semiconductor states. And the first demonstration of this effects was Si metal oxide semiconductor (Fowler et al., 1966). In this system, the confining potential of the Si/SiO₂ interface barrier and the potential well in the other direction due to band bending lead to quantization of carrier motion. The development of precise epitaxial growth techniques such as molecular beam epitaxy and metal organic chemical vapor deposition made it possible to realize high-quality lattice-matched heterojunction systems (Petroff et al., 1982). These systems exhibit quantum confinement effects bigger than those in the Si metal oxide semiconductor system. Because lattice-matched heterojunctions such as GaAs and Al_xGa_{1-x}As include low surface state density at the interface and have lower conduction band mass.

III-V semiconductor compounds generally are formed of zinc-blende crystal structures.

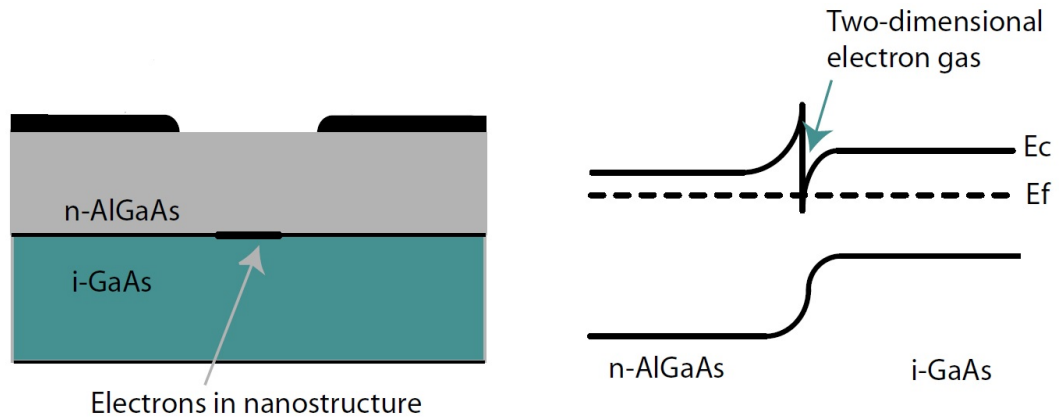


Figure 2.1 Schematic illustration of two-dimensional electron gas which is located in the interface between two heterostructures. (Havu, 2005)

GaAs and AlGaAs have quite similar lattice constants which enables a very sharp interface without disturbing lattice errors stem from crystal strain (Wagner, 2009). GaAs has a band-gap of 1.42 eV whereas AlAs has larger gap of 2.16 eV. The band-gap of GaAs and $\text{Al}_x\text{Ga}_{1-x}\text{As}$ alloy is between these two values and depends on the concentration x (Yu & Cardona, 2010). The Fermi energy in the narrowgap GaAs layer is lower than in the widegap AlGaAs layer. When these two crystals are brought together, electrons start to spill over from the negatively doped n-AlGaAs and leaves behind positively charged donors. This space charge gives rise to an electrostatic potential that causes the bands to bend (Gişi, 2012). When equilibrium is achieved the Fermi energy is constant in the sample and it is inside the conduction band. The electron density is sharply peaked near the GaAs-AlGaAs interface and the conduction band forms a triangular QW crossing the Fermi energy. And it forms a very thin conducting layer (Havu, 2005). Therefore a two-dimensional electron gas is formed as shown in Figure 2.1. By applying a further confinement to a two-dimensional electron gas it is possible to restrict the electron motion in directions along the interface. This enables to vary the size and shape of the device in a controlled way. When the electrons are confined in one direction and can easily move in two dimensions, this system is known as QW. In QWRs the confinement is in two dimensions and the movement of electrons is allowed only in one direction. The electron are confined in three dimensions in QDs.

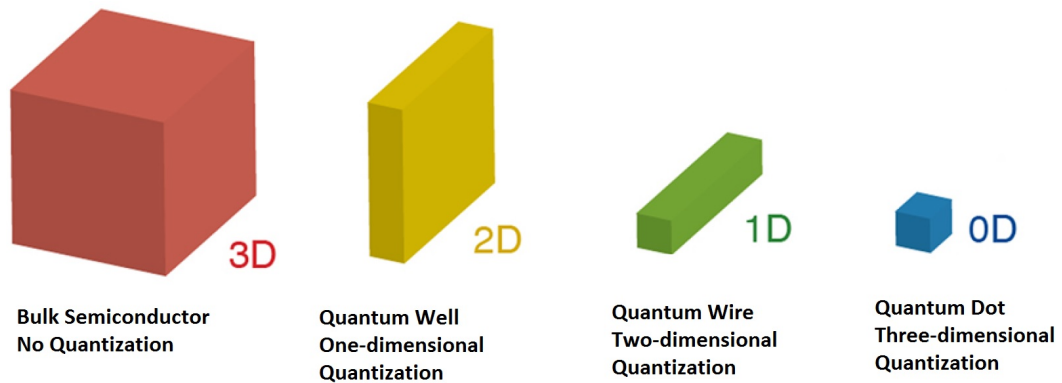


Figure 2.2 Schematic representation of semiconductor nanostructures with reduced dimensionality: bulk semiconductor, quantum well, quantum wire and quantum dot.

2.2 Quantum Wires

QWR is described as a strip of conducting material with the size of 10 nanometers or less. It exhibits quantum mechanical effects such as the Aharonov-Bohm effect (Ji & Miao, dt). In the information transfer process, there is a basic difference between QWR and classical wire. In the QWR the information can not be copied instead the information at the source must be destroyed and re-created it at the destination (Isailovic et al., 2004). Semiconductor QWRs have been studied intensively for a wide range of variety of materials. The QWRs are interesting for fundamental research because they have unique structural and physical properties relative to their bulk counterparts. The interest in QWRs stems from two facts. First, the effective size of QWR can be easily controlled and made remarkably small, down to the de Broglie wavelength of an electron. The controllability of size of QWR makes it possible to realize experimental systems which have an arbitrary number of occupied transverse modes (Pramanik et al., 2007). On the other hand, the electron motion can be rendered almost collisionless because of the high purity of 2DEG's grown by molecular beam epitaxy (Gişi, 2012). Due to the coexistence of these two factors, the QWRs offer fascinating potential for future technological applications (Malet et al., 2007). QWRs are promising candidates for the development of optoelectronic and microelectronic devices and they are now used for a variety of applications including optical probes, light-emitting diodes, photo detectors, fiber optics communication

network systems, photovoltaic devices (Krishna, 2005; Kukushkin, 2009; Majumdar et al., 2010; Saravanan et al., 2015).

In 1989, first QWR laser was achieved in multi-mode V-shaped GaAs/AlGaAs wires (Kapon et al., 1989). After this seminal invention, QWR laser has attracted active studies (Hayamizu et al., 2002; Suárez et al., 2006; Wegscheider et al., 1993). Another possible application of QWRs is in quantum information processing (Bennett & DiVincenzo, 2000). Moreover, the double-well potential for one-dimensional quantum systems is received a considerable amount of attention from various branches of physics to chemistry (Banerjee & Bhatnagar, 1978; Balsa et al., 1983; Pedram et al., 2010; Hodgson & Varshni, 1989; der Straeten & Naudts, 2006; Handy, 1992). The properties of a large number of physical and chemical systems are studied by assuming that the potential function responsible for such properties is well represented by means of a function with two valleys and a barrier between them. Examples for a such potentials are infrared spectra of NH₃ molecule, infrared and Raman spectroscopy of hydrogen-bonded systems, structural phase transitions, macroscopic quantum coherence in superconducting Josephson device and so on (Papageorgiou et al., 1990; Simos & Raptis, 1990). The separation between the two lowest-lying energy states is the most important characteristic of these systems because it defines the tunneling rate through the double-well barrier (Yamamoto et al., 2005). Double QWRs consisting of two long valleys separated by a potential barrier are of interest because of fundamental investigations on tunnel coupling between two quantum systems (Shi & Gu, 1997). It was demonstrated that it is possible to establish level spectroscopy of single and coupled QWR states by all-electrical means. This work has prompted an active study field in quantum engineering of coupled quantum waveguide devices, such as quantum waveguide inverters, bi-directional couplers (Fischer et al., 2006a). In particular, coherent electron transport in quantum wires coupled through a potential barrier has been proposed for the elementary quantum bit realization (Bertoni et al., 2000). Furthermore, double QWRs can be used for light-emitting devices (Karlsson et al., 2004).

The ability to create QWRs with very high accuracy makes them very promising

candidates for future electronic devices. QWRs can be fabricated with different techniques. Among them: molecular beam epitaxy (González et al., 2000), electron-beam lithography, wet/dry chemical etching (Petroff et al., 1982), optical lithography and epitaxial growth techniques which can be separated as V-shaped (Kapon et al., 1989) and T-shaped (Pfeiffer et al., 1990). In optical lithography the sample is first covered with a photosensitive resist and then exposed with ultraviolet light through a mask, which contains the pattern of the structure. Then the exposed surface of the sample is etched down by typically 100 nm, thus removing also the 2DEG in these regions. In this technique, the main limitation of the resolution is the wavelength of the light (larger than 200 nm) and the mechanical precision of the exposing equipment (mask aligner). Electron beam lithography overcomes this limitation with the shorter wavelength of the electrons and is widely used for the fabrication of semiconductor nanostructures (Alessandro, 2005).

2.3 Introduction to Spintronics

Until recently, the electron spin was ignored in traditional charge-based electronics and all the electronic devices exploited negative charge carriers-electrons and positive charge carriers-holes. This leads to an unused additional degree of freedom of both charge carriers have: spin. Emerged technology called spintronics where not only electron charge but also spin carries information. This new field promises opportunities for a new generation of devices combining standard microelectronics with spin-dependent effects which arise from the interaction between spin of the carrier and the magnetic properties of material (Wolf et al., 2001). In the traditional approaches there are two directions of a spin namely up or down relative to a reference such as an applied magnetic field. Device operations depend on the degree of directions. Adding the spin degree of freedom to traditional semiconductor charge based electronic leads to obtain electronic products with more capability and performance. These new devices offers opportunities for technology with decreased electric power consumption and increased data processing speed compared with those currently existing (Malet

et al., 2007). The possibility to carry out controllable spin injection, detection and manipulation leads to new spin-based multifunctional devices such as quantum bits for quantum computation and communication, optical switches, spin-field effect transistor, encoders. The success of these ventures depends on a deeper understanding of spin interactions and controlling of spin degree of freedom in semiconductor structures.

2.4 Spin-Orbit Interactions

A consequence of relativity is that the spin and momentum of an electron can be coupled in the presence of electric fields (Kato et al., 2004). This effect is called spin-orbit coupling. Even in the absence of applied magnetic fields, this interaction opens a pathway to the manipulation of electron spins in semiconductor heterostructures which present intrinsic spin-orbit interactions arising from inversion asymmetry properties characteristic of those systems (Malet et al., 2007).

The main mechanism of spin-orbit interactions can be explained as follows: Dirac electron which moves in an electric field experiences an effective magnetic field and therefore the electric field is essentially converted into a magnetic field (Park et al., 2013). The Dirac equation of an electron is given by (Sakurai, 1967):

$$H = c\boldsymbol{\alpha} \cdot \mathbf{p} + \beta m_0 c^2 + eV, \quad (2.1)$$

where c is speed of light, \mathbf{p} is the momentum operator, e is the charge of electron, V is the scalar potential, α and β are the usual four-dimensional Dirac matrices defined as:

$$\alpha = \begin{pmatrix} 0 & \sigma \\ \sigma & 0 \end{pmatrix} \quad \beta = \begin{pmatrix} \mathbb{I} & 0 \\ 0 & -\mathbb{I} \end{pmatrix} \quad (2.2)$$

The Hamiltonian form of the Dirac equation can be expressed as:

$$i\hbar \frac{\partial \Psi}{\partial t} = (c\boldsymbol{\alpha} \cdot \mathbf{p} + \beta m_0 c^2 + eV)\Psi \quad (2.3)$$

$|\Psi\rangle = (\psi_A, \psi_B)^T$ is two coupled wave function which consists of four spinors. Using the Equation 2.2 and Equation 2.3 the spinor ψ_B is obtained in terms of ψ_A .

$$(\boldsymbol{\sigma} \cdot \mathbf{p})\psi_B = \frac{1}{c}(E' - V)\psi_A \quad (2.4)$$

$$(\boldsymbol{\sigma} \cdot \mathbf{p})\psi_A = \frac{1}{c}(E' - V + 2mc^2)\psi_B \quad (2.5)$$

$$\psi_B = \boldsymbol{\sigma} \cdot \mathbf{p} \left[\frac{c}{(E' - V + 2mc^2)} \right] \psi_A \quad (2.6)$$

Equation 2.4 can be rewritten by substituting Equation 2.6

$$(\boldsymbol{\sigma} \cdot \mathbf{p})(\boldsymbol{\sigma} \cdot \mathbf{p}) \left[\frac{c}{(E' - V + 2mc^2)} \right] \psi_A = \frac{1}{c}(E' - V)\psi_A \quad (2.7)$$

In nonrelativistic limit $(E' - V)/2mc^2 \ll 1$ and so $\left[\frac{c}{(E' - V + 2mc^2)} \right]$ can be expanded

$$\frac{c}{(E' - V + 2mc^2)} \approx \frac{1}{2m} \left(1 - \frac{E' - V}{2mc^2} + \dots \right). \quad (2.8)$$

With this expansion, Equation 2.6 is obtained as:

$$\psi_B \approx \frac{1}{2mc} (\boldsymbol{\sigma} \cdot \mathbf{p})\psi_A. \quad (2.9)$$

By inserting $(\boldsymbol{\sigma} \cdot \mathbf{p})(\boldsymbol{\sigma} \cdot \mathbf{p}) = p^2$ and Equation 2.8 in Equation 2.7, one can obtain simply Schrödinger equation.

$$\left(\frac{p^2}{2m} + V \right) \psi_A = E' \psi_A \quad (2.10)$$

In accordance with Dirac theory the wave function have to be normalized.

$$\int d^3r \Psi^\dagger \Psi = \int d^3r (\psi_A^\dagger \psi_A + \psi_B^\dagger \psi_B) = 1 \quad (2.11)$$

From Equation 2.9 writing ψ_A instead of ψ_B , we can reformulate normalization equation such as:

$$\int d^3r \psi_A^\dagger \left(1 + \frac{p^2}{4m^2 c^2} \right) \psi_A = 1. \quad (2.12)$$

According to the Equation 2.13 the normalized two coupled wave function Ψ is given

by:

$$\Psi = \left(1 + \frac{p^2}{8m^2c^2}\right)\psi_A. \quad (2.13)$$

After some rearrangement, Dirac equation in non-relativistic limit can be obtained.

$$\left[\frac{\mathbf{p}^2}{2m} + V - \frac{\mathbf{p}^4}{8m^3c^2} - \frac{\hbar}{4m^2c^2}\boldsymbol{\sigma} \cdot [\mathbf{p} \times \nabla V] + \frac{\hbar}{8m^2c^2}\nabla^2 V\right]\Psi = E\Psi \quad (2.14)$$

The first two terms are kinetic and potential energy, respectively. The third one is a relativistic correction to the kinetic energy. The last one is Darwin term. And the fourth term is spin-orbit coupling term in general form the three-dimension spin-orbit interaction Hamiltonian.

$$H_{SO} = -\frac{\hbar}{4m^2c^2}\boldsymbol{\sigma} \cdot [\mathbf{p} \times \nabla V] \quad (2.15)$$

where V is the electric potential.

When an electron moves in an electric field, it feels an effective magnetic field even without any external magnetic field. This effective field stemming from spin-orbit interactions can be expressed as (Jalil et al., 2008):

$$B_{eff} = \frac{\mathbf{p} \times \mathbf{E}}{2mc^2}. \quad (2.16)$$

According to the equation, the direction of effective magnetic field is perpendicular to the momentum and electric field. $2mc^2$ is the energy gap between an electron and positron in vacuum and the energy scale of $2mc^2$ is ~ 1 MeV. And the spin-orbit effective field is usually neglected for a particle with nonrelativistic momentum in vacuum. A large spin-orbit effective field can be obtained in two cases either in the presence of a large electric field or in materials with reduced mass gap. The first one is takes place in an atom. Because the Coulomb field arising from nucleus is sufficiently large to induce an energy shift in the energy levels of an electron bound to the nucleus (Jalil et al., 2008). Bulk inversion asymmetry and structural inversion asymmetry lead to a large electric field in semiconductor structures. The internal electric field of the bulk inversion asymmetry arises from the microscopic

Coulomb potential gradient of the atomic nucleus region and it is usually difficult to modulate. The internal electric field of the structural inversion asymmetry originates from both the microscopic Coulomb potential induced by atomic nucleus and the macroscopic potential gradient due to the heterointerface and the band bending in the semiconductor heterostructures (Wrinkler, 2003). The second case occurs in some III-V semiconductor materials with small effective electron mass such as InAs ($m^* = 0.03m$)

In solid state systems, three different sources of electric field induces spin-orbit interactions. First one is impurity in the conduction layer, second is lack of crystal inversion symmetry and the last one is the lack of structural inversion symmetry of the confinement potential of electrons in a heterostructure. The spin-orbit interaction stems from impurities can be neglected in practise because it is very weak in epitaxially grown III-V QWs (Meijer, 2005). In the absence of the other two mechanisms, impurities are the main source of spin-orbit interaction in metallic systems. Most of III-V semiconductors crystallize in the zinc-blende structure lacks an inversion symmetry. When electrons move through this lattice they experience an asymmetric confining potential. This effect which gives rise to spin-splitting in conduction band was demonstrated theoretically by Dresselhaus. So this type of spin-orbit interaction is called as Dresselhaus spin-orbit interaction (Dresselhaus, 1955). An asymmetric confining potential induces last type of spin-orbit interaction. This mechanism is important because the confinement potential can be varied electrostatically which allows to tune the strength of spin-orbit interaction via gate voltages. This type of spin-orbit interaction is known as Rashba spin-orbit interaction (Rashba, 1960).

In an sample the total spin-orbit interaction is the sum of the three type of spin-orbit interaction. The spin-orbit interaction lifts the electron degeneracy for nonvanishing momentum creating spin-split energy bands even in the absence of external magnetic field (Zhang et al., 2005). And the competition between these spin-orbit interactions causes to observe complex electronic, spintronic and transport properties.

2.4.1 Rashba Spin-Orbit Interactions

The QW confining electrons in two dimensions is never perfectly flat because of the charging effects. Thus when two differently doped semiconductors are brought together, gradient arises $\nabla V = \mathbf{E}$ at the interface. This effective electric field couples with the electron motion as (Wrinkler, 2003)

$$H_R \propto (\mathbf{E} \times \mathbf{p}) \cdot \boldsymbol{\sigma}. \quad (2.17)$$

When QW is considered along the (001) growth direction $\mathbf{E} = E_z \mathbf{z}$ and the Rashba spin-orbit coupling can be rephrased as:

$$H_R = \frac{\alpha_R}{\hbar} (\boldsymbol{\sigma} \times \mathbf{p}) \cdot \mathbf{z} = \frac{\alpha_R}{\hbar} (p_y \sigma_x - p_x \sigma_y), \quad (2.18)$$

where α_R is the Rashba spin-orbit coupling parameter and it consists of two terms, a field contribution due to the potential gradient of the band-bending and an interfacial contribution due to the electric field at the heterojunction interface (Jalil et al., 2008). Rashba spin-orbit interaction gives rise to an effective magnetic field perpendicular to \mathbf{k} and the symmetry-breaking axis $\hat{\mathbf{n}}$, but its relative orientation to \mathbf{k} remains constant in the plane normal to $\hat{\mathbf{n}}$ (Kato et al., 2004).

It is experimentally shown that the strength of Rashba coupling can be tuned via proper gating of structure (Nitta et al., 1997; Engels et al., 1997) which makes Rashba spin-orbit interaction very appealing for potential technological applications.

2.4.2 Dresselhaus Spin-Orbit Interactions

The Dresselhaus spin-orbit interaction is a bulk property as it arises from the inversion asymmetry of the crystal. This asymmetry is fixed for a given sample, is intrinsic of the system and it is not possible to manipulate it externally (Scheid et al.,

2008). The three-dimensional spin-orbit interaction Hamiltonian reads:

$$H_D \propto p_x(p_y^2 - p_z^2)\sigma_x + p_y(p_z^2 - p_x^2)\sigma_y + p_z(p_x^2 - p_y^2)\sigma_z \quad (2.19)$$

where p_x, p_y, p_z is momentum operator. In order to achieve the effective Hamiltonian acting on the electrons confined in the two-dimensional electron gas we have to integrate along the growth direction. There is a constraint for $\langle p_z \rangle = 0$, while $\langle p_z^2 \rangle \neq 0$ because it is a sample dependent constant. The Dresselhaus spin-orbit Hamiltonian is given by

$$H_D = \alpha_D(p_y\sigma_y - p_x\sigma_x) + \gamma(p_x p_y^2 \sigma_x - p_y p_x^2 \sigma_x) \quad (2.20)$$

here γ is the material dependent constant and α_D depends on $\langle p_z^2 \rangle$. The first term is linear in the electron momentum and called as linear Dresselhaus term and second one is cubic Dresselhaus term (Wrinkler, 2003). In a two-dimensional electron gas, the cubic Dresselhaus term is usually neglected, as it is generally smaller than the linear contribution. The strength of Dresselhaus spin-orbit interaction depends only on the atomic elements in the crystal lattice.

Dresselhaus spin-orbit interaction has a quantization axis perpendicular to the electron wavevector \mathbf{k} and it changes its orientation with respect to \mathbf{k} as the direction of \mathbf{k} changes between crystal directions $[110]$ and $[1\bar{1}0]$ (Kato et al., 2004).

2.5 Effect of External Static Fields

Inclusion of external static fields change the physical properties of the low-dimensional systems. When an atom is subjected to an external magnetic field \mathbf{B} , the total angular momentum of electron \mathbf{J} is quantized in space with respect to the alignment of magnetic field. The energy of atomic state is characterized by the angular momentum quantum number j and it is split into $2j + 1$ energy levels. This splitting of the energy levels induces a splitting of the spectral lines which are emitted by atom. The splitting of the spectral lines of an atom subjected to an external magnetic field is

known as the Zeeman effect (Tipler & Llewellyn, 2008). Zeeman Hamiltonian for an electron which has only intrinsic spin angular momentum is given as:

$$H_Z = -\boldsymbol{\mu} \cdot \mathbf{B} = g^* \mu_B \mathbf{S} \cdot \mathbf{B} \quad (2.21)$$

where $\boldsymbol{\mu} = -g^* \mu_B \mathbf{S}$ is magnetic moment and $\mu_B = e\hbar/2m^*$ is Bohr magneton.

The spin of charge carrier can be controlled by using an external magnetic field and this provides an extra degree of freedom which can be utilized for device functionalities such as electronics, spintronics (Martin et al., 2008; Elzerman et al., 2004). In semiconductor devices, an external magnetic field breaks the degeneracy of two spin states at all wave vectors. Because the wave vector is independent of Zeeman splitting which is given as $\Delta E_z = g^* \mu_B B$. Zeeman effect gives rise to spin-polarized transport, where a particular spin orientation dominates the electrical conductance of the device.

Stark effect is due to the interaction between the electric moment of the atom and the external electric field. The leading term to the interaction energy is given as

$$U = -\mathbf{p} \cdot \mathbf{E}, \quad (2.22)$$

where \mathbf{E} is the external electric field and \mathbf{p} is the electric moment. The distribution of the charges within the atoms results to electric dipole moments in atoms. The Stark effect is to be considered two aspects such as the linear effect and the quadratic effect (Bethe & Salpeter, 1957). The linear Stark effect is due to a dipole moment that arises from a naturally occurring nonsymmetric distribution of electron charge, whereas the quadratic Stark effect is due to a dipole moment that is induced by the external field. When an external electric field is applied, an arbitrary n energy level splits into $2n - 1$ sublevels (Littman, dt). The spacing between sublevels increase linearly with the applied electric field. Thus the higher n states are more sensitive to the external field. For states with no linear shift such as ground state ($n = 1$), there is still a shift due to external fields. The shift is quadratic in its dependence on field strength (Tipler & Llewellyn, 2008).

2.6 Quantum Transport

In recent years, with the development of nanotechnology, it has become possible to obtain low-dimensional systems. The idea of possibility of designing and manufacturing the devices and electrical circuits in the atomic sizes opened up a new area in the field of physics. Fabrication of computer chips with 30 nm has become routine. When the size of electronic systems decreases, many of physical properties of them change. In the single atom or molecule scale, the electrical and transport properties are determined by quantum mechanics because in this limit charge quantization and individual electronic states play important role. In this case, even small changes such as single electron tunneling events lead to difference in observed physics (Fulton & Dolan, 1987; Meir et al., 1991).

Among these studies, the charge transport has prompted an intensive study field. After carrying out the first experiments on conductivity properties of single molecules, the electron transport, especially the phenomena of quantum transport has become an attractive study field (Reed et al., 1997; Smit et al., 2002). One of the main goal of nanophysics is to manufacture and control nano-scale systems. The efforts of carrying out to control and manipulate a system with such a small size cause to study electron transport phenomenon.

Classical transport theories act as particles to electrons. Phonons, impurities and scattering by electrons controls the motion of electrons. When the size of device reaches the characteristic scattering length, the electrons can travel through the device only by scattering a few times. In this case, the wavefunction of the electron spreads throughout the device and classical approaches starts to collapse (Datta, 1995). The transport properties of the semiconductor nanostructures depend on characteristic length scales and their relation to the size of the system. If the size of the conductor is much larger than all of characteristic lengths, it usually shows classical ohmic behaviour. These length scales varies from one material to other material and they depend on electric field, impurity concentration, temperature and

magnetic field (Schöll, 1998).

The size of the conductor is characterized by four important length scales such as the de Broglie wavelength, the mean free path, the phase relaxation length of electrons and the magnetic length. The de Broglie wavelength is the electron wavelength at the Fermi level and it $\lambda = 2\pi/k = h/(2m^*E)^{1/2}$ is related to the kinetic energy of an electron. When the size of the conductor is the same order of magnitude as de Broglie wavelength, the quantum mechanical effects such as the wave-like nature of the electron, become important. The mean free path l_m is the average distance that an electron travels before it has lost its original momentum by experiencing elastic scattering. The dominant elastic scattering mechanism is impurity scattering. The mean free path is related to the momentum relaxation time τ_m and average carrier velocity v , namely $l_m = v\tau_m$.

The phase relaxation length l_ϕ is defined as the average distance that an electron travels before it destroys its initial coherent state by experiencing inelastic scattering. Typical scattering events, such as electron-phonon and electron-electron collisions, change the energy of the electron and randomize its quantum mechanical phase. Phase relaxation usually occurs on a timescale τ_ϕ in high-mobility degenerate semiconductors. τ_ϕ is same order or shorter than the momentum relaxation time. Phase relaxation length is proportional to Fermi velocity v_F and τ_ϕ , $l_\phi = v_F\tau_\phi$. In low-mobility semiconductors, momentum relaxation time is shorter than phase relaxation time and diffusive motion can occur in a phase-coherent region. $D = v_F^2\tau_\phi/2$ denotes the diffusion constant and the relation between it and phase relaxation length is given as $l_\phi^2 = D\tau_\phi$. If the size of the conductor is smaller than the phase relaxation length, waves of electrons interfere and quantum mechanical phenomena appear. These phenomena plays important role in the transport properties of devices. Another important length is magnetic length l_B . When an external magnetic field is applied, the electron energy is quantized $E_n = (n + \frac{1}{2})\omega_c$ where $\omega_c = eB/m^*$ is the cyclotron frequency. The magnetic length is defined as $l_B = (\hbar/eB)^{1/2}$ and it characterizes the extension of cyclotron orbit. The magnetic length is important because it can be tuned over a large range by changing the magnetic field. Therefore an external magnetic can be tool to reduce the effective dimensionality of the system.

According to the relation between the characteristic lengths and system size L , different transport regimes are defined. In macroscopic limits $L \gg l_m, l_\phi$, the charge carriers experience many elastic and inelastic collisions. This regime is called as classical diffusive transport. In coherent transport, the system size is smaller than phase relaxation length and the wavefunction of the carriers has a well-defined phase. In this regime conductance fluctuations and quantum interference events are observed. When the system size is smaller than mean free path, charge carriers can travel through the device without any scattering and this regime is known as ballistic transport.

When electrons move in a material they scatter from impurities, defects, phonons and other electrons. The scattering from other electron is assumed less important (Ashcroft & Mermin, 1976). This scattering leads to electrical resistance and in macroscopic size electronic components the conductance expressed as

$$G = \sigma \frac{A}{L}, \quad (2.23)$$

here σ is conductivity, A and L are the perpendicular area and the length of the conductor, respectively. In the macroscopic scale, the scatterers are uniformly distributed into the material so the Ohm's law is understandable. A longer device has also more scatterers to reduce the collective electron drift movement. According to Ohm's law, when the conductor gets narrower $A \rightarrow 0$ the conductance vanishes and when the length of conductor is very short $L \rightarrow 0$ the conductance becomes infinite. This behaviour can be explained via the assumption that the conductivity does not depend on the size of the conductor. Since the conductivity is a macroscopically defined quantity and it is assumed to be homogenous over the conductor. When the size of conductor is in the atomic scale, the homogeneity of the conductivity is violated. In this regime it is not surprising that statistical Ohm's law breaks down and other theories have to be used.

A quantum mechanical formulation of the electronic transport through a small conductor was first proposed by Landauer (Landauer, 1970; Datta, 1995). Landauer suggested a simple formula that set up the relation between the transmission probability

of the electron and the electronic conductance in one-dimensional conductors. After that Büttiker proposed a multi-channel Landauer formula for multi-probe devices (Büttiker et al., 1985; Büttiker, 1986).

2.6.1 Landauer-Büttiker Formalism

The Landauer approach is the building block of this field due to its conceptual simplicity, its predictive power, and for having introduced most of the concepts upon which our understanding of transport at the meso/nanoscale is based (Piccinin, 2006). The Landauer formula can be derived for a system roughly as follows: For simplicity, one can consider two-dimensional system subjected to transverse confining potential such as harmonic potential $V(y) = \frac{1}{2}m^*\omega_0^2y^2$ and the conductor is uniform in the x direction. The Schrödinger equation of such a systems is given as:

$$\left(\frac{p_x^2}{2m^*} + \frac{p_y^2}{2m} + V(y) \right) \psi(x, y) = E\psi(x, y). \quad (2.24)$$

The confinement potential is translationally invariant in the x -direction. The wave function in the QWR can be spatially separated into the n th eigenfunction of the confinement potential $\chi(y)$ and a plane wave e^{ikx} traveling along the wire.

$$\psi(x, y) = \frac{1}{\sqrt{l}} e^{ikx} \chi(y), \quad (2.25)$$

where l is the length of the conductor. The eigenenergies of the system are

$$E_n(k) = \frac{\hbar^2 k^2}{2m^*} + \varepsilon_n = \frac{\hbar^2 k^2}{2m^*} + \left(n + \frac{1}{2} \right) \hbar\omega_0, \quad (2.26)$$

where ε_n defines as the n th eigenenergy of the confinement. Conduction electron needs energy $E \geq \varepsilon_n$ to enter band n of the QWR. When the energy of an electron in band n is $E = \varepsilon_n$ the electron is at the band bottom and it does not have any kinetic energy along the wire. All the energy is in the transverse direction, i.e, in the confinement potential. When the energy of electron is larger $E > \varepsilon_n$ its kinetic energy along the wire is given

as $E_n^x = E - \varepsilon_n = \hbar^2 k^2 / 2m^*$. The corresponding velocity operator can be written as:

$$v_n^x(E) = \frac{1}{\hbar} \frac{\partial E_n(k)}{\partial k} = \frac{\hbar k}{m^*} = \sqrt{\frac{2(E - \xi_n)}{m^*}}. \quad (2.27)$$

In the Landauer approach the conductance through a two-terminal system is derived. One imagines to have a wire connected to two leads with chemical potentials μ_L and μ_R , respectively as illustrated in Figure 2.3. The leads are assumed to be ballistic

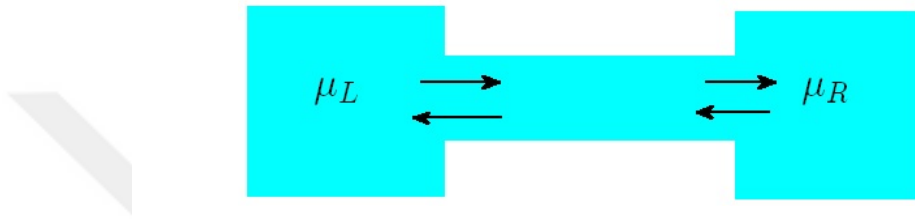


Figure 2.3 Schematic of the system used to study electron transport.

conductors in which no scattering occurs so the transmission probability is equal to one. And the leads can be treated as electron reservoirs at a fixed chemical potential. In Landauer approach the transport of this geometry can be interpreted as a scattering problem. A carrier flux comes from left lead, is scattered by the conductor and is transmitted to right lead. The current is proportional to the transmission coefficient which is the probability of an electron to be transmitted from left lead to right lead. Landauer approach is applied to systems in which electrons experience no inelastic scattering. Thus the transport is assumed as coherent.

When a bias V is applied to the electrodes, it shifts the chemical potential of the reservoirs such that $\mu_L - \mu_R = eV$. According to the Landauer approach the contacts are not reflecting. It is assumed that an electron in the conductor can enter the electrode without any reflection. The states in the left lead with positive momentum ($+k$) are occupied with equilibrium distribution $f_L(E)$ whereas the states in the right lead with negative momentum ($-k$) are occupied with equilibrium distribution $f_R(E)$. In order to compute current, all possible scattering mechanisms in the conductor are neglected so

the transport is assumed to be ballistic. A uniform electrons gas with n electrons per unit length moving with velocity v carries a current equal to env . The electron density of a single $+k$ state in the conductor of length l is equal to $1/l$. The $+k$ state carries the current which is given as:

$$I^+ = \frac{e}{l} \sum_k v_k f_L(E_k) T_{LR} = \frac{e}{l} \sum_k \frac{1}{\hbar} \frac{\partial E}{\partial k} f_L(E_k) T_{LR}, \quad (2.28)$$

where $T_{LR}(E)$ denotes the transmission probability of an electron at energy E from left lead to right lead. Converting the summation to integral

$$\sum_k \rightarrow 2l \int \frac{dk}{2\pi}, \quad (2.29)$$

and including the contribution of all subbands, the current is expressed as:

$$I^+ = \frac{2e}{h} \int_{V_L}^{\infty} f_L(E) T_{LR}(E) dE, \quad (2.30)$$

where the factor 2 is for spin. Similarly, the contribution of the states with negative momentum to current is

$$I^- = \frac{2e}{h} \int_{V_R}^{\infty} f_R(E) T_{RL}(E) dE. \quad (2.31)$$

Here the $T_{RL}(E)$ the transmission probability from right reservoir to left reservoir. At zero temperature, assuming the number of modes is constant over the range $\mu_R < E < \mu_L$, the total current can be given as:

$$I = I^+ - I^-. \quad (2.32)$$

Equation 2.30 and Equation 2.31 are substituted in Equation 2.32 and the current is obtained:

$$I = \frac{2e^2}{h} \int_{V_L}^{\infty} T(E) [f_L(E) - f_R(E)] dE. \quad (2.33)$$

It must be noted that the states which are in and around the energy interval $[\mu_L, \mu_R]$

leads to the largest current. This can be explained via Figure 2.4. The states below $\approx \mu_R - k_B T$ are fully occupied and there are equal amount of states with positive and negative velocities. Therefore the current contribution of these states cancel out. At finite temperatures the border sates in the $\approx \mu_R \pm k_B T$ and $\approx \mu_L \pm k_B T$ interval are not fully empty or occupied. Hence these gives rise to a net current contribution. At low temperatures, one can make an approach that these border states are either empty or fully occupied. At this case only $[\mu_R, \mu_L]$ interval gives current contribution (Porgilsson, 2012).

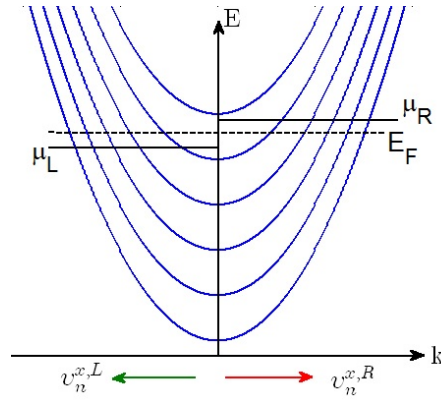


Figure 2.4 Schematic illustration of the chemical potentials μ_L and μ_R , the Fermi energy E_F , the direction of the k dependent electron velocities in the bands.

If the difference between chemical potentials of sources is small and the transmission probability is approximately constant over the energy range in which transport occurs, the system is in a linear response regime. This enables to rewrite Equation 2.33 via Taylor expansion such as

$$I \approx \frac{2e}{h} \int_0^\infty T(E) \left[\frac{\partial f_0}{\partial \mu} (\mu_L - \mu_R) \right] dE, \quad (2.34)$$

where $f_0(E)$ is the equilibrium Fermi distribution function

$$f_0(E) = \frac{1}{1 + e^{(E-\mu)/k_B T}} \Big|_{\mu=E_F}. \quad (2.35)$$

The voltage difference between leads is $V = (\mu_L - \mu_R)/e$ and the conductance is

$$G = \frac{I}{V} = \frac{2e^2}{h} \int_0^\infty T(E) \left(\frac{\partial f_0}{\partial \mu} \right) dE. \quad (2.36)$$

The factor $\frac{e^2}{h}$ is known as quantum conductance. In the low temperature limit ($k_B T \ll E_F$), the derivative of the equilibrium Fermi function can be assumed nearly equal to Delta function ($\frac{\partial f_0}{\partial \mu} \approx \delta(E_F - E)$). Under this approach conductance can be simply written as

$$G = \frac{2e^2}{h} T(E_F), \quad (2.37)$$

where E_F is the Fermi energy of the system. This equation is called Landauer formula for the conductance. According to this formula the conductance of a thin wire is finite even for small values of length l . If we have a large device where the number of conducting modes is infinite the conductance rises to infinity, this means that zero resistance. But such a large device with very large number of conducting modes can not be considered to be a nanodevice. However, this kind of electron conductance is seen in many systems such as quantum wires, atomic chains.

Landauer formalism was generalized by Büttiker for multi-terminal systems. The transmission is now not only from the left contact to the right, but between every pair of contacts (Büttiker et al., 1985). In the multi terminal system the conductance from lead β to lead α can be written via Equation 2.36 and Equation 2.37

$$G_{\alpha,\beta} = \frac{I}{V} = \frac{2e^2}{h} \int_0^\infty T_{\alpha,\beta}(E) \left(\frac{\partial f_0}{\partial \mu} \right) dE \quad (2.38)$$

and

$$G_{\alpha,\beta} = \frac{2e^2}{h} T_{\alpha,\beta}(E_F). \quad (2.39)$$

CHAPTER THREE

RESULTS AND DISCUSSIONS

3.1 Motivation

Recent advances in fabrication of high-mobility low-dimensional semiconductor structures have prompted the large number of works in this area. The double low-dimensional semiconductor structures, such as double QWs, double QWRs and double QDs, constituted by restricting the motion of charge carriers are attractive phenomenon in from various branches of physics to chemistry (Pedram et al., 2010). The one-dimensional double well potential is a well-known and topical problem in quantum mechanics (Bhattacharya, 1985). This potential consisting of two valleys separated by the potential barrier is utilized to study the properties of numerous systems. The study done by Bender et al. (Bender & Wu, 1973) for obtaining the energy eigenvalues of quantum anharmonic oscillator has been quite impressive that has been followed by a great number of works. The energy eigenvalues of double well anharmonic oscillator are investigated using perturbative or nonperturbative methods by research. Banerjee et al. (Banerjee & Bhatnagar, 1978) obtained the eigenvalues of two-well oscillator by a nonperturbative method WKB. Hodgson et al. (Hodgson & Varshni, 1989) performed an analytic procedure to calculate accurate wavefunctions and energy eigenvalues of a double minimum potential with almost degenerate levels. The effect of an external field onto the behavior of the lowest eigenvalues of the quantum double well anharmonic oscillator was surveyed by der Straeten et al. (der Straeten & Naudts, 2006). Also, Witwit (Witwit, 1996) calculated energy levels of nonsymmetric double well potentials in one-, two- and three-dimensional systems for large values of the depth of the potential.

Furthermore, a great deal of theoretical (Thomas et al., 1999; Wang et al., 2005) and experimental (Moon et al., 1999; Yamamoto et al., 2005) work has been devoted to survey the electronic and transport properties of double QWRs, consisting of two parallel long QWRs coupled through a potential barrier allowing

the tunneling of electrons between them. Shi et al. (Shi & Gu, 1997) investigated the magnetotransport properties of dual QWRs for different heights of barrier in the presence of magnetic fields. Numerical results show that if the potential barrier is height enough, *i.e.* the coupling between the QWRs is weak so they are approximately independent, the lower energy eigenvalues are closely bunched as a couple. Lyo and his collaborates (Lyo & Huang, 2001) searched the energy spectrum, magnetization and magnetotransport properties for tunnel-coupled double QWRs subjected to an external magnetic field. The electronic transport properties of double QWRs by considering impurity, perpendicular magnetic field and correlated disorder were investigated by Korepov (Korepov & Liberman, 1999). Gudmundsson et al. (Gudmundsson & Tang, 2006) analyzed the energy spectrum, electronic transport and probability density of electron waves of a double QWR system containing a coupling element in the middle barrier between the two parallel QWRs under the influence of magnetic field.

The study of spin-orbit interaction in quantum confined structures is important from the standpoint of their fundamental role in spintronic applications. These devices are based on manipulating and controlling the spin orientation by utilizing spin-orbit interaction which arises from inversion asymmetry properties of low-dimensional systems. Structural inversion asymmetry induces Rashba spin-orbit interaction which can be tuned by changing the gate voltages whereas bulk inversion asymmetry gives rise to Dresselhaus spin-orbit interaction which contribution can be altered by sample thickness or electron density.

Semiconductor nanowires are powerful class of materials that through a controlled growth and organization can be produced in a wide range with a compositional and/or doping modulation (Li et al., 2006). Spatially separated two identical quasi-one-dimensional systems can be coupled by an additional lateral confinement to produce a double QWR structure (Fischer et al., 2006b). Band structure behaviors, spin texture and transport properties of double QWRs have attracted immense interest in respect of promising remarkable new devices, faster, smaller, and more powerful for the applications in quantum computing, spin-field effect transistors and spin filters (Upadhyaya et al., 2008b; Scheid et al., 2008). It is therefore important to

characterize electronic energy spectrum of double QWRs in the presence of different external agents, in order to gain a better understanding of the conductance and spin-related properties. In this purpose Karaaslan et al. (Karaaslan et al., 2015) investigated the effects of Rashba spin-orbit interaction on the electronic energy dispersion and conductance of double QWR under the influence of perpendicular magnetic field. Lastly, the electronic, spin and transport properties of double QWR subjected to an in-plane magnetic field have been searched by Gisi et al. (Gisi et al., 2016a) incorporating both Rashba and Dresselhaus spin-orbit interactions. Recently some experimental techniques have been developed to control a coupling of spin to electric field. According to the result of these experiments, an in-plane magnetic field is more appropriate to obtain a prominent spin resonance. Spin-orbit interactions generate an effective in-plane magnetic field which gives rise to an drift-driven in-plane spin polarization, and the summation of an external magnetic field and spin-orbit induced effective magnetic field leads to observe surprising spin polarization (Edelstein, 1990; Kato et al., 2004). In the light of these findings it is worth to investigate the effect of an in-plane magnetic field and electric field on the energy, spin texture and conductance of double QWR considering the spin-orbit interaction.

3.2 System and Its Variables

In this thesis, we consider a quasi-one-dimensional quantum wire with Rashba and Dresselhaus spin-orbit couplings under the influence of external magnetic and electric field. The confinement potential representing the local depletion of stacked two-dimensional gases contained in double-quantum-well heterostructures with controllable tunneling barrier thickness can be modeled by a double quartic-well confinement potential given as

$$V(y) = \frac{1}{4}\lambda\left(y^2 - \frac{\mu^2}{\lambda}\right)^2, \quad (3.1)$$

where μ and λ are positive, adjustable structural parameters controlling the height of the barrier between wells and the width of wells. In-plane magnetic field applied with an arbitrary orientation is chosen as $\mathbf{B} = B(\cos\phi\mathbf{e}_x + \sin\phi\mathbf{e}_y)$. Here ϕ indicates the

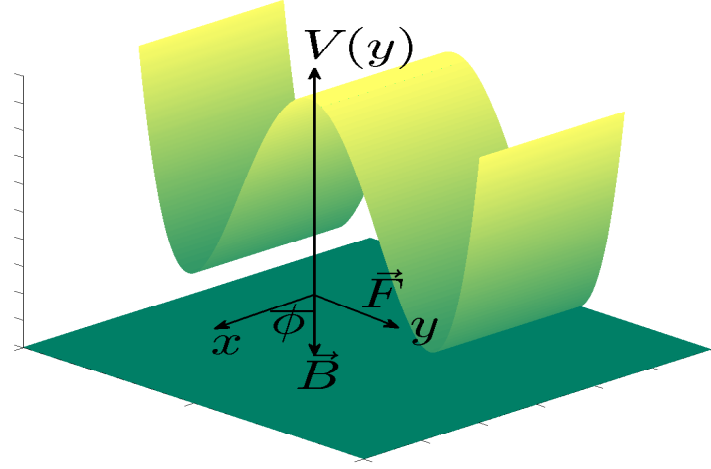


Figure 3.1 The model of the double quantum wire structure and orientation of magnetic and electric fields.

azimuthal angle between the magnetic field and x -direction. The external electric field is applied in the growth direction of the system. The single particle Hamiltonian of the systems is given by

$$\mathcal{H} = \left[\frac{p_x^2 + p_y^2}{2m^*} + V(y) + eFy \right] \sigma_0 + \frac{1}{2} g^* \mu_B B (\cos \phi \sigma_x + \sin \phi \sigma_y) + \mathcal{H}_R + \mathcal{H}_D \quad (3.2)$$

where m^* is effective mass, g^* and μ_B are the effective Lande-g factor and Bohr magneton, respectively, σ_x and σ_y represent the Pauli spin matrix components. Here the first term consists of the kinetic energy, confinement potential and Stark effect whereas second term describes Zeeman effect. Note that p_x and p_y are the actual components of linear momentum. We use symmetric gauge $A = (B_y z, -B_x z, 0)$ and choosing the confinement to be located at $z = 0$, we get $A = 0$. The magnetic field enters the Hamiltonian only Zeeman effect. In order to confine electrons to nanostructure devices, sharp potentials are necessary, which lead to non-negligible spin-orbit interactions, especially in systems with structural asymmetry such as semiconductor heterostructures. This interaction can be used to achieve control of manipulations of electron spin. And the last two terms \mathcal{H}_R and \mathcal{H}_D are Rashba and

Dresselhaus spin-orbit interactions that are given as

$$\mathcal{H}_R = \frac{\alpha_R}{\hbar}(p_y\sigma_x - p_x\sigma_y), \quad (3.3)$$

$$\mathcal{H}_D = \frac{\alpha_D}{\hbar}(p_x\sigma_x - p_y\sigma_y). \quad (3.4)$$

α_R is Rashba spin-orbit coupling parameter that can be tuned by changing gate voltages and α_D corresponds Dresselhaus spin-orbit coupling factor which can be varied sample thickness or electron density. Dresselhaus spin-orbit coupling term has two components, one linear in the electron momentum and the other cubic. The cubic Dresselhaus term is generally neglected because its contribution is smaller than the linear one. In our study, we ignore the cubic Dresselhaus spin-orbit contribution.

The eigenfunctions of Hamiltonian can be written as a product of plane-waves propagating along the x -axis and y -dependent spinor part as follows:

$$\psi_{nk_x}(\mathbf{r}) = \frac{e^{ik_x x}}{\sqrt{L}} \begin{pmatrix} \varphi_{nk_x}(y, \uparrow) \\ \varphi_{nk_x}(y, \downarrow) \end{pmatrix} \quad (3.5)$$

where φ_{nk_x} is spinor function. We use integer numbers $n = 1, 2, 3, \dots$ to label different energy subbands and introduce a continuous wave number k_x . The finite- T frame formalism is used as a numerical trick, but results of actual calculations are for $T = 0$ case. σ_a ($a = x, y, z$) being the corresponding Pauli matrix, we can calculate spin magnetization components,

$$m_a(y) = \sum_n \frac{L}{2\pi} \int dk \langle \psi_{nk} | \delta(r_i - r) \sigma_a | \psi_{nk} \rangle_{r_i} f_\beta(\epsilon_{nk}, \mu), \quad (3.6)$$

where $f_\beta(\epsilon_{nk_x})$ is the Fermi distribution.

The energy eigenvalues and eigenfunctions of double QWR are obtained by using the finite element method (FEM) which is a powerful numerical method for the solutions of the physical systems. FEM is a very important tool of scientific and engineering analysis. It provides us a significant simplification to form the matrix elements and also to calculate the integrals in two dimensions (Hutton,

2004; Zienkiewicz et al., 2005). In FEM, the physical region is discretized and the wave functions are represented by piecewise polynomials (Ram-Mohan, 2002). The discretization of the physical region enables accurate representation of complex geometries and inclusion of dissimilar materials. And also to reveal local effects, it allows accurate representation of the solution within each element (Sarikurt, 2013; Reddy, 1993). The results can be obtained with a very high accuracy via FEM.

The fundamental principle is to construct Galerkin expression which will be minimalized by the variational variables of the system. For this purpose, the Schrödinger equation with wanted wave function is written down, the equation is multiplied by hermitian conjugate of the wave function on the left hand and this expression is integrated over the work space. A wavefunction family which minimalize the G expression also minimalize the energy of the system.

In FEM formalism, the Hamiltonian in quantum mechanical formulation is given as

$$\mathcal{H} = \sum_0^{\infty} \left\{ \frac{1}{n!} \frac{\partial^n \mathcal{H}}{\partial p_{\xi}^n} \Big|_{p_{\xi}=0}, P_{\xi}^n \right\}, \quad (3.7)$$

where p_{ξ} is the dimensionless canonical momentum. And the $\{\}$ parenthesis defines a specific operation such as $\{A, B\} = \frac{1}{2}(AB + BA)$.

The scaled form of the Hamiltonian of the system under investigation can be written as:

$$\begin{aligned} \mathcal{H} = & \frac{1}{2} \sigma_0 p_{\tilde{y}}^2 + (\eta_R \sigma_x - \sigma_y \eta_D) p_{\tilde{y}} \\ & + \left[\left(\frac{1}{2} \mathcal{K}_0^2 + \frac{1}{4} \tilde{\lambda} \tilde{y}^4 - \frac{1}{2} \tilde{\mu}^2 \tilde{y}^2 + \frac{1}{4} \frac{\tilde{\mu}^4}{\tilde{\lambda}} + \tilde{F} \tilde{y} \right) \sigma_0 \right. \\ & \left. + \left(\frac{1}{2} \mathcal{B} \cos \phi + \eta_D \mathcal{K}_0 \right) \sigma_x + \left(\frac{1}{2} \mathcal{B} \sin \phi - \eta_R \mathcal{K}_0 \right) \sigma_y \right]. \end{aligned} \quad (3.8)$$

Characteristic length corresponding to harmonic oscillator ($l_0 = \sqrt{\hbar/m^* \omega_0}$) is taken as a length scale and correspondingly the obtained energies are in $\hbar \omega_0$ units. And also, we define dimensionless parameters: $\mathcal{K}_0 = k_x l_0$, $\tilde{y} = y/l_0$, $p_{\tilde{y}} = \frac{1}{i} \frac{\partial}{\partial \tilde{y}}$ and $\tilde{F} = e F l_0 / \hbar \omega_0$. And throughout our work we use dimensionless form of the structural parameters:

$\tilde{\mu} = \mu / \sqrt{m^* \omega_0}$ and $\tilde{\lambda} = \lambda \hbar \omega_0 / (m^* \omega_0^2)^2$. Lastly \mathcal{B} is proportional to Lande-g factor and the strength of magnetic field ($\mathcal{B} = (eg^*B)/(2m_0\omega_0)$, e and m_0 is the charge and the mass of electron, respectively).

3.3 Numerical Results

In this study, we have investigated the electronic structure, spin and transport properties of double QWRs formed by a symmetric, double quartic-well potential subjected to an in-plane magnetic field by taking into account Rashba and Dresselhaus spin-orbit couplings. The energy dispersion relation of the system is analyzed for different strengths of spin-orbit interactions, magnitude and direction of magnetic field, magnitude of electric field and for different values of structural parameter. Figure 3.2 presents the shape of double-well potential. The other structural parameter is set $\tilde{\lambda} = 1$. The smaller values of $\tilde{\mu}$, in which the tunneling effects are in action, called as strong coupling is shown with light blue and pink lines. On the other hand, in the weak coupling limit (green and blue lines), characterized by large values of $\tilde{\mu}$, tunneling of electrons can be negligible and also the wires can be considered as two individual QWRs.

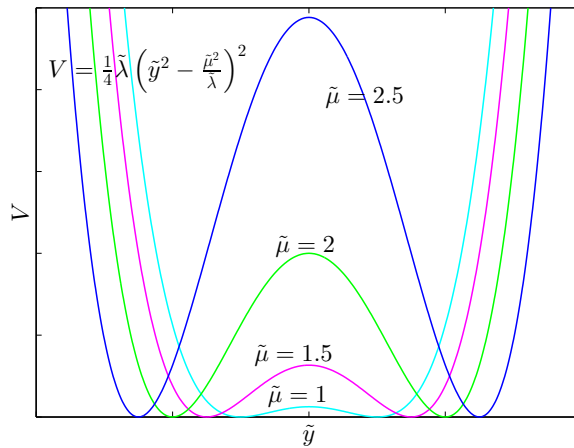


Figure 3.2 The potential profile of double quantum well potential for different values of structure parameter.

3.3.1 Energy Dispersion

Zeeman splitting is proportional to Lande-g factor (g^*) and external magnetic field. So the strength of the spin splitting is controlled by g^* and narrow band-gap materials with a large g^* factor such as InAs or GaInAs are highly desirable in the quest to develop electronic devices that require only the smallest magnetic fields to achieve spin-functional operations (Martin et al., 2008). Because of this, in this study, we carried out our numerical calculations for a InAs double QWR with corresponding bulk parameters: $g^* = -15$, $m^* = 0.03m_0$. The experimental values of spin-orbit coupling constants $\alpha_{R,D}$ are in order of 10^{-11} eV·m (Pramanik et al., 2007; Könnemann et al., 2005). We set $\hbar\omega_0$ to 2 meV and for the sake of simplicity, one of the structural parameters controlling the shape of the double-well potential is fixed, $\tilde{\lambda} = 1$. In the present work characterization of the spin-orbit regime is realized by the ratio of the strength of spin-orbit interaction to the confinement potential energy, $\Delta_{R(D)} = m^* \alpha_{R(D)}^2 / 2\hbar^3 \omega_0$. By virtue of this fact, parameters $\Delta_{R(D)} \gtrsim 0.1$ define the strong spin-orbit regime and $\Delta_{R(D)} < 0.1$ accounts for the weak spin-orbit regime. And the dimensionless value of electric field is chosen as $\tilde{F} = 1$ which corresponds to electric field $F = 0.6$ kV/cm.

Physical properties of semiconductor structures are often determined by the energy spectrum of charge carriers. Investigation of dispersion relation is very useful to find out many prominent effects like spin texturing which is mainly utilized in the field of electronic and spintronics properties which constitutes the base of optoelectronic devices. Applying external magnetic and electric fields introduce additional features in the subband structure that may be used to control and modulate the intensity output of devices. In this thesis, we have aimed to reveal the qualitative hallmarks of spin-orbit interaction and in-plane magnetic field and electric field in double QWR so a part of result section is devoted to present some illustrative examples rather than study whole parameter space.

Initially, in order to identify how the spin-orbit interaction affects the energy subband structure of double QWR, in Figure 3.3 we give $E - k$ graphs for different

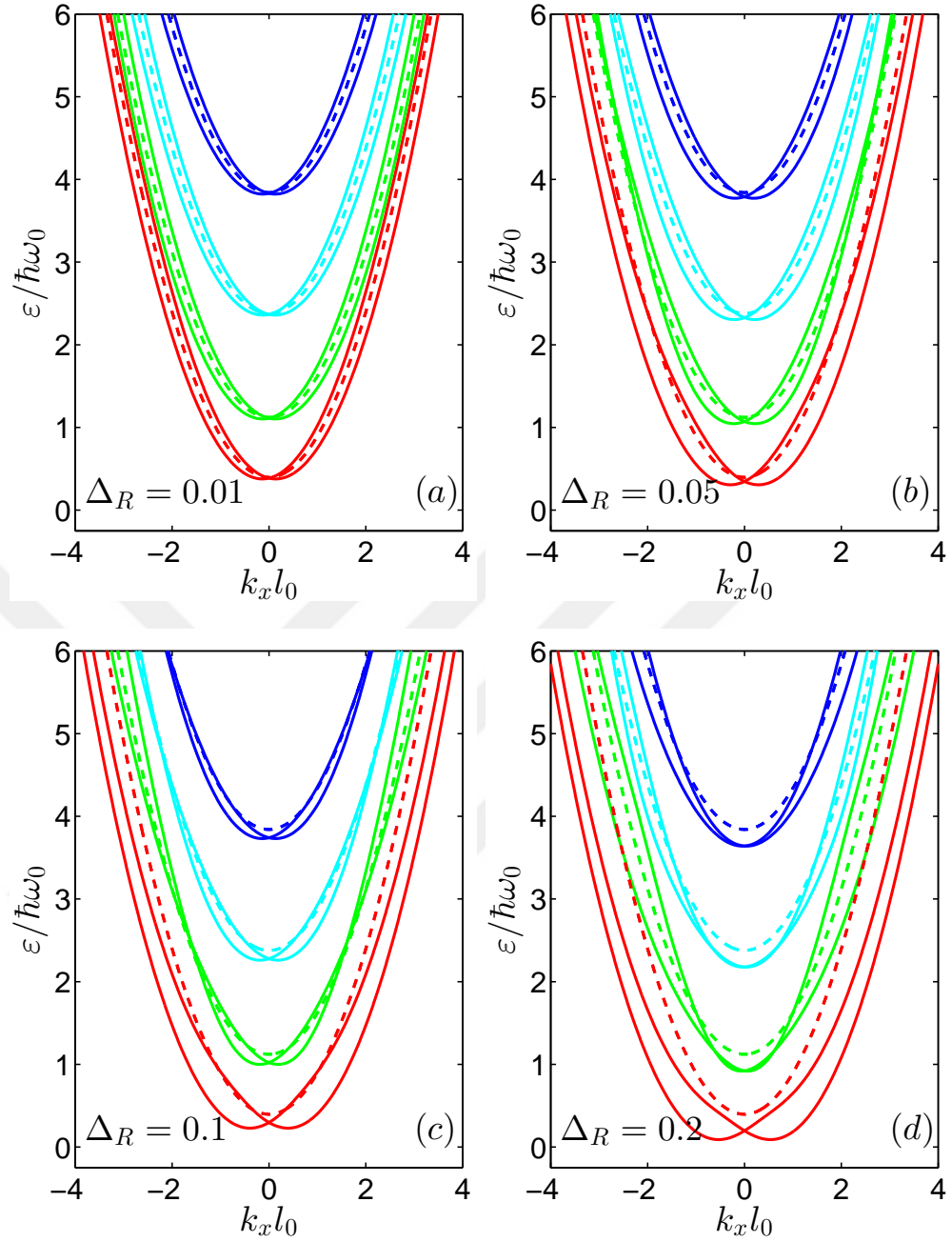


Figure 3.3 Variation of the energy dispersion curves of electrons in a double QWR for different strength of Rashba spin-orbit interaction in the absence of magnetic/electric fields. The structural parameter is set $\tilde{\mu} = 1$. The strength of Rashba spin-orbit coupling is increased such as a) $\Delta_R = 0.01$, b) $\Delta_R = 0.05$, c) $\Delta_R = 0.1$ and d) $\Delta_R = 0.2$. The dashed lines correspond the case of $\Delta_R = \Delta_D = 0$ and $B = \tilde{F} = 0$.

strengths of Rashba spin-orbit coupling in the absence of magnetic and electric fields. We show only Rashba spin-orbit contribution because in the absence of magnetic and electric fields the spectral properties of electrons subject to Rashba or linear Dresselhaus spin-orbit interactions are exactly the same. This behaviour can be

expressed as follows: the Rasha Hamiltonian Equation 2.18 and linear Dresselhaus Hamiltonian Equation 2.20 are equivalent under the unitary transformation rotating the spin Pauli matrices $\sigma_x \rightarrow \sigma_y$, $\sigma_y \rightarrow \sigma_x$ and $\sigma_z \rightarrow -\sigma_z$ (Lucignano et al., 2008). Also we consider strong coupling limit, $\tilde{\mu} = 1$, in which tunneling effect between QWRs is in action. Both of subfigures, the dashed lines represent the energy spectra of double QWR with no spin-orbit interaction, magnetic and electric fields. It is clear from the Figure 3.3 that all subbands are two-fold degenerate for spin-up and spin-down states for all values of $k_x l_0$ presented with dashed lines. Taking into account even a weak Rashba spin-orbit interaction lifts the spin degeneracy of the subbands for nonzero wave vectors and produces an energy splitting proportional to k_x . When the strength of Rashba spin-orbit coupling is increased, the energy subbands shift to lower energy values as seen in all subfigures. In the weak Rashba spin-orbit regime characterized by $\Delta_R = 0.01$, the spin-split energy levels for different subbands get closer in lower subbands. With further increment in Rashba spin-orbit interaction, crossings between same levels with opposite spins appear. These crossings occur at lower energy values for the larger values of spin-orbit strengths.

When the effect of Dresselhaus spin-orbit coupling is switched on, it leads to a rather complex energy spectra. Figure 3.4 displays the combined effect of Rashba and Dresselhaus spin-orbit couplings. It is clear from the both subfigures, the spin-orbit interaction gives rise to a visible shift in energy subbands compared to dashed lines. The crossings which leap out in the pure Rashba case ($\Delta_R = 0.2$) vanish by including an even weak Dresselhaus spin-orbit interaction ($\Delta_D = 0.01$) as seen in Figure 3.4(a) compared to Figure 3.3(d). The energy subbands are nearly parabolic in this regime. Simultaneous contribution of both spin-orbit interaction terms in strong regime ($\Delta_R = 0.2$ and $\Delta_D = 0.1$) results in stronger deviation from parabolicity of the subbands and downward shifting of energy displayed as in Figure 3.4(b). We observe local extrema that can be attributed as an anomalous plateaus near $k_x l_0 = 0$ which plays an important role in the explanation of anomalous steps in conductance.

We examine the influence of an in-plane magnetic field on the subband structure because it has an important role to clarify the beating pattern in the magnetoresistance

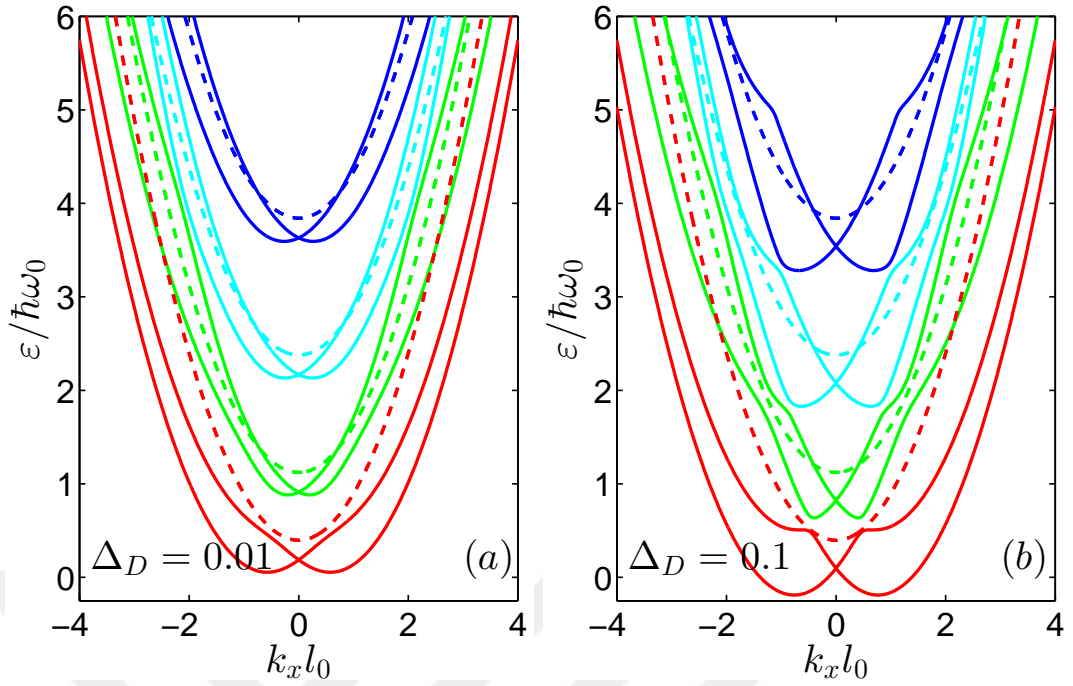


Figure 3.4 Subband energy spectra as a function of linear momentum $k_x l_0$ for different spin-orbit coupling regimes when magnetic and electric fields are not considered. a) Strong Rashba and weak Dresselhaus spin-orbit couplings $\Delta_R = 0.2$ and $\Delta_D = 0.01$ b) Both of spin-orbit interactions are in strong regime $\Delta_R = 0.2$ and $\Delta_D = 0.1$. The dashed lines correspond to the case of $\Delta_R = \Delta_D = 0$ and $B = \tilde{F} = 0$.

and absorption spectra of magneto-optic transitions. The magnetic field moves the bottoms of two parabolas in each level in opposite direction along the energy axis via Zeeman effect and changes the character of the energy spectrum as can be seen in Figure 3.5. It is obtained that, when spin-orbit interaction is considered the zero- k spin-splitting energy is not equal to the Zeeman spin-splitting given by $g^* \mu_B B$, it also depends on the strength of spin-orbit interaction. Coexistence of spin-orbit interaction and magnetic field gives rise to peculiarities in the energy spectrum (Datta & Das, 1990; Bandyopadhyaya & Cahay, 2004; Ganichev et al., 2002). We searched the energy spectra of double QWR for four different orientations ($\phi = 0, \pi/6, \pi/3, \pi/2$) of a constant magnetic field (1 T) for the strong spin-orbit regime characterized by $\Delta_R = 0.2$ and $\Delta_D = 0.1$. When magnetic field is not considered, the spin-orbit interaction gives rise to symmetric double minimum structures in the energy subband which is shown by dashed lines, but including the magnetic field breaks down this symmetry and introduces additional complexities in the subband structure as shown

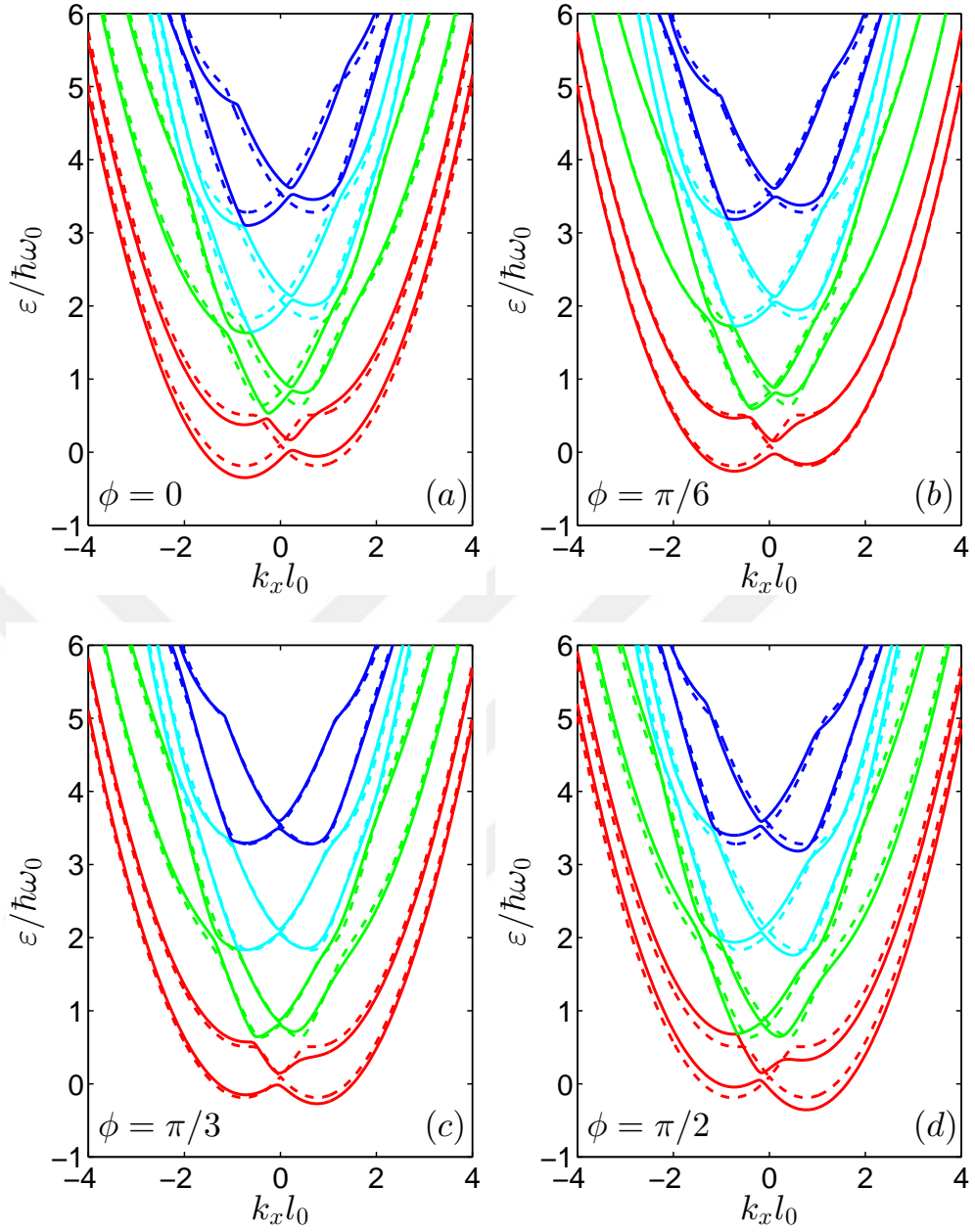


Figure 3.5 Energy dispersion curves of electrons in a double QWR with different orientation of magnetic field: a) $\phi = 0$, b) $\phi = \pi/6$, c) $\phi = \pi/3$, and d) $\phi = \pi/2$. The magnitude of magnetic field and the strength of spin-orbit interactions are fixed at $B = 1$ T, $\Delta_R = 0.2$ and $\Delta_D = 0.1$. The dashed lines correspond the case of $\Delta_R = 0.2$, $\Delta_D = 0.1$ and $B = 0$.

in Figure 3.5. This asymmetry can be explain via Equation 3.8. For a magnetic field directed along the wire axis, $\cos \phi = 1$ and $\mathcal{B} \cos \phi$ contributes negative values to Hamiltonian for all k_x . Also the Dresselhaus spin-orbit term is negative for $k_x < 0$, and positive for $k_x > 0$. For negative (positive) k_x values, due to the same (opposite) signs

of Zeeman and Dresselhaus spin-orbit interaction, their overall (net) effect contributes to the Hamiltonian. This explains why the minimum point of energy subband occurs at negative k_x as seen in Figure 3.5(a). In the case of magnetic field orientated along the perpendicular axis of wire ($\phi = \pi/2$), $\sin \phi = 1$ and $\mathcal{B} \sin \phi$ is a nontrivial negative value. For positive (negative) k_x values, due to the same signs of Rashba spin-orbit interaction and magnetic field, their overall (net) effect contributes to the Hamiltonian. This elucidate the shifting of the minimum of energy to positive k_x as observed in Figure 3.5(d). For the other orientations of magnetic field such as $\phi = \pi/3$, $\phi/6$ (Figure 3.5(b) and Figure 3.5(c)) the asymmetries in the subbands can be explained in a similar way. Additionally, the crossings and anticrossings arising from spin-orbit interaction are observed as it is evident from the Figure 3.5. In all panels, conspicuous band gaps and local extrema leap out near $k_x l_0$. These maxima leads to observe anomalous steps in the conductance.

Applying an external electric field offers a way to realise such a control over the QWR characteristics for a desired device operation. Figure 3.6 is devoted to present the effect of external electric field on to the energy spectra of double QWR for three orientations ($\phi = 0, \pi/4, \pi/2$) of a constant magnetic field 1 T with considering strong spin-orbit coupling regime characterized by $\Delta_R = 0.2$ and $\Delta_D = 0.1$. The dashed lines represent the energy spectrum of double QWR with spin-orbit interaction and magnetic field whereas the solid lines denote the case involving effect of electric field. In the presence of an in-plane magnetic field the orbital effects are absent and the electric field induces Stark shift in the energy spectra characterized by F^2 -dependence. The effect of external electric field ($\tilde{F} = 1$) on the subbands is indicated by the solid lines in Figure 3.6. It is clear from the figure that the energy spectra exhibits a downward shift only without any lateral displacement. Also, the electric field induces larger energy gaps between spin-split levels. This considerable changes in the energy spectrum of the carriers may be used to control and modulate the intensity output of devices.

It is useful at this stage to inquire to what extent the structural parameter $\tilde{\mu}$ affects the system. Figure 3.7 presents the energy dispersion behavior of the subbands of the double QWR comprising of strong spin-orbit interaction ($\Delta_R = 0.2$ and $\Delta_D = 0.05$) and

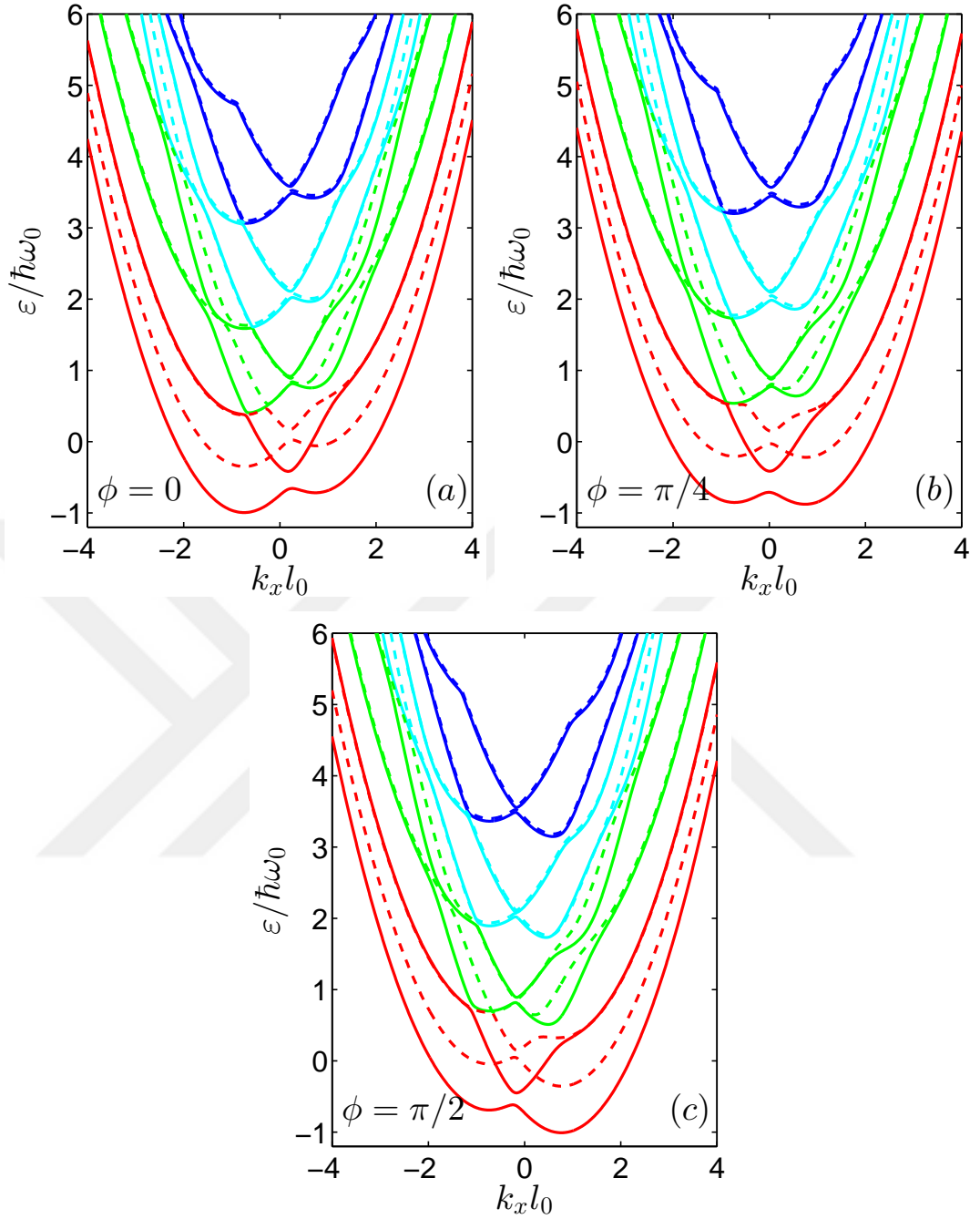


Figure 3.6 The Stark effect on the energy subband structure of double quantum wire for different directions of magnetic field in the presence of strong spin-orbit interactions in the strong coupling limit, namely $\Delta_R = 0.2$, $\Delta_D = 0.1$, $B = 1$ T, $\tilde{\mu} = 1$, $\tilde{F} = 1$. The dashed lines correspond the zero electric field case.

magnetic field (1 T) orientated with an angle $\phi = \pi/4$. The dashed lines correspond to the pure case (no spin-orbit interaction and no magnetic field) in all subfigures. The most striking feature of the figure is that the energy band levels shift to upper

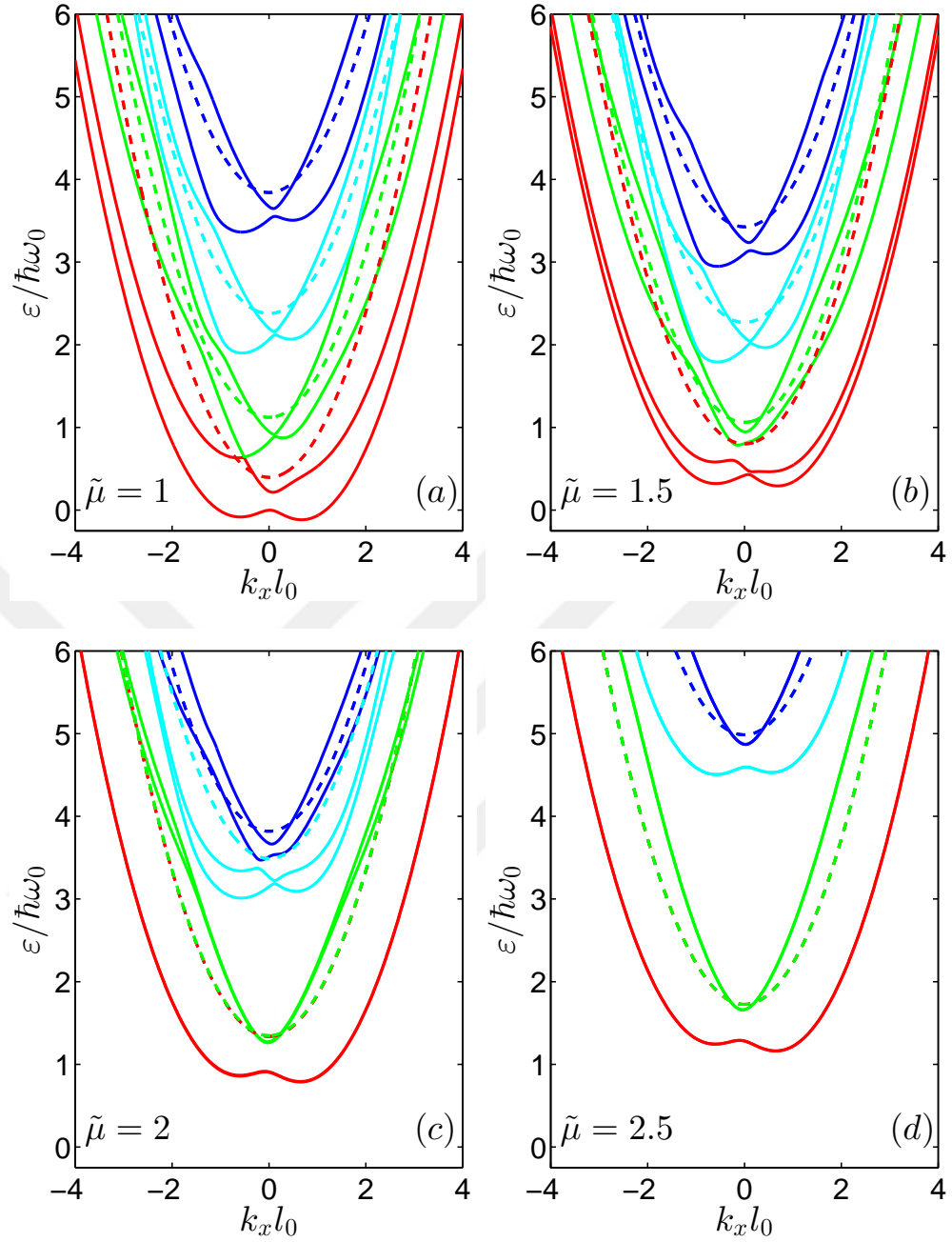


Figure 3.7 Energy spectrum of double QWR in the presence of strong spin-orbit interaction ($\Delta_R = 0.2$, $\Delta_D = 0.05$) and an external magnetic field ($B = 1$ T). The orientation angle is chosen as $\phi = \pi/4$ where different values of $\tilde{\mu}$ are taken: a) 1, b) 1.5, c) 2, and d) 2.5. The dashed lines correspond the case of $\Delta_R = \Delta_D = 0$ and $B = 0$.

values and are grouped in pairs by starting from the lowest level with increasing values of $\tilde{\mu}$ for both solid lines and dashed lines as depicted in the figure. Small values of $\tilde{\mu}$ correspond the strong coupling limit (Figure 3.7(a), Figure 3.7(b)) in which the tunneling effect between wires is allowed. In this limit, energy levels have

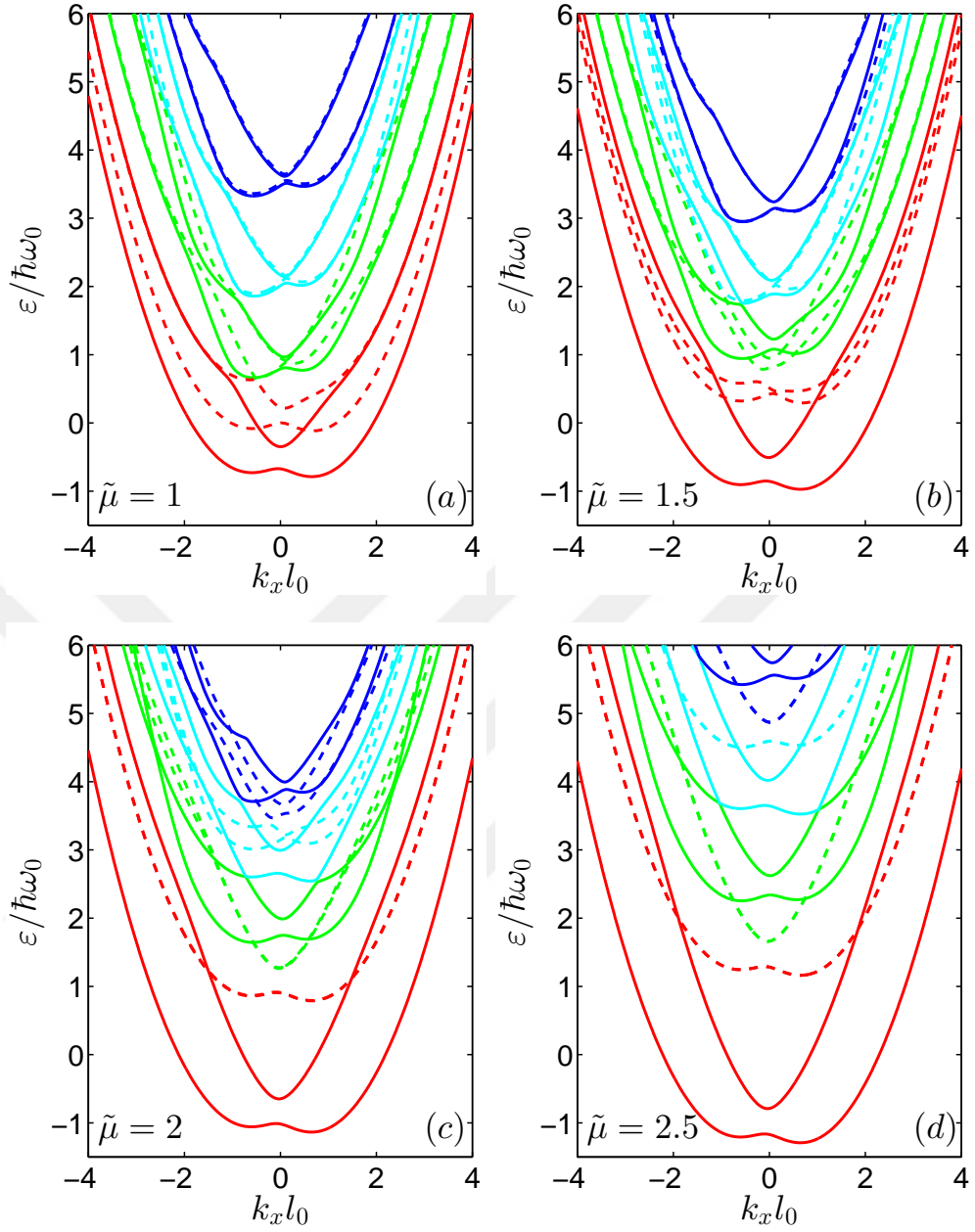


Figure 3.8 Variation of the energy dispersion curves of electrons in a double quantum wire in the presence of strong spin-orbit interaction ($\Delta_R = 0.2$, $\Delta_D = 0.05$) and an external magnetic field ($B = 1$ T) and electric field ($\tilde{F} = 1$). The orientation angle is chosen as $\phi = \pi/4$ where different values of $\tilde{\mu}$ are taken: a) 1, b) 1.5, c) 2, and d) 2.5. The dashed lines correspond the case $\tilde{F} = 0$.

local minimum and maximum points which give rise to the appearance of intriguing properties in conductance. On the other hand, in the weak coupling limit (Figure 3.7(c), Figure 3.7(d)), characterized by large values of $\tilde{\mu}$, tunneling of electrons can be negligible and also the wires can be considered as two individual QWRs. The energy

spectrum of this decoupled double QWR is a superposition of the dispersion curves of individual QWRs. The crossings and anticrossings between energy levels which appear in the strong coupling limit vanish in the weak coupling limit. Further the energy subbands exhibit a smoother behavior.

Figure 3.8 presents the energy spectra of double QWR for different values of $\tilde{\mu}$ ((a) 1, (b) 1.5, (c) 2 and (d) 2.5) in the presence of spin-orbit coupling and magnetic field with the values of $\Delta_R = 0.2$, $\Delta_D = 0.1$, $B = 1$ T, and $\phi = \pi/4$. The dashed lines correspond the case $\tilde{F} = 0$ as seen in Figure 3.7 solid lines. In the presence of an in-plane magnetic field the orbital effects are absent and the electric field induces Stark shift in the energy spectra characterized by F^2 -dependence. It is clear from the figure that the applied electric field gives rise to a downward shift energy subbands for all values of $\tilde{\mu}$. The most striking feature is the separation of two sets of dispersion curves belonging to individual quantum numbers in wave-number space in the weak coupling limits. In this limit the energy subbands are two fold degenerate for spin-up and down as seen in Figure 3.8(c) and Figure 3.8(d) with dashed lines. Applying external electric field shift this degeneracy and induces larger energy gaps between spin-split levels. The separation distance is proportional to the magnitude of electric field. This phenomenon manifests itself in both spin textures and conductivity.

3.3.2 Spin Textures

In the recent years, both experimental and theoretical physicists has focused on spintronics. This field relies on the manipulation of spins in semiconductor systems. A key role in the success of semiconductor spintronics is to carry out controllable manipulation of electron spins. Semiconductor heterostructures offer the possibility of electric control of spins via intrinsic spin-orbit interactions which stem from the inversion asymmetry properties characteristic of these systems. Also the spins can be manipulated by applying external magnetic and electric fields to the systems. External magnetic field strongly alters the energy spectra and leads to larger energy gaps and it effects the psysical properties of the semiconductor such as spin and conductance. An

external electric field applied along the growth direction of the wire induces Stark shift in the subband structure and also it leaves its marks on the spin properties.

Traditional approaches on the usage of the spin are based on the alignment of a spin relative to a reference such as an applied magnetic field or magnetization orientation. Device operations depends in a predictable way on the degree of the alignment. Adding the spin degree of freedom to conventional semiconductor charge-based electronics or using the spin degree of freedom alone will add substantially more capability and performance to electronic products (Governale & Zülicke, 2002). The success of these ventures depends on a deeper understanding of fundamental spin interactions, controlling and manipulating spin orientations in semiconductors. In the presence of spin-orbit interactions spin is not a good quantum number and it is possible to find spin textures across the wire with the spin direction depending on k_x and the wire transversal coordinate y . In contrast, when spin-orbit coupling is not incorporated, the states are exact eigenspinors even in the presence of in-plane magnetic field and electric field. Thus, observation of a clear spin texture can be interpreted as a signature of spin-orbit interactions. Whenever the typical spin-orbit interaction energy scale becomes comparable to the subband splitting, emergence of a sizable spin z component due to anticrossings between neighboring subbands precludes a definition of common spin-quantization axis (Governale & Zülicke, 2002). The interplay between external magnetic/electric fields and spin-orbit interactions gives rise to observe surprising spin textures. Zeeman effect tends to align the spin along the external magnetic field, whereas the spin-orbit interaction is responsible for the randomization of the spin direction. The concept of spin texturing is crucial for spintronics in two respects: it is closely related to that of spin current which is measured as a change in the local spin and it represents the spatial distribution of the effective magnetic field due to spin-orbit interaction.

In the following part of the study, we illustrate to what extend effects of spin-orbit interaction and magnetic field modify the spin orientation. In this respect we calculated spin expectation values $\langle \sigma_a \rangle = \Psi_{nk}^\dagger \sigma_n \Psi_{nk}$ where $a = x, y, z$.

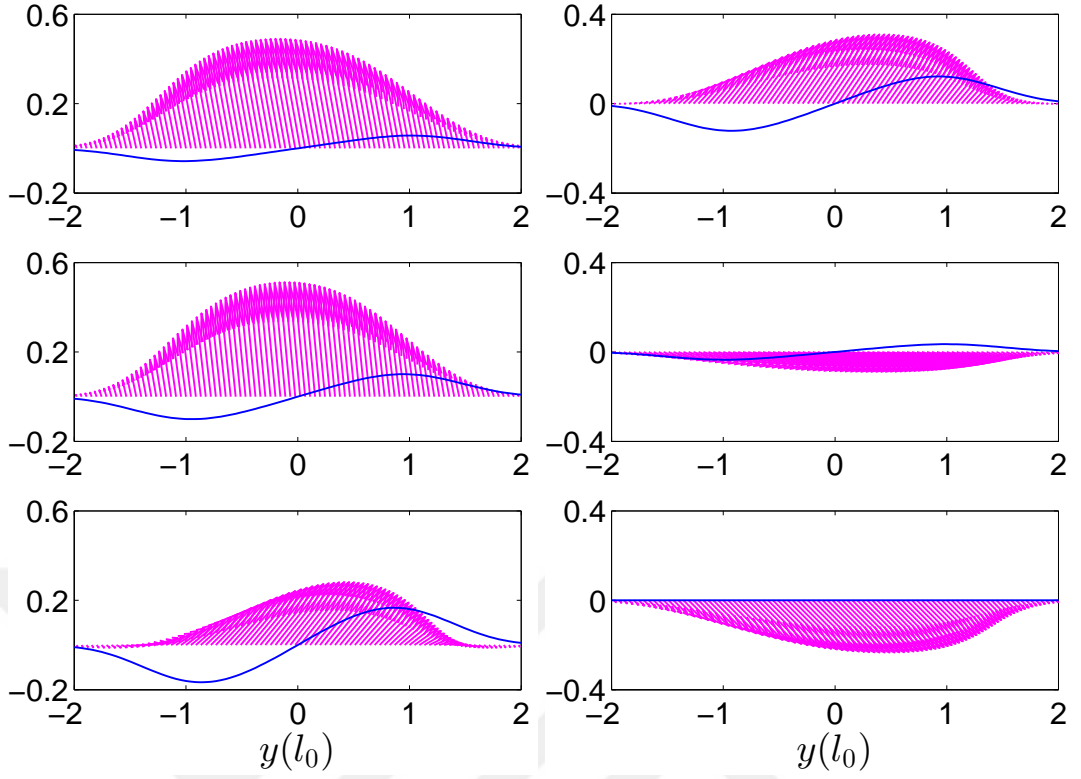


Figure 3.9 Spin textures across the wire (y direction in l_0 units) in the presence of both type of spin-orbit couplings ($\Delta_R = 0.05$, $\Delta_D = 0.2$) and external magnetic field (3 T) oriented along the wire axis (left panel) and perpendicular to the wire axis (right panel). Plots from the top to down correspond to momentum $k_x l_0 = -0.69, 0.0, 0.69$ where arrow length is proportional to spin density. Blue solid lines correspond to the z component of magnetization.

In-plane spin distributions for the lowest subband at three different momenta are shown in the Figure 3.9 in the presence of strong spin-orbit coupling characterized by $\Delta_R = 0.05$ and $\Delta_D = 0.2$ and an external magnetic field ($B = 3$ T) oriented along the wire axis $\phi = 0$ in the left panel and perpendicular to the wire axis $\phi = \pi/2$ in the right panel of Figure 3.9. The vector plot shows the in-plane spin for different momenta such as $k_x l_0 = -0.69, 0, 0.69$ from top to down respectively whereas the solid line corresponds to the z component. The electrons in the double QWR experience three different magnetic fields: an in-plane external magnetic field, effective pseudomagnetic fields arising from Rashba and Dresselhaus spin-orbit couplings. Effective Rashba magnetic field (\vec{B}_R) is directed along the the y axis because it is perpendicular to the electric field and the electron's velocity (Upadhyaya et al., 2008a). The effective Dresselhaus magnetic field (\vec{B}_D) acts along the x direction (Gujarathi et al., 2012). Electrons

with positive (negative) k_x experience $+y$ ($-y$) directed \vec{B}_R and $-x$ ($+x$) directed \vec{B}_D . Therefore the net magnetic field exerted on electrons is the vector sum of the pseudomagnetic fields and the external magnetic field. In the absence of spin-orbit coupling, the spins are parallel to the direction of external magnetic field. In the presence of spin-orbit interaction effects, when $\phi = 0$, for $k_x = -0.69$ (the minimum point of the lowest energy level) electron is under the influence of $-y$ directed \vec{B}_R , $+x$ directed \vec{B}_D and $+x$ directed external magnetic field. So the spins deviate a little from positive x direction to negative y direction as seen in top of the left panel. For the same case but when external magnetic field is applied along the y direction ($\phi = \pi/2$) then the electrons experience $+y$ directed external magnetic field in addition to effective spin-orbit magnetic fields. The external magnetic field is larger than the effective \vec{B}_R and the spins show larger deviations from positive x direction to positive y direction as seen in top of the right panel. Similarly, when $k_x l_0 = 0.69$ (the symmetry point according to $k_x l_0 = 0$ of the minimum point of the lowest energy level) electron is under the influence of $+y$ directed \vec{B}_R , $-x$ directed \vec{B}_D and $+x$ directed external magnetic field for $\phi = 0$. The magnitude of external field is greater than the effective Dresselhaus magnetic field and the spins align the positive $x - y$ plane as shown in bottom of left panel. When $\phi = \pi/2$, the net magnetic field has only x component arises from effective Dresselhaus magnetic field. Both Rashba field and external field are $+y$ directed. Thus the spins are in the negative x and positive y plane displayed in the bottom of right panel. The electrons in the center of the wire will be in closed Landau orbits with no translational velocity. So the states with zero $k_x l_0$ experience no Rashba and Dresselhaus spin-orbit magnetic field because spin-orbit interaction is present only for moving electrons. Therefore the net magnetic field that electrons in the center of wire experience x directed for $\phi = 0$ and y directed for $\phi = \pi/2$ external in-plane magnetic field as shown in the mid of left and right panels of 3.9, respectively. At the edge states the effective pseudomagnetic fields are nonzero. Rashba and Dresselhaus effective magnetic fields have opposite signs at there because the states at the two edges have oppositely directed translational velocities. Spins align parallel to x axis for $\phi = 0$ and parallel to y axis for $\phi = \pi/2$. The z component of magnetization strongly depends on the propagation momenta and the direction of magnetic field.

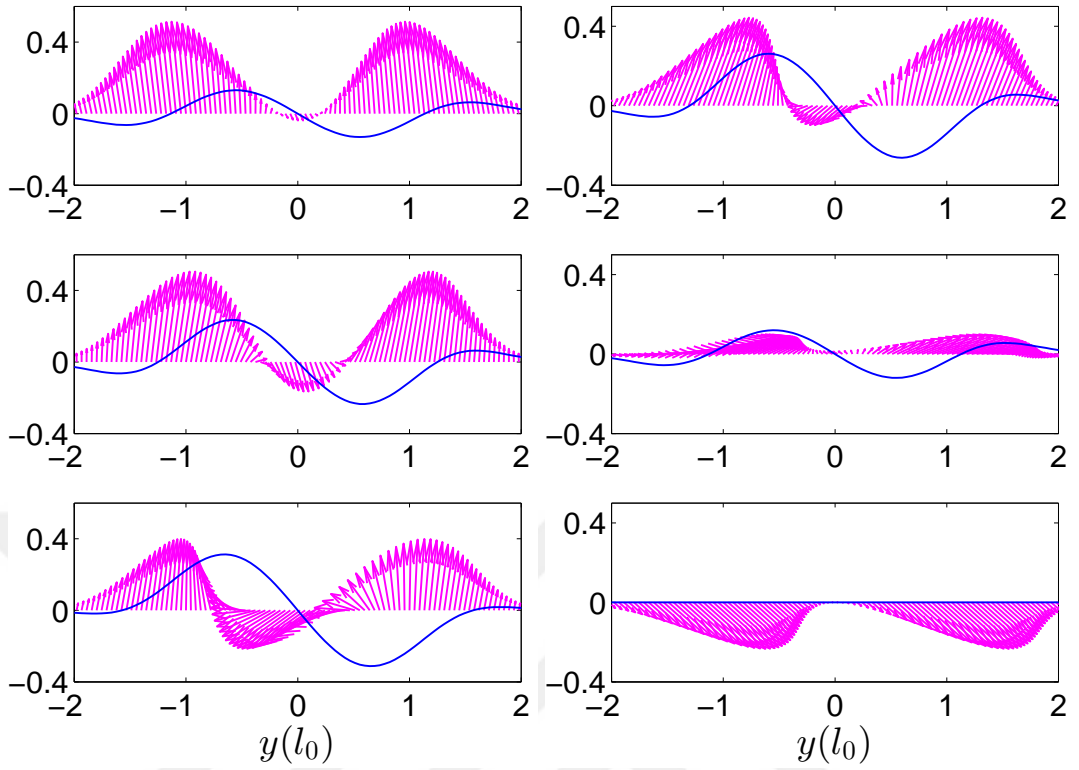


Figure 3.10 Same as Figure 3.9 for the second level of the lowest spin-split subband.

Figure 3.10 presents the spatially spin dependent magnetization for the second subband with the same parameters as in Figure 3.9. The combined effect of the spin-orbit interactions and magnetic field is more pronounced than in the first level of the lowest spin-split subband as seen from the spin textures. Spin distribution of second level exhibits noncollinear distribution compared to the first level and the spin accumulation at the wire edges are larger. In addition, it is clear from the figure that the local z magnetization is greater than lower subband.

In the presence of spin-orbit interaction and magnetic field, the electric field is an effective tool for the studying the properties of spin in semiconductor heterostructures. In these structures, a favorable Stark shift occurs and it can be used to control and manipulate the intensity output of the devices. For this reason, Figure 3.11 is devoted to effect of electric field onto the spin textures. The parameters are chosen same as with Figure 3.6(b) such as $\Delta_R = 0.2$, $\Delta_D = 0.1$ and $B = 1$ T with the angle $\phi = \pi/4$. The structure parameter is set $\tilde{\mu} = 1$ in which the tunneling effects are in action. Left panel

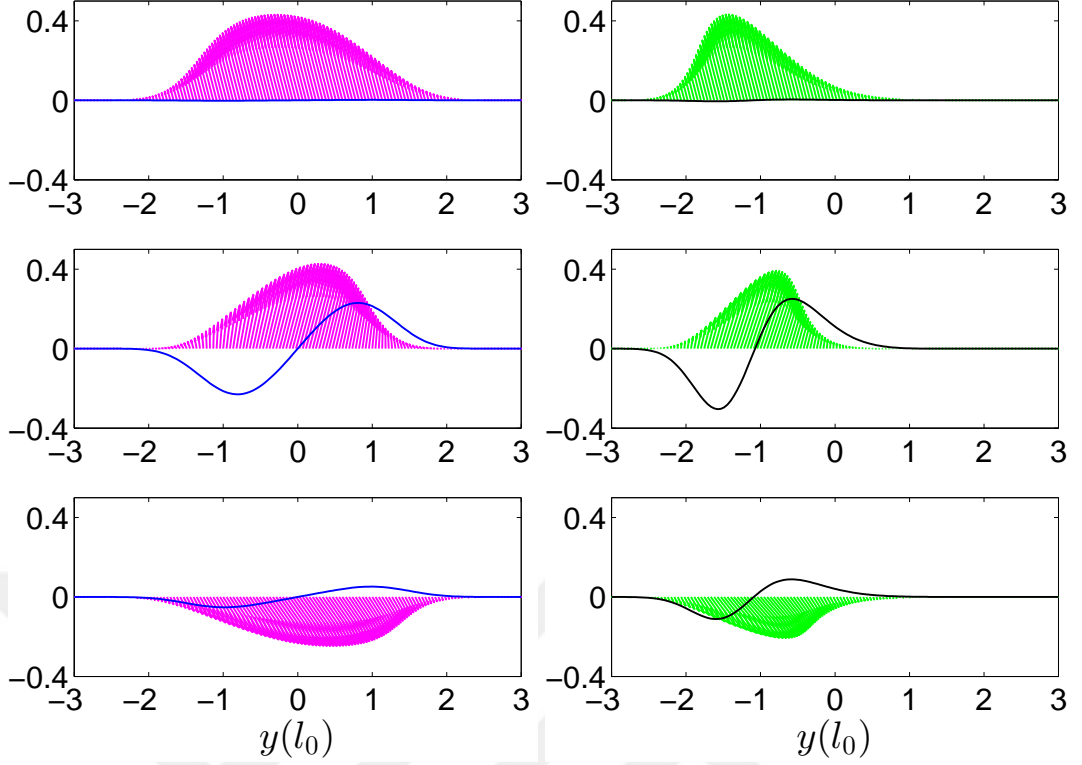


Figure 3.11 Spin textures across the wire subjected to external magnetic field $B = 1$ T with the angle $\phi = \pi/4$ in the presence of spin-orbit coupling characterized by $\Delta_R = 0.2$, $\Delta_D = 0.1$. The left panel corresponds to the zero electric field case, and the right panel presents the effect of electric field $\tilde{F} = 1$. Plots from the top to down correspond to momentum $k_x l_0 = -0.74, 0.0, 0.74$ where arrow length is proportional to spin density. Blue and black solid lines correspond to the z component of magnetization.

corresponds to the absence of electric field and right panel presents the electric field effect ($\tilde{F} = 1$). As described above the electrons with positive (negative) k_x experience $+y$ ($-y$) directed \vec{B}_R and $-x$ ($+x$) directed \vec{B}_D . The spin orientations can be interpreted similarly. Due to the combined effect of pseudomagnetic field and the external in-plane magnetic field, the spins align in the positive x negative y plane for negative $k_x l_0$ values whereas they align in the negative x positive y plane for positive $k_x l_0$ values as presented in top and bottom of the left panel respectively. In the mid of the left panel $k_x l_0 = 0$, the electrons experience equal x and y component of the applied magnetic field. Thus direction of the spins is in the positive $x - y$ plane. Blue solid lines present z component of magnetization which has maximum value at the center of the wire. The right panel of Figure 3.11 depicts the effect of electric field onto the spin distribution. Local spins experience linear displacement depending on the direction of

the electric field which is applied in the growth direction of the system. Similar shift is also observed for the z component of magnetization.

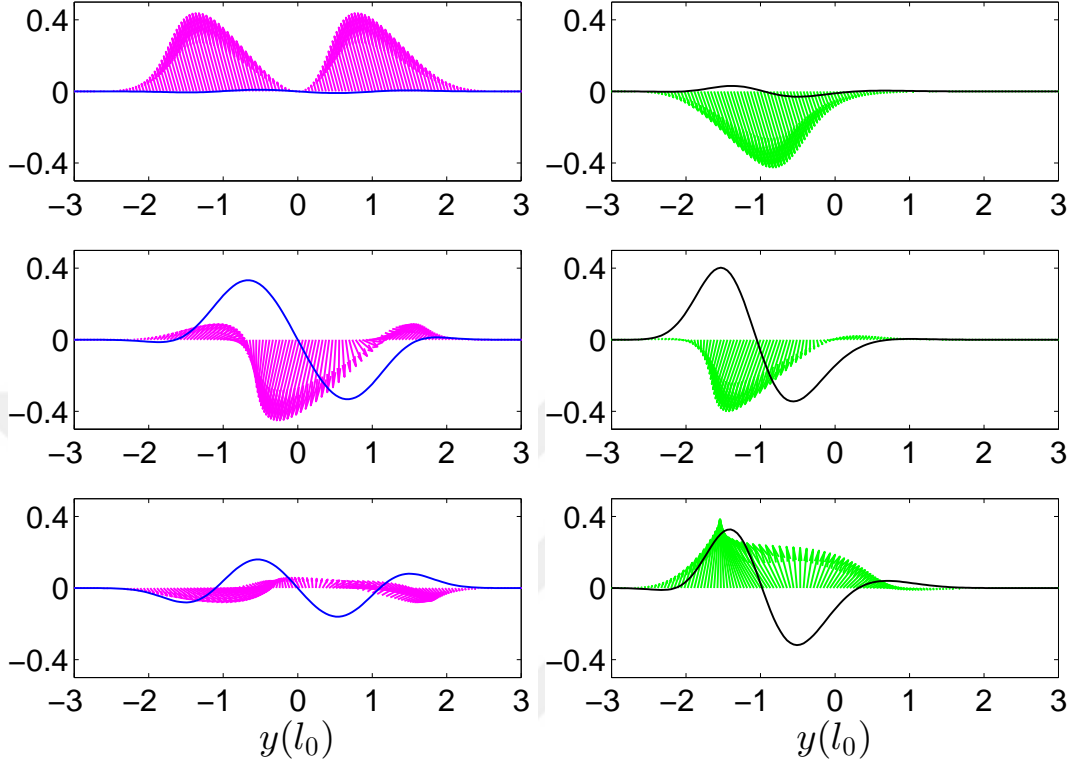


Figure 3.12 Same as Figure 3.11 for the second level of the lowest spin-split subband.

The second level of the lowest spin-split subband is more impressed from the spin-orbit couplings and external magnetic/electric fields than first level of the lowest spin-split subband. The spin texture and local z magnetization of the second level for the same parameters with Figure 3.11 is depicted in Figure 3.12. The spin distribution of first level exhibits linear behaviour as seen in Figure 3.11's left panel whereas it turns to noncollinear distribution for the second level as shown in Figure 3.12's left panel. When an external electric field is applied the spins of second level align in opposite direction with respect to the first level. Also the noncollinear spin distribution in the left panel exhibits nearly linear behaviour and linear displacement in the presence of electric field. Local z magnetization is bigger than the first level both in the absence and presence of electric field.

The combined effect of external and internal agents affects significantly the spin-

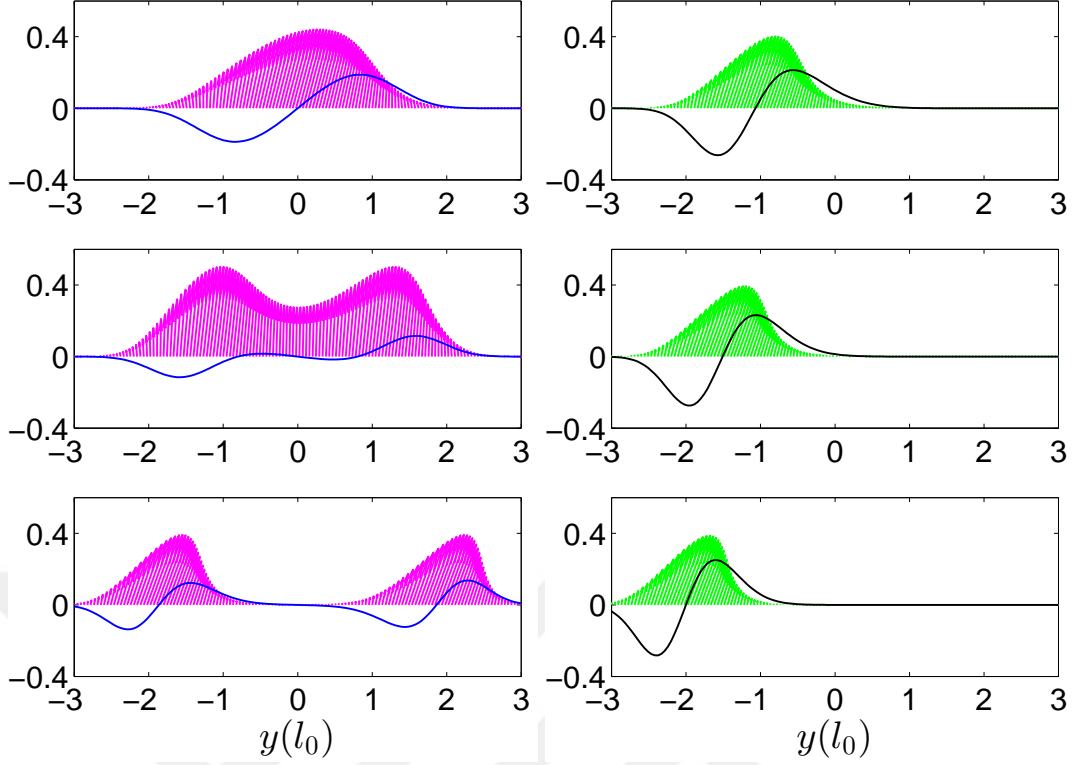


Figure 3.13 Spin textures across the wire corresponding to the parameters: $\Delta_R = 0.2$, $\Delta_D = 0.1$, $B = 1$ T directed with angle $\phi = \pi/4$. Plots from top to bottom correspond to $\tilde{\mu} = 1, 1.5, 2$ when external electric field is zero (left panel) and electric field is not zero $\tilde{F} = 1$ (right panel).

related properties. Figure 3.13 left and right panels depict the spin-textures for three different values of structural parameter $\tilde{\mu} = 1, 1.5, 2$ from top to bottom in the absence and presence of external electric field, respectively. Strong spin-orbit coupling with the value of $\Delta_R = 0.2$, $\Delta_D = 0.1$ is considered under the influence of a constant magnetic field 1 T directed with angle $\phi = \pi/4$. The structural parameter controlling the potential profile leaves its marks on the spin texturing as well as on the energy spectra as seen in Figure 3.13. As shown in the energy spectrums with dashed lines, the value of $\tilde{\mu}$ is increased the coupling between QWRs weakens and the system behaves like as two individual quantum wires. This feature is obviously seen in spin textures. For strong coupling limit $\tilde{\mu} = 1$ (top of left panel) the spin textures orient along the net magnetic field. When the value of $\tilde{\mu}$ is enhanced to 1.5, the energy levels become nearly grouped in pairs, which results in observation of double spin textures in the mid panel. For $\tilde{\mu} = 2$ the system can be considered as two individual QWRs so we observe two individual spin textures for each QWR as seen in bottom of left panel. Also we

observe perceptible change in z component of magnetization with blue lines. The external electric field manifests itself as unique feature in the spin textures especially in weak coupling limits as indicated in right panel of Figure 3.13. It leads to a downward shift in the in-plane spin distributions for all values of $\tilde{\mu}$. The electric field removes the overlap of energy levels of two QWRs and the system behaves as if in the strong coupling limit. That is the why we obtained one spin texture under the influence of electric field even if in the weak coupling limit. Electric field allows for greater spatial selectivity, which is important for local addressing of individual spins. It would thus be highly desirable to control the spins by means of electric fields. In addition, the magnitude of local z magnetization increases when electric field effect is considered.

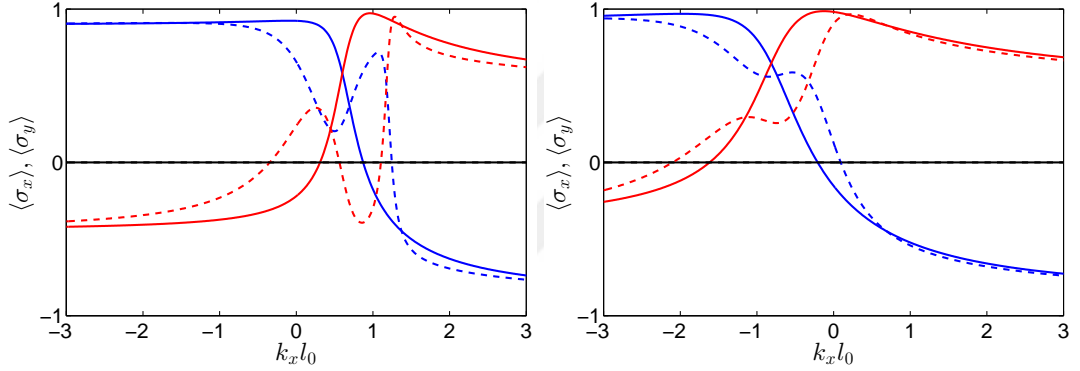


Figure 3.14 The spin projections of eigenstates in the lowest spin-split subbands for the parameters: $\Delta_R = 0.05$, $\Delta_D = 0.2$, $B = 3$ T. Left panel presents $\phi = 0$ case where the right panel shows $\phi = \pi/2$. The solid (dashed) lines show first (second) level of the lowest spin-split subband. Blue lines indicate $\langle\sigma_x\rangle$ whereas red lines represent $\langle\sigma_y\rangle$.

In Figure 3.14, we plot the dependence on k_x of the spin expectation values in the first (solid line) and second (dashed line) level of the lowest spin-split subbands in the presence of both type of spin-orbit couplings ($\Delta_R = 0.05$, $\Delta_D = 0.2$) and external magnetic field (3 T) oriented along the wire axis (left panel) and perpendicular to the wire axis (right panel). Here blue lines indicate $\langle\sigma_x\rangle$ and red lines correspond to $\langle\sigma_y\rangle$. The local z -magnetization in real space $\langle\sigma_z(y)\rangle$ is antisymmetric in y and therefore integrated $\langle\sigma_y\rangle$ is equal to zero. It can be seen that the spins of eigenstates with large absolute value of k_x approach to asymptotic states of $\langle\sigma_x\rangle$ and $\langle\sigma_y\rangle$. For negative large k_x the spinor is nearly described by eigenstates of $\langle\sigma_x\rangle$. Also, it is observed from

the figure that, there exists right (left) moving states for both spin-up and spin-down electrons at any energy. Figure reveals the remarkable change in the spin expectation values $\langle\sigma_x\rangle$ and $\langle\sigma_y\rangle$ for the second spin-split level. When the magnetic field is oriented along the perpendicular axis of the wire the maximum points of spin expectation values shift to negative k_x values as seen in Figure 3.14 right panel. The spin expectation value of second spin-split level exhibits smoother variation.

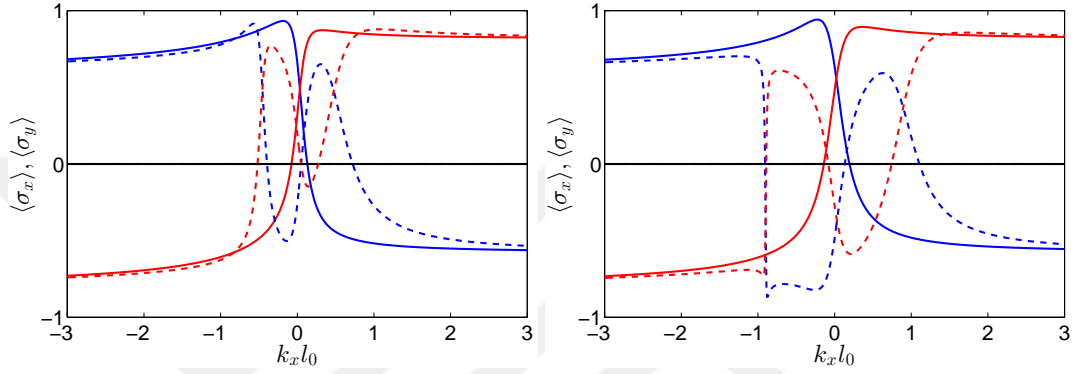


Figure 3.15 The spin projections of eigenstates in the lowest spin-split subbands for the parameters: $\Delta_R = 0.2$, $\Delta_D = 0.1$, $B = 1$ T and $\phi = \pi/4$. Left panel presents $\tilde{F} = 0$ case where the right panel shows $\tilde{F} = 1$. The solid (dashed) lines show first (second) level of the lowest spin-split subband. Blue lines indicate $\langle\sigma_x\rangle$ whereas red lines represent $\langle\sigma_y\rangle$.

The spin expectation values in the first (solid line) and second (dashed line) level of the subbands as a function of k_x are depicted in Figure 3.15 considering strong spin-orbit interaction case and magnetic field with the parameters: $\Delta_R = 0.2$, $\Delta_D = 0.1$, $B = 1$ T and $\phi = \pi/4$. Left panel presents $\tilde{F} = 0$ case where the right panel shows $\tilde{F} = 1$. The effect of electric field is more prominent for the second level of the subband.

3.3.3 Conductance

In recent years, quantum transport phenomena have attracted much attention. The developments in experiment in low-dimensional systems have displayed quantum mechanical nature of transport at low temperatures such as ballistic quantization of conductance. The underlying physical reason of this quantization is the creation of

one-dimensional subband modes due to the electron motion in the two-dimensional electron gases subjected to lateral confinement. In fact that each mode carries the same amount of current (Ferry et al., 2009).

In low-dimensional electron systems, the transmission of electrons can be attributed as the redistribution of incoming electron flux between the discrete energy eigenvalues of the system. Hence the determination of the energy dispersion of the system is extremely important for the calculation of ballistic quantum conductance. Thus the total conductance of the system is completely determined from the energy spectrum and Fermi energy. We assume that two reservoirs are connected to double QWR and the wire is long enough so that is devoid of backscattering process. Conductivity of the system, by neglecting the electron-electron interaction, can be simply calculated using Landauer-Büttiker formalism.

$$G = G_0 \sum_{\alpha\alpha'} T_{\alpha\alpha'} \quad (3.9)$$

where $T_{\alpha\alpha'}$ is the transition probability from $|\alpha\rangle$ state to $|\alpha'\rangle$ state and $G_0 = 2e^2/h$ is the conductance quantization. Following the strategy of Reference. (Pershin et al., 2004), the conductance can be calculated as:

$$G = \frac{e^2}{h} \sum_{n,s} \sum_i \beta_i^{(n,s)} f(E_i^{(n,s)}). \quad (3.10)$$

Here n and s represents the level of state and the level of spin, respectively while $E_i^{(n,s)}$ is the energy of i^{th} extremum point in the related energy subband and $f(E_i^{(n,s)})$ is the Fermi-Dirac distribution. $\beta_i^{(n,s)}$ corresponds -1 for a maximum and $+1$ for a minimum point in the energy subband labeled with n and s as shown in Figure 3.16.

Clearly, the conductance of the system crucially depends on the energy spectrum. Peculiar features in the energy spectra give rise to observe intriguing transport properties through double QWRs. In this part of the paper, our goal is to calculate zero-temperature conductance for different directions of magnetic field such as $\phi = 0, \pi/6, \pi/3, \pi/2$ in the presence of strong spin-orbit couplings $\Delta_R = 0.2$ and $\Delta_D =$

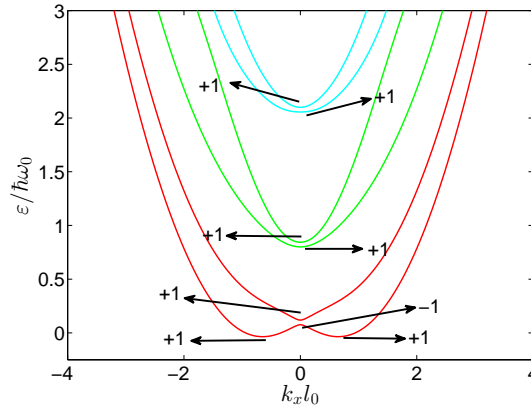


Figure 3.16 Schematic representation of $\beta_i^{(n,s)}$. It is +1 for the minimum point and -1 for the maximum point in the energy subband.

0.1. The strength of magnetic field is set $B = 1$ T and the structure parameter is chosen as $\tilde{\mu} = 1$ in which the tunneling effects are in action. The pink lines present the conductance of the double QWR in the presence of spin-orbit interactions and magnetic field whereas the conductance for the pure case namely no magnetic field and no spin-orbit coupling, is shown with green lines. The energy subband structure is given in Figure 3.6. In the pure case, the energy subbands are two-fold spin-degenerate. As expected, the conductance exhibits an increasing stepwise profile with integer conductance. When the Fermi energy of an electron increases, the conductance increases $2(e2/h)$ instead of $1(e2/h)$ as given in Figure 3.17 with green lines. This physical origin of this quantization can be explained as the additional propagating channels which contribute to conductance are opened in pairs. The competing effect of spin-orbit coupling and external magnetic field gives rise to more complicated energy spectra which breaks down the monotonic stepwise shape of conductance and induces large number of oscillation peaks. The local minimum (subband bottom) and local maximum (subband top) in the subband structures are the reason of anomalous steps in the conductance that appear on the top of the ordinary steps. When the direction of the magnetic field is changed from 0 to $\pi/2$ the minimum and maximum points change so we observe the oscillation peaks at different Fermi energies. Also, the width of the oscillation peaks increase.

The energy spectrum of electrons and conductance critically depends on the

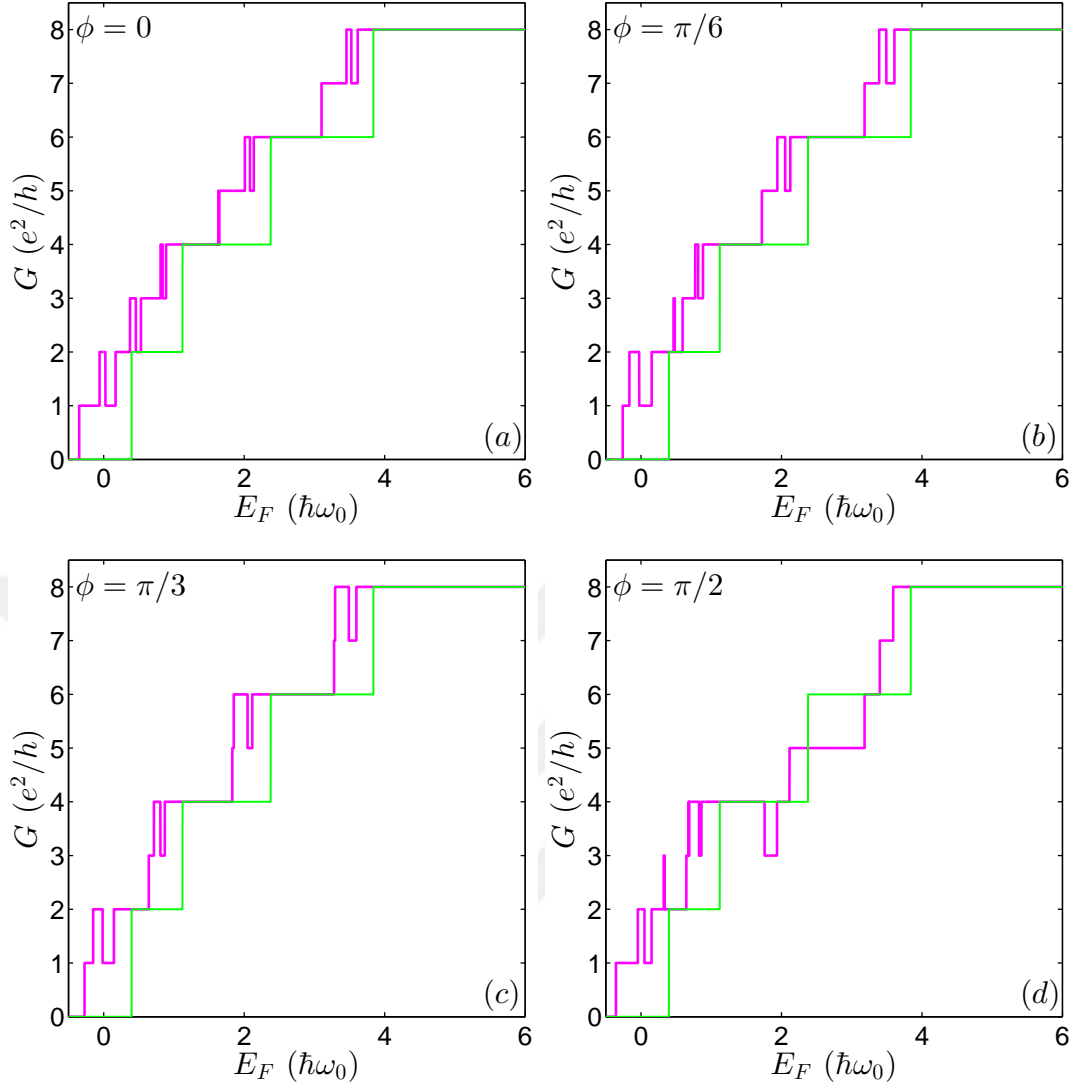


Figure 3.17 The conductance of double quantum wire as a function of Fermi energy in the presence of spin-orbit couplings for different direction of magnetic field with pink lines: a) $\phi = 0$, b) $\phi = \pi/3$, c) $\phi = \pi/3$ and d) $\phi = \pi/2$. The strengths of spin-orbit interaction and magnetic field are set $\Delta_R = 0.2$, $\Delta_D = 0.1$, $B = 1$, respectively. The structural parameter is chosen $\tilde{\mu} = 1$. The green lines correspond the pure case where $\Delta_R = \Delta_D = 0$ and $B = 0$

effective geometry of double QWR as well as the external and internal parameters such as magnetic field and spin-orbit interactions. In order to show the effect of structural parameters, in Figure 3.18 we present the conductance behavior of the subbands of the double QWR comprising of strong spin-orbit interaction $\Delta_R = 0.2$ and $\Delta_D = 0.05$ and magnetic field (1 T) orientated with an angle $\phi = \pi/4$. The energy subband structure of this case is depicted in Figure 3.8. In the pure case, namely no magnetic field and no spin-orbit coupling, the energy subbands are two-fold spin-degenerate for the strong

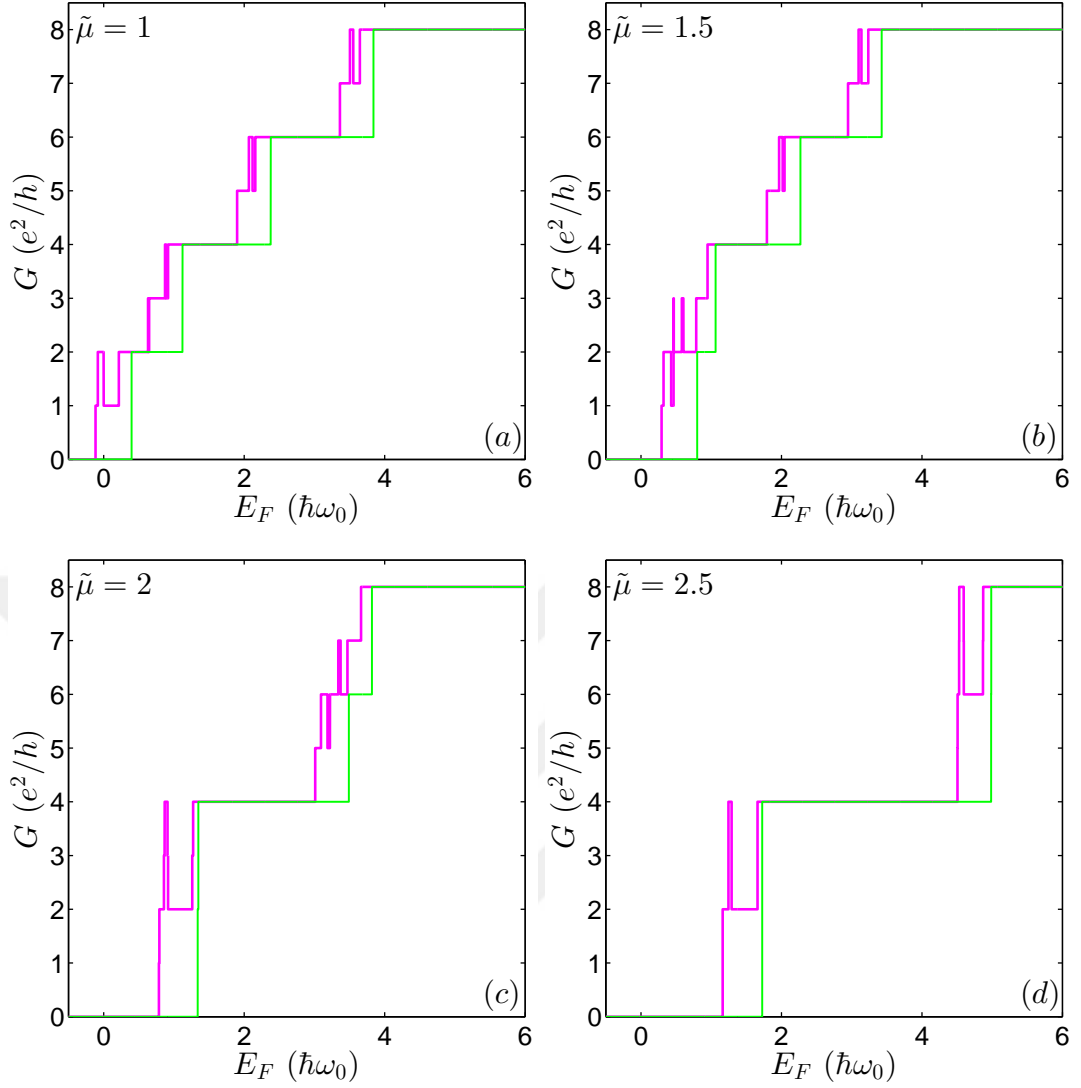


Figure 3.18 Conductance of double quantum wires as a function function of Fermi energy for different values of structural parameter a) $\tilde{\mu} = 1$ b) $\tilde{\mu} = 1.5$ c) $\tilde{\mu} = 2$ and d) $\tilde{\mu} = 2.5$ with pink lines in a constant magnetic field $B = 1$, $\phi = \pi/4$ and in the presence of spin-orbit couplings $\Delta_R = 0.2$, $\Delta_D = 0.05$. The green lines correspond the case pure case where $\Delta_R = \Delta_D = 0$ and $B = 0$.

coupling limit as seen in Figure 3.8(a) and Figure 3.8(b) plotted with dashed lines. When the Fermi energy of an electron increases, the conductance increases $2(e^2/h)$ instead of $1(e^2/h)$ as given in Figure 3.18(a) and Figure 3.18(b) with green lines. The reason of this increment is the additional propagating channels opened in pairs. For $\tilde{\mu} = 2$ (Figure 3.18(c)) the spin-degenerate lowest levels overlap which leads to an increment of conductance in amount of $4(e^2/h)$. In the weak coupling limit, all of spin-degenerate levels are grouped in pairs so conductivity increases monotonically with

$4(e2/h)$ as is evident from the Figure Figure 3.18(d) with red line. For all subfigures it is clear that with the increment of μ the energy gaps raise and this leads to observe wider plateaus of conductance. The conductance under the influence of both magnetic field ($B = 1$ T) with the orientation of $\phi = \pi/4$ and strong spin-orbit coupling limit ($\Delta_R = 0.2$, $\Delta_D = 0.05$) is given with pink lines. The competing effect of spin-orbit coupling and external magnetic field gives rise to local minimum (subband bottom) and local maximum (subband top) in the subband structures. The existence of these minimum and maximum is the reason of anomalous steps in the conductance that appear on the top of the ordinary steps. In this case, the conductance is anymore a stepwise monotonically increasing function, has dips at the extremum points of energy level. The profile of conductance behaves like square-wave oscillations for which, with the increment of μ the width of dips become wider.

The sensitivity of the transport properties of quantum wires to internal and external agents is a key ingredient in the search of new technology. The Stark effect manifested in the shift of electron energy under the action of external electric field is a particular interest. It leaves its marks on the conductance as energy spectra and spin texture as shown in Figure 3.8 and Figure 3.13. Figure 3.19 is devoted to investigate the effect of external electric field on the conductance of double QWR for different structural parameters with same as Figure 3.18. The pink lines denote the absence of electric field case which is also displayed in Figure 3.18 with same color. The light blue lines show the effect of electric field applied the growth direction of wire. It is clear from all subfigures, when the electric field is considered the first steps of conductance shift to lower Fermi energies for all $\tilde{\mu}$ values. Because electric field shifts the energy subbands to lower energies especially for larger value of $\tilde{\mu}$ larger shift occurs as seen in Figure 3.8(c) and Figure 3.8(d). So the first steps of conductance shift to lower Fermi energies in the weak coupling limit. In the strong coupling limit, applying electric field shifts the anomalous steps and leads to smoother behaviour. It gives rise to observe monotonically increasing step wise conductance as depicted in Figure 3.19(a) and Figure 3.19(a). In the weak coupling limit lower spin-split energy levels are nearly degenerate and the energy gaps between upper spin-split energy levels are small so the

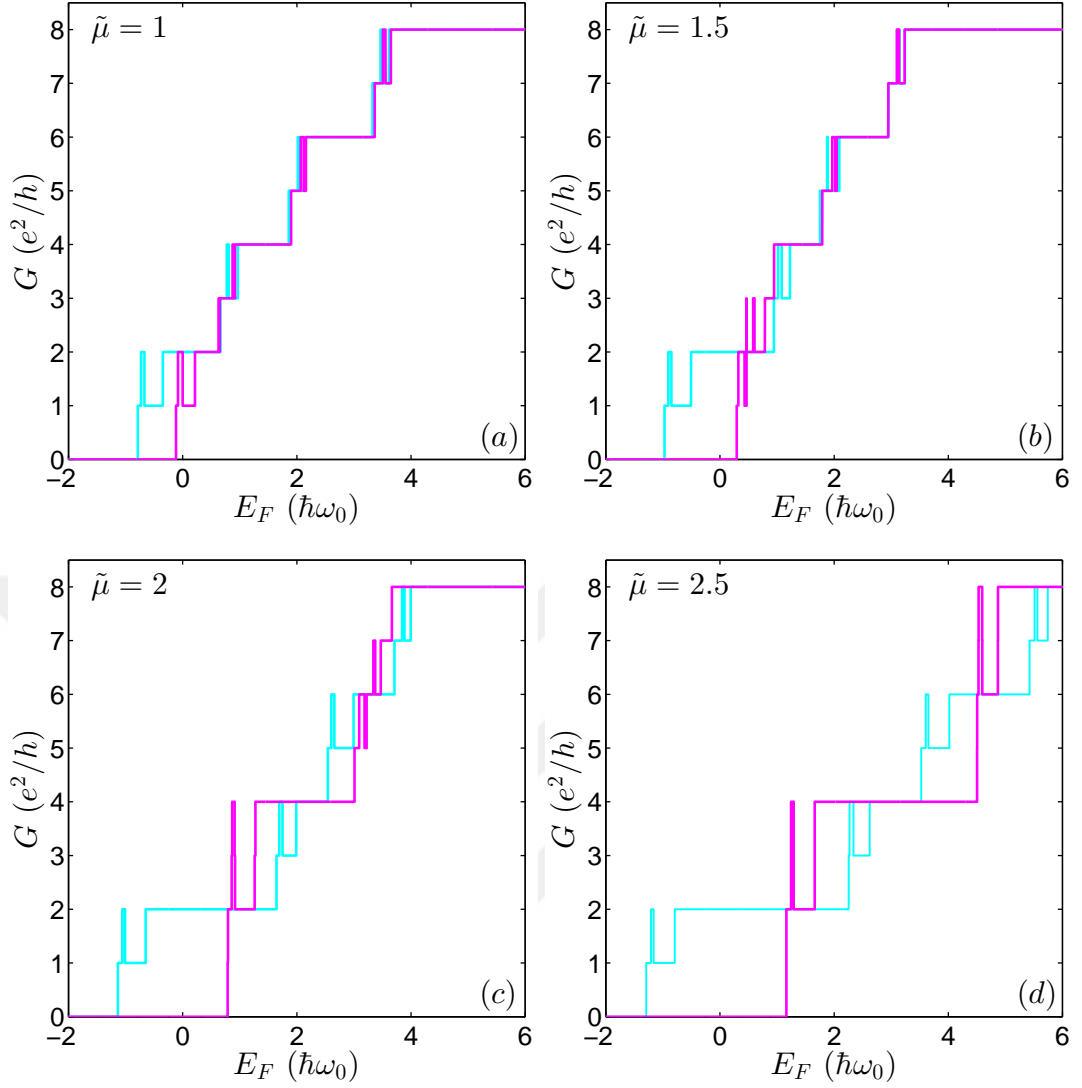


Figure 3.19 Calculated conductance as a function of Fermi energy in the presence of internal and external agents for different values of $\tilde{\mu}$. a) 1, b) 1.5, c) 2 and d) 2.5. The strength of spin-orbit interactions, magnetic field and electric field are: $\Delta_R = 0.2$, $\Delta_D = 0.05$, $B = 1$, $\phi = \pi/4$, $\tilde{F} = 1$.

the width of peaks is narrow. Also the energy gaps between upper and lower subbands are larger so the width of conductance step is large as seen in Figure 3.19(c) with pink lines. Stark effect splits the nearly degenerate levels and induces larger energy gaps. Both width of peaks and width of conductance steps are larger. For $\tilde{\mu} = 2.5$, the energy levels are degenerate so the conductance increases in amount of $(2e^2/h)$. Electric field causes an increment of conductance in amount $(2e^2/h)$ by lifting the degeneracy in the energy levels. Larger energy gaps between subbands induce larger conductance steps.

CHAPTER FOUR

CONDUCTANCE OF PARABOLIC QUANTUM WIRE

In the part of the thesis, we investigate theoretically the conductance for a QWR formed by a parabolic confining potential. The effect of in-plane magnetic field on the electrical conductance of the wire has been analyzed. We take into account the Rashba and Dresselhaus spin-orbit interactions.

4.1 Formalism

We calculate conductance for a quantum wire confined by harmonic potential. For this purpose the QWR structure is divided into three regions as shown in Figure 4.1. The first and third regions are assumed to be identical with same spin-orbit interactions and magnetic fields and which are acting as reservoirs. The middle region differs from the other parts and it is the conductor in which the transmission occurs. We investigate the transmission from region *I* to region *III* for different strengths of Rashba and Dresselhaus spin-orbit interactions and magnetic fields.

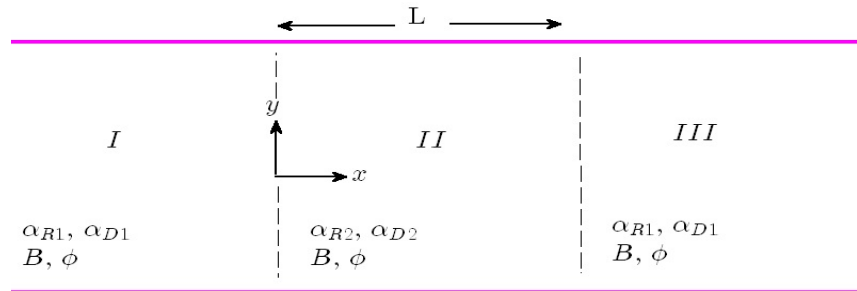


Figure 4.1 The schematic illustration of quantum wire structure used in transport calculations.

The zero-temperature ballistic conductance of a QWR which is connected to two leads is calculated by scattering matrix method. We assume that an electron wave is injected from the left region and transmitted to the third region. In order to calculate scattering matrices, the wave functions at two interfaces of wire-lead connections are

matched. The energies and the wave functions of the Schrödinger equation are obtained numerically by finite elements method (Zienkiewicz et al., 2005). The wave function of an electron can be written as a product of plane-waves propagating along the x -axis and y -dependent spinor part as follows:

$$\Psi(x, y) = \begin{pmatrix} \varphi_{n,\sigma}^{\pm,\uparrow} \\ \varphi_{n,\sigma}^{\pm,\downarrow} \end{pmatrix} e^{ik_{n,\sigma}^{\pm}x}. \quad (4.1)$$

Where the φ is defined as

$$\varphi_{n,\sigma}^{\pm,\uparrow\downarrow} = \varphi(y, k_{n,\sigma}^{\pm}, \uparrow\downarrow). \quad (4.2)$$

Here n is the label of subband index and σ is defined as helicity which stands the lower and upper levels of spin-split subbands. $\sigma = +$ for the lower spin-split energy level whereas the upper level is indicated by $\sigma = -$. The superscript \pm is used to define the coming electron from left (+) and backscattered electron (-) whereas \uparrow, \downarrow is for spin-up and spin-down as usual. Then one can write the wave functions of three regions. The first one is:

$$\Psi^I(x, y) = \begin{pmatrix} \varphi_{n_I, \sigma_I}^{+, \uparrow} \\ \varphi_{n_I, \sigma_I}^{+, \downarrow} \end{pmatrix} e^{ik_{n_I, \sigma_I}^+ x} + \sum_{n'_I} \sum_{\sigma'_I = \pm} r_{n_I, \sigma_I; n'_I, \sigma'_I} \begin{pmatrix} \varphi_{n'_I, \sigma'_I}^{-, \uparrow} \\ \varphi_{n'_I, \sigma'_I}^{-, \downarrow} \end{pmatrix} e^{ik_{n'_I, \sigma'_I}^- x}. \quad (4.3)$$

Here N_I is the total number of states under the Fermi energy, $r_{n_I, \sigma_I; n'_I, \sigma'_I}$ is coefficient of incident modes n_I with helicity σ_I reflecting to mode n'_I with helicity σ'_I . The amplitude of incident electron is assumed as unit. Similarly, the wave function of region II can be written as:

$$\begin{aligned} \Psi^{II}(x, y) &= \sum_{n_{II}} \sum_{\sigma_{II} = \pm} a_{n_I, \sigma_I; n_{II}, \sigma_{II}} \begin{pmatrix} \varphi_{n_{II}, \sigma_{II}}^{+, \uparrow} \\ \varphi_{n_{II}, \sigma_{II}}^{+, \downarrow} \end{pmatrix} e^{ik_{n_{II}, \sigma_{II}}^+ x} \\ &+ \sum_{n'_{II}} \sum_{\sigma'_{II} = \pm} b_{n_I, \sigma_I; n'_{II}, \sigma'_{II}} \begin{pmatrix} \varphi_{n'_{II}, \sigma'_{II}}^{-, \uparrow} \\ \varphi_{n'_{II}, \sigma'_{II}}^{-, \downarrow} \end{pmatrix} e^{ik_{n'_{II}, \sigma'_{II}}^- x}, \end{aligned} \quad (4.4)$$

where $a_{n_I, \sigma_I; n_{II}, \sigma_{II}}$ is transmission coefficient from region I to region II and $b_{n_I, \sigma_I; n'_{II}, \sigma'_{II}}$

is the reflection coefficient. The wave function belonging to third region is

$$\Psi^{III}(x, y) = \sum_{n_{III}}^{N_{III}} \sum_{\sigma_{III}=\pm} t_{n_I, \sigma_I; n_{III}, \sigma_{III}} \begin{pmatrix} \varphi_{n_{III}, \sigma_{III}}^{+, \uparrow} \\ \varphi_{n_{III}, \sigma_{III}}^{+, \downarrow} \end{pmatrix} e^{ik_{n_{III}, \sigma_{III}}^+ x}. \quad (4.5)$$

Here $t_{n_I, \sigma_I; n_{III}, \sigma_{III}}$ is the transmission coefficient of an electron from region I with mode n_I, σ_I to region III with with mode n_{III}, σ_{III} .

The wave functions satisfy two conditions at the interfaces $x = 0$ and $x = L$: i) the wave functions have continuity at two interfaces, ii) due to the presence of spin-orbit couplings, the continuity of their derivative is not valid, so the wave functions ensure the current conservation (Moroz & Barnes, 1999; Wang, 2004). At this point, it is useful to obtain velocity operator.

$$v_x = \frac{\partial H}{\partial p_x} = \frac{p_y}{m^*} \sigma_0 - \frac{\alpha_R}{\hbar} \sigma_y + \frac{\alpha_D}{\hbar} \sigma_x. \quad (4.6)$$

The continuity of wave functions at the interface $x = 0$ gives

$$\Psi^I(x, y)|_{(x=0)} = \Psi^{II}(x, y)|_{(x=0)}, \quad (4.7)$$

$$\begin{aligned} & \begin{pmatrix} \varphi_{n_I, \sigma_I}^{+, \uparrow} \\ \varphi_{n_I, \sigma_I}^{+, \downarrow} \end{pmatrix} + \sum_{n'_I} \sum_{\sigma'_I} \begin{pmatrix} \varphi_{n'_I, \sigma'_I}^{-, \uparrow} \\ \varphi_{n'_I, \sigma'_I}^{-, \downarrow} \end{pmatrix} r_{n_I, \sigma_I; n'_I, \sigma'_I} \\ &= \sum_{n_{II}} \sum_{\sigma_{II}} \begin{pmatrix} \varphi_{n_{II}, \sigma_{II}}^{+, \uparrow} \\ \varphi_{n_{II}, \sigma_{II}}^{+, \downarrow} \end{pmatrix} a_{n_I, \sigma_I; n_{II}, \sigma_{II}} + \sum_{n'_{II}} \sum_{\sigma'_{II}} \begin{pmatrix} \varphi_{n'_{II}, \sigma'_{II}}^{-, \uparrow} \\ \varphi_{n'_{II}, \sigma'_{II}}^{-, \downarrow} \end{pmatrix} b_{n_I, \sigma_I; n'_{II}, \sigma'_{II}}. \end{aligned} \quad (4.8)$$

The current conservation at $x = 0$ is (?)

$$v_x^I \Psi^I(x, y)|_{(x=0)} = v_x^{II} \Psi^{II}(x, y)|_{(x=0)}. \quad (4.9)$$

$$\begin{aligned}
& \begin{pmatrix} k_{n_I, \sigma_I}^+ & C_I \\ C_I^* & k_{n_I, \sigma_I}^+ \end{pmatrix} \begin{pmatrix} \varphi_{n_I, \sigma_I}^{+, \uparrow} \\ \varphi_{n_I, \sigma_I}^{+, \downarrow} \end{pmatrix} \\
& + \sum_{n'_I} \sum_{\sigma'_I} \begin{pmatrix} k_{n'_I, \sigma'_I}^- & C_I \\ C_I^* & k_{n'_I, \sigma'_I}^- \end{pmatrix} \begin{pmatrix} \varphi_{n'_I, \sigma'_I}^{-, \uparrow} \\ \varphi_{n'_I, \sigma'_I}^{-, \downarrow} \end{pmatrix} r_{n_I, \sigma_I; n'_I, \sigma'_I} \\
& = \sum_{n_{II}} \sum_{\sigma_{II}} \begin{pmatrix} k_{n_{II}, \sigma_{II}}^+ & C_{II} \\ C_{II}^* & k_{n_{II}, \sigma_{II}}^+ \end{pmatrix} \begin{pmatrix} \varphi_{n_{II}, \sigma_{II}}^{+, \uparrow} \\ \varphi_{n_{II}, \sigma_{II}}^{+, \downarrow} \end{pmatrix} a_{n_I, \sigma_I; n_{II}, \sigma_{II}} \\
& + \sum_{n'_{II}} \sum_{\sigma'_{II}} \begin{pmatrix} k_{n'_{II}, \sigma'_{II}}^- & C_{II} \\ C_{II}^* & k_{n'_{II}, \sigma'_{II}}^- \end{pmatrix} \begin{pmatrix} \varphi_{n'_{II}, \sigma'_{II}}^{-, \uparrow} \\ \varphi_{n'_{II}, \sigma'_{II}}^{-, \downarrow} \end{pmatrix} b_{n_I, \sigma_I; n'_{II}, \sigma'_{II}}. \tag{4.10}
\end{aligned}$$

Here C indicates the spin-orbit coupling constants in the velocity operator such as $C_n = \frac{m^*}{\hbar} (i\alpha_{R_n} + \alpha_{D_n})$ with $n = I, II, III$. (C_n^* is the complex conjugate.)

The first boundary condition at $x = L$ gives

$$\Psi^{II}(x, y)|_{(x=L)} = \Psi^{III}(x, y)|_{(x=L)}, \tag{4.11}$$

$$\begin{aligned}
& \sum_{n_{II}} \sum_{\sigma_{II}} \begin{pmatrix} \varphi_{n_{II}, \sigma_{II}}^{+, \uparrow} \\ \varphi_{n_{II}, \sigma_{II}}^{+, \downarrow} \end{pmatrix} e^{ik_{n_{II}, \sigma_{II}}^+ L} a_{n_I, \sigma_I; n_{II}, \sigma_{II}} + \sum_{n'_{II}} \sum_{\sigma'_{II}} \begin{pmatrix} \varphi_{n'_{II}, \sigma'_{II}}^{-, \uparrow} \\ \varphi_{n'_{II}, \sigma'_{II}}^{-, \downarrow} \end{pmatrix} e^{ik_{n'_{II}, \sigma'_{II}}^- L} b_{n_I, \sigma_I; n'_{II}, \sigma'_{II}} \\
& = \sum_{n_{III}} \sum_{\sigma_{III}} \begin{pmatrix} \varphi_{n_{III}, \sigma_{III}}^{+, \uparrow} \\ \varphi_{n_{III}, \sigma_{III}}^{+, \downarrow} \end{pmatrix} e^{ik_{n_{III}, \sigma_{III}}^+ L} t_{n_I, \sigma_I; n_{III}, \sigma_{III}} \tag{4.12}
\end{aligned}$$

The current conservation at $x = L$ implies

$$v_x^{II} \Psi^{II}(x, y)|_{(x=L)} = v_x^{III} \Psi^{III}(x, y)|_{(x=L)}. \tag{4.13}$$

$$\begin{aligned}
& \sum_{n_{II}} \sum_{\sigma_{II}} \begin{pmatrix} k_{n_{II},\sigma_{II}}^+ & C_{II} \\ C_{II}^* & k_{n_{II},\sigma_{II}}^+ \end{pmatrix} \begin{pmatrix} \varphi_{n_{II},\sigma_{II}}^{+,\uparrow} \\ \varphi_{n_{II},\sigma_{II}}^{+,\downarrow} \end{pmatrix} e^{ik_{n_{II},\sigma_{II}}^+ L} a_{n_I,\sigma_I;n_{II},\sigma_{II}} \\
& + \sum_{n'_{II}} \sum_{\sigma'_{II}} \begin{pmatrix} k_{n'_{II},\sigma'_{II}}^- & C_{II} \\ C_{II}^* & k_{n'_{II},\sigma'_{II}}^- \end{pmatrix} \begin{pmatrix} \varphi_{n'_{II},\sigma'_{II}}^{-,\uparrow} \\ \varphi_{n'_{II},\sigma'_{II}}^{-,\downarrow} \end{pmatrix} e^{ik_{n'_{II},\sigma'_{II}}^- L} b_{n_I,\sigma_I;n'_{II},\sigma'_{II}} \\
& = \sum_{n_{III}} \sum_{\sigma_{III}} \begin{pmatrix} k_{n_{III},\sigma_{III}}^+ & C_{III} \\ C_{III}^* & k_{n_{III},\sigma_{III}}^+ \end{pmatrix} \begin{pmatrix} \varphi_{n_{III},\sigma_{III}}^{+,\uparrow} \\ \varphi_{n_{III},\sigma_{III}}^{+,\downarrow} \end{pmatrix} e^{ik_{n_{III},\sigma_{III}}^+ L} t_{n_I,\sigma_I;n_{III},\sigma_{III}} \tag{4.14}
\end{aligned}$$

Then after, the Equations 4.8 and 4.10 obtained from the first interface $x = 0$ are multiplied by $(\varphi_{n_I,\sigma_I}^{+,\uparrow}, \varphi_{n_I,\sigma_I}^{+,\downarrow})^*$ from left and integrated over the y . In a similar manner the Eqs. 4.12 and 4.14 arise from $x = L$ interface are multiplied by $(\varphi_{n_{II},\sigma_{II}}^{+,\uparrow}, \varphi_{n_{II},\sigma_{II}}^{+,\downarrow})^*$ from left and integrated over the y . For the sake of simplicity, we have defined some abbreviations for the expressions:

$$\begin{aligned}
\mathbf{A}_{2N_I \times 2N_I}^{I+} &= \int dy ((\varphi_{n_I,\sigma_I}^{+,\uparrow})^* \varphi_{n_I,\sigma_I}^{+,\uparrow} + (\varphi_{n_I,\sigma_I}^{+,\downarrow})^* \varphi_{n_I,\sigma_I}^{+,\downarrow}) \\
\mathbf{A}_{2N_I \times 2N_I}^{I-} &= \int dy ((\varphi_{n_I,\sigma_I}^{+,\uparrow})^* \varphi_{n'_{II},\sigma'_{II}}^{-,\uparrow} + (\varphi_{n_I,\sigma_I}^{+,\downarrow})^* \varphi_{n'_{II},\sigma'_{II}}^{-,\downarrow}) \\
\mathbf{A}_{2N_I \times 2N_{II}}^{II+} &= \int dy ((\varphi_{n_I,\sigma_I}^{+,\uparrow})^* \varphi_{n_{II},\sigma_{II}}^{+,\uparrow} + (\varphi_{n_I,\sigma_I}^{+,\downarrow})^* \varphi_{n_{II},\sigma_{II}}^{+,\downarrow}) \\
\mathbf{A}_{2N_I \times 2N_{II}}^{II-} &= \int dy ((\varphi_{n_I,\sigma_I}^{+,\uparrow})^* \varphi_{n'_{II},\sigma'_{II}}^{-,\uparrow} + (\varphi_{n_I,\sigma_I}^{+,\downarrow})^* \varphi_{n'_{II},\sigma'_{II}}^{-,\downarrow}) \\
\mathbf{B}_{2N_I \times 2N_I}^{I+} &= \int dy (k_{n_I,\sigma_I}^+ ((\varphi_{n_I,\sigma_I}^{+,\uparrow})^* \varphi_{n_I,\sigma_I}^{+,\uparrow} + (\varphi_{n_I,\sigma_I}^{+,\downarrow})^* \varphi_{n_I,\sigma_I}^{+,\downarrow}) \\
&\quad C_I ((\varphi_{n_I,\sigma_I}^{+,\uparrow})^* \varphi_{n_I,\sigma_I}^{+,\uparrow} + (\varphi_{n_I,\sigma_I}^{+,\downarrow})^* \varphi_{n_I,\sigma_I}^{+,\downarrow})) \\
\mathbf{B}_{2N_I \times 2N_I}^{I-} &= \int dy (k_{n'_{II},\sigma'_{II}}^- ((\varphi_{n_I,\sigma_I}^{+,\uparrow})^* \varphi_{n'_{II},\sigma'_{II}}^{-,\uparrow} + (\varphi_{n_I,\sigma_I}^{+,\downarrow})^* \varphi_{n'_{II},\sigma'_{II}}^{-,\downarrow}) \\
&\quad C_I^* ((\varphi_{n_I,\sigma_I}^{+,\uparrow})^* \varphi_{n'_{II},\sigma'_{II}}^{-,\uparrow} + (\varphi_{n_I,\sigma_I}^{+,\downarrow})^* \varphi_{n'_{II},\sigma'_{II}}^{-,\downarrow})) \\
\mathbf{B}_{2N_I \times 2N_{II}}^{II+} &= \int dy (k_{n_{II},\sigma_{II}}^+ ((\varphi_{n_I,\sigma_I}^{+,\uparrow})^* \varphi_{n_{II},\sigma_{II}}^{+,\uparrow} + (\varphi_{n_I,\sigma_I}^{+,\downarrow})^* \varphi_{n_{II},\sigma_{II}}^{+,\downarrow}) \\
&\quad C_{II} ((\varphi_{n_I,\sigma_I}^{+,\uparrow})^* \varphi_{n_{II},\sigma_{II}}^{+,\uparrow} + (\varphi_{n_I,\sigma_I}^{+,\downarrow})^* \varphi_{n_{II},\sigma_{II}}^{+,\downarrow}))
\end{aligned}$$

$$\begin{aligned}
\mathbf{B}_{2N_I \times 2N_{II}}^{II-} &= \int dy (k_{n_{II}, \sigma_{II}}^- ((\varphi_{n_I, \sigma_I}^{+\uparrow})^* \varphi_{n'_{II}, \sigma'_{II}}^{-\uparrow} + (\varphi_{n_I, \sigma_I}^{+\downarrow})^* \varphi_{n'_{II}, \sigma'_{II}}^{-\downarrow})) \\
&\quad C_{II}^* ((\varphi_{n_I, \sigma_I}^{+\uparrow})^* \varphi_{n'_{II}, \sigma'_{II}}^{-\uparrow} + (\varphi_{n_I, \sigma_I}^{+\downarrow})^* \varphi_{n'_{II}, \sigma'_{II}}^{-\downarrow}) \\
\mathbf{C}_{2N_{II} \times 2N_{II}}^{II+} &= \int dy ((\varphi_{n_{II}, \sigma_{II}}^{+\uparrow})^* \varphi_{n_{II}, \sigma_{II}}^{+\uparrow} + (\varphi_{n_{II}, \sigma_{II}}^{+\downarrow})^* \varphi_{n_{II}, \sigma_{II}}^{+\downarrow}) \\
\mathbf{C}_{2N_{II} \times 2N_{II}}^{II-} &= \int dy ((\varphi_{n_{II}, \sigma_{II}}^{+\uparrow})^* \varphi_{n'_{II}, \sigma'_{II}}^{-\uparrow} + (\varphi_{n_{II}, \sigma_{II}}^{+\downarrow})^* \varphi_{n'_{II}, \sigma'_{II}}^{-\downarrow}) \\
\mathbf{C}_{2N_{II} \times 2N_{III}}^{III+} &= \int dy ((\varphi_{n_{II}, \sigma_{II}}^{+\uparrow})^* \varphi_{n_{III}, \sigma_{III}}^{+\uparrow} + (\varphi_{n_{II}, \sigma_{II}}^{+\downarrow})^* \varphi_{n_{III}, \sigma_{III}}^{+\downarrow}) \\
\mathbf{D}_{2N_{II} \times 2N_{II}}^{II+} &= \int dy (k_{n_{II}, \sigma_{II}}^+ ((\varphi_{n_{II}, \sigma_{II}}^{+\uparrow})^* \varphi_{n_{II}, \sigma_{II}}^{+\uparrow} + (\varphi_{n_{II}, \sigma_{II}}^{+\downarrow})^* \varphi_{n_{II}, \sigma_{II}}^{+\downarrow})) \\
&\quad C_{II} ((\varphi_{n_{II}, \sigma_{II}}^{+\uparrow})^* \varphi_{n_{II}, \sigma_{II}}^{+\uparrow} + (\varphi_{n_{II}, \sigma_{II}}^{+\downarrow})^* \varphi_{n_{II}, \sigma_{II}}^{+\downarrow}) \\
\mathbf{D}_{2N_{II} \times 2N_{II}}^{II-} &= \int dy (k_{n_{II}, \sigma_{II}}^+ ((\varphi_{n_{II}, \sigma_{II}}^{+\uparrow})^* \varphi_{n'_{II}, \sigma'_{II}}^{+\uparrow} + (\varphi_{n_{II}, \sigma_{II}}^{+\downarrow})^* \varphi_{n'_{II}, \sigma'_{II}}^{+\downarrow})) \\
&\quad C_{II} ((\varphi_{n_{II}, \sigma_{II}}^{+\uparrow})^* \varphi_{n'_{II}, \sigma'_{II}}^{+\uparrow} + (\varphi_{n_{II}, \sigma_{II}}^{+\downarrow})^* \varphi_{n'_{II}, \sigma'_{II}}^{+\downarrow}) \\
\mathbf{D}_{2N_{II} \times 2N_{III}}^{III+} &= \int dy (k_{n_{II}, \sigma_{II}}^+ ((\varphi_{n_{II}, \sigma_{II}}^{+\uparrow})^* \varphi_{n_{III}, \sigma_{III}}^{+\uparrow} + (\varphi_{n_{II}, \sigma_{II}}^{+\downarrow})^* \varphi_{n_{III}, \sigma_{III}}^{+\downarrow})) \\
&\quad C_{III} ((\varphi_{n_{II}, \sigma_{II}}^{+\uparrow})^* \varphi_{n_{III}, \sigma_{III}}^{+\uparrow} + (\varphi_{n_{II}, \sigma_{II}}^{+\downarrow})^* \varphi_{n_{III}, \sigma_{III}}^{+\downarrow})
\end{aligned} \tag{4.15}$$

Here the dimension of the matrices are $2N \times 2N$ if the number of subband N under the Fermi function includes both $+$ and $-$ spin-split levels. If N includes only $+$ level than the dimensions of the matrices are $(2N - 1) \times (2N - 1)$. The reflection matrix r is given as:

$$\mathbf{r} = \begin{pmatrix} r_{0,+;0,+} & r_{0,-;0,+} & r_{1,+;0,+} & \cdot & \cdot & \cdot & r_{N_I,+;0+} & r_{N_I,-;0+} \\ r_{0,+;0,-} & r_{0,-;0,-} & r_{1,+;0,-} & \cdot & \cdot & \cdot & r_{N_I,+;0-} & r_{N_I,-;0-} \\ r_{0,+;1,+} & r_{0,-;1,+} & r_{1,+;1,+} & \cdot & \cdot & \cdot & r_{N_I,+;1+} & r_{N_I,-;1+} \\ \cdot & \cdot & \cdot & \cdot & \cdot & \cdot & \cdot & \cdot \\ \cdot & \cdot & \cdot & \cdot & \cdot & \cdot & \cdot & \cdot \\ \cdot & \cdot & \cdot & \cdot & \cdot & \cdot & \cdot & \cdot \\ r_{0,+;N_I,+} & r_{0,-;N_I,+} & r_{1,+;N_I,+} & \cdot & \cdot & \cdot & r_{N_I,+;N_I+} & r_{N_I,-;N_I+} \\ r_{0,+;N_I,-} & r_{0,-;N_I,-} & r_{1,+;N_I,-} & \cdot & \cdot & \cdot & r_{N_I,+;N_I,-} & r_{N_I,-;N_I,-} \end{pmatrix}. \tag{4.16}$$

Similarly, the transmission amplitudes (matrix a) and refracting amplitudes (matrix b) for region II can be written as follows:

$$\mathbf{a} = \begin{pmatrix} a_{0,+;0,+} & a_{0,-;0,+} & a_{1,+;0,+} & \cdot & \cdot & \cdot & a_{N_I,+;0+} & a_{N_I,-;0+} \\ a_{0,+;0,-} & a_{0,-;0,-} & a_{1,+;0,-} & \cdot & \cdot & \cdot & a_{N_I,+;0-} & a_{N_I,-;0-} \\ a_{0,+;1,+} & a_{0,-;1,+} & a_{1,+;1,+} & \cdot & \cdot & \cdot & a_{N_I,+;1+} & a_{N_I,-;1+} \\ \cdot & \cdot & \cdot & \cdot & \cdot & \cdot & \cdot & \cdot \\ \cdot & \cdot & \cdot & \cdot & \cdot & \cdot & \cdot & \cdot \\ \cdot & \cdot & \cdot & \cdot & \cdot & \cdot & \cdot & \cdot \\ a_{0,+;N_{II},+} & a_{0,-;N_{II},+} & a_{1,+;N_{II},+} & \cdot & \cdot & \cdot & a_{N_{II},+;N_{II}+} & a_{N_{II},-;N_{II}+} \\ a_{0,+;N_{II},-} & a_{0,-;N_{II},-} & a_{1,+;N_{II},-} & \cdot & \cdot & \cdot & a_{N_{II},+;N_{II},-} & a_{N_{II},-;N_{II},-} \end{pmatrix} \quad (4.17)$$

$$\mathbf{b} = \begin{pmatrix} b_{0,+;0,+} & b_{0,-;0,+} & b_{1,+;0,+} & \cdot & \cdot & \cdot & b_{N_I,+;0+} & b_{N_I,-;0+} \\ b_{0,+;0,-} & b_{0,-;0,-} & b_{1,+;0,-} & \cdot & \cdot & \cdot & b_{N_I,+;0-} & b_{N_I,-;0-} \\ b_{0,+;1,+} & b_{0,-;1,+} & b_{1,+;1,+} & \cdot & \cdot & \cdot & b_{N_I,+;1+} & b_{N_I,-;1+} \\ \cdot & \cdot & \cdot & \cdot & \cdot & \cdot & \cdot & \cdot \\ \cdot & \cdot & \cdot & \cdot & \cdot & \cdot & \cdot & \cdot \\ \cdot & \cdot & \cdot & \cdot & \cdot & \cdot & \cdot & \cdot \\ b_{0,+;N_{II},+} & b_{0,-;N_{II},+} & b_{1,+;N_{II},+} & \cdot & \cdot & \cdot & b_{N_{II},+;N_{II}+} & b_{N_{II},-;N_{II}+} \\ b_{0,+;N_{II},-} & b_{0,-;N_{II},-} & b_{1,+;N_{II},-} & \cdot & \cdot & \cdot & b_{N_{II},+;N_{II},-} & b_{N_{II},-;N_{II},-} \end{pmatrix} \quad (4.18)$$

The transmission matrix of the system becomes to be:

$$\mathbf{t} = \begin{pmatrix} t_{0,+;0,+} & t_{0,-;0,+} & t_{1,+;0,+} & \cdot & \cdot & \cdot & t_{N_I,+;0+} & t_{N_I,-;0+} \\ t_{0,+;0,-} & t_{0,-;0,-} & t_{1,+;0,-} & \cdot & \cdot & \cdot & t_{N_I,+;0-} & t_{N_I,-;0-} \\ t_{0,+;1,+} & t_{0,-;1,+} & t_{1,+;1,+} & \cdot & \cdot & \cdot & t_{N_I,+;1+} & t_{N_I,-;1+} \\ \cdot & \cdot & \cdot & \cdot & \cdot & \cdot & \cdot & \cdot \\ \cdot & \cdot & \cdot & \cdot & \cdot & \cdot & \cdot & \cdot \\ \cdot & \cdot & \cdot & \cdot & \cdot & \cdot & \cdot & \cdot \\ t_{0,+;N_{II},+} & t_{0,-;N_{II},+} & t_{1,+;N_{II},+} & \cdot & \cdot & \cdot & t_{N_{II},+;N_{II}+} & b_{N_{II},-;N_{II}+} \\ t_{0,+;N_{II},-} & t_{0,-;N_{II},-} & t_{1,+;N_{II},-} & \cdot & \cdot & \cdot & t_{N_{II},+;N_{II},-} & t_{N_{II},-;N_{II},-} \end{pmatrix} \quad (4.19)$$

The continuity of the wave functions and the current conservation at the two

interfaces can be rewritten in with definitions accordingly,

$$\begin{aligned}
(\mathbf{A}^{I+})_{2N_I \times 2N_I} + (\mathbf{A}^{I-})_{2N_I \times 2N_I}(\mathbf{r})_{2N_I \times 2N_I} &= (\mathbf{A}^{II+})_{2N_I \times 2N_{II}}(\mathbf{a})_{2N_{II} \times 2N_I} + (\mathbf{A}^{II-})_{2N_I \times 2N_{II}}(\mathbf{b})_{2N_{II} \times 2N_I} \\
(\mathbf{B}^{I+})_{2N_I \times 2N_I} + (\mathbf{B}^{I-})_{2N_I \times 2N_I}(\mathbf{r})_{2N_I \times 2N_I} &= (\mathbf{B}^{II+})_{2N_I \times 2N_{II}}(\mathbf{a})_{2N_{II} \times 2N_I} + (\mathbf{B}^{II-})_{2N_I \times 2N_{II}}(\mathbf{b})_{2N_{II} \times 2N_I} \\
(\mathbf{C}^{II+})_{2N_{II} \times 2N_{II}}(\mathbf{a})_{2N_{II} \times 2N_I} + (\mathbf{C}^{II-})_{2N_{II} \times 2N_{II}}(\mathbf{b})_{2N_{II} \times 2N_I} &= (\mathbf{C}^{III+})_{2N_{II} \times 2N_{III}}(\mathbf{t})_{2N_{III} \times 2N_I} \\
(\mathbf{D}^{II+})_{2N_{II} \times 2N_{II}}(\mathbf{a})_{2N_{II} \times 2N_I} + (\mathbf{D}^{II-})_{2N_{II} \times 2N_{II}}(\mathbf{b})_{2N_{II} \times 2N_I} &= (\mathbf{D}^{III+})_{2N_{II} \times 2N_{III}}(\mathbf{t})_{2N_{III} \times 2N_I}. \quad (4.20)
\end{aligned}$$

From Eqs. 4.20, with some mathematical algebra it is possible to obtain unknown matrices \mathbf{r} , \mathbf{a} , \mathbf{b} and \mathbf{t} . For the simplicity of illustration, we do not write the dimensions of matrices.

$$\begin{aligned}
\mathbf{a} &= (\mathbf{C}^{II+})^{-1}(\mathbf{C}^{III+})(\mathbf{t}) - (\mathbf{C}^{II+})^{-1}(\mathbf{C}^{II-})(\mathbf{b}) \\
\mathbf{a} &= (\mathbf{D}^{II+})^{-1}(\mathbf{D}^{III+})(\mathbf{t}) - (\mathbf{D}^{II+})^{-1}(\mathbf{D}^{II-})(\mathbf{b})
\end{aligned}$$

From the equivalence of these two equations, the matrix \mathbf{b} is obtained.

$$\mathbf{b} = (\mathbf{b}_1)^{-1}(\mathbf{b}_2)(\mathbf{t}) \quad (4.21)$$

where \mathbf{b}_1 and \mathbf{b}_2 are defined as:

$$\begin{aligned}
\mathbf{b}_1 &= (\mathbf{C}^{II+})^{-1}(\mathbf{C}^{II-}) - (\mathbf{D}^{II+})^{-1}(\mathbf{D}^{II-}) \\
\mathbf{b}_2 &= (\mathbf{C}^{II+})^{-1}(\mathbf{C}^{III+}) - (\mathbf{D}^{II+})^{-1}(\mathbf{D}^{III+}).
\end{aligned}$$

From Equations. 4.20, the matrix \mathbf{b} is obtained as follows:

$$\begin{aligned}
\mathbf{b} &= (\mathbf{C}^{II-})^{-1}(\mathbf{C}^{III+})(\mathbf{t}) - (\mathbf{C}^{II-})(\mathbf{C}^{II+})(\mathbf{a}) \\
\mathbf{b} &= (\mathbf{D}^{II-})^{-1}(\mathbf{D}^{III+})(\mathbf{t}) - (\mathbf{D}^{II-})(\mathbf{D}^{II+})(\mathbf{a}).
\end{aligned}$$

From the equivalence of these two equations, the matrix \mathbf{a} is obtained.

$$\mathbf{a} = (\mathbf{a}_1)^{-1}(\mathbf{a}_2)(\mathbf{t}) \quad (4.22)$$

where \mathbf{a}_1 and \mathbf{a}_2 are defined as:

$$\begin{aligned}\mathbf{a}_1 &= (\mathbf{C}^{II-})^{-1}(\mathbf{C}^{II+}) - (\mathbf{D}^{II-})^{-1}(\mathbf{D}^{II+}) \\ \mathbf{a}_2 &= (\mathbf{C}^{II-})^{-1}(\mathbf{C}^{III+}) - (\mathbf{D}^{II-})^{-1}(\mathbf{D}^{III+}).\end{aligned}$$

According to the Equations. 4.20, the matrix \mathbf{r} can be written as

$$\mathbf{r} = (\mathbf{B}^{I-})^{-1}[(\mathbf{B}^{II+})(\mathbf{a}) + (\mathbf{B}^{II-})(\mathbf{b}) - (\mathbf{B}^{I+})]. \quad (4.23)$$

Substitution of the matrix \mathbf{a} and \mathbf{b} into the Equation. 4.24 leads to the matrix \mathbf{r} following:

$$\mathbf{r} = (\mathbf{r}_1)^{-1}(\mathbf{t}) - (\mathbf{r}_2), \quad (4.24)$$

where

$$\begin{aligned}\mathbf{r}_1 &= (\mathbf{B}^{I-})^{-1}[(\mathbf{B}^{II+})(\mathbf{a}_1)^{-1}(\mathbf{a}_2) + (\mathbf{B}^{II-})(\mathbf{b}_1)^{-1}(\mathbf{b}_2)] \\ \mathbf{r}_2 &= (\mathbf{B}^{I-})^{-1}(\mathbf{B}^{I+})\end{aligned}$$

As a consequence the transmission matrix \mathbf{t} is obtained as below:

$$\mathbf{t} = [(\mathbf{A}^{II+})(\mathbf{a}_1)^{-1}(\mathbf{a}_2) + (\mathbf{A}^{II-})(\mathbf{b}_1)^{-1}(\mathbf{b}_2) - (\mathbf{A}^{II-})(\mathbf{r}_1)]^{-1}[(\mathbf{A}^{I+}) - (\mathbf{A}^{I-})(\mathbf{r}_2)] \quad (4.25)$$

The transmission coefficients can be calculated by multiplying the components of matrix \mathbf{t} and normalized the wave amplitudes.

$$\tilde{t}_{n_I, \sigma_I; n_{III}, \sigma_{III}} = \frac{k_{n_{III}, \sigma_{III}}^+}{k_{n_I, \sigma_I}^+} t_{n_I, \sigma_I; n_{III}, \sigma_{III}} \quad (4.26)$$

The conductance of the system is obtained via Landauer-Büttiker formula (Kassubek et al., 1999),

$$G_{n_I, \sigma_I; n_{III}, \sigma_{III}} = \frac{e^2}{h} \int dE \frac{-\partial f(E)}{\partial E} (\tilde{t}_{n_I, \sigma_I; n_{III}, \sigma_{III}}(E))^* \tilde{t}_{n_I, \sigma_I; n_{III}, \sigma_{III}}(E), \quad (4.27)$$

where $f(E)$ is the Fermi distribution function defined as:

$$f(E) = \frac{1}{1 + e^{(E-E_F)/k_B T}}. \quad (4.28)$$

For low temperature limit $k_B T \ll E_F$, $E \approx E_F$ is assumed. The conductance between energy spin-split levels which are defined as + and – levels, can be written as:

$$G_{++} = G_{0,+;0,+} + G_{0,+;1,+} + \cdots + G_{1,+;0,+} + G_{1,+;1,+} + \cdots + G_{2,+;0,+} + G_{2,+;1,+} + \cdots,$$

$$G_{--} = G_{0,-;0,-} + G_{0,-;1,-} + \cdots + G_{1,-;0,-} + G_{1,-;1,-} + \cdots + G_{2,-;0,-} + G_{2,-;1,-} + \cdots,$$

$$G_{+-} = G_{0,+;0,-} + G_{0,+;1,-} + \cdots + G_{1,+;0,-} + G_{1,+;1,-} + \cdots + G_{2,+;0,-} + G_{2,+;1,-} + \cdots,$$

$$G_{-+} = G_{0,-;0,+} + G_{0,-;1,+} + \cdots + G_{1,-;0,+} + G_{1,-;1,+} + \cdots + G_{2,-;0,+} + G_{2,-;1,+} + \cdots.$$

Then the total conductance G is found to be

$$G = G_{++} + G_{--} + G_{+-} + G_{-+}. \quad (4.29)$$

4.2 Numerical Results

In this part of the thesis, we aimed to theoretically investigate the conductance of a QWR for different strengths of spin-orbit interactions, magnitude and orientations of magnetic field. We consider *InAs* bulk structure with the parameters: effective mass $m^* = 0.03$ and Lande-g factor $g^* = -15$. The length is scaled with harmonic oscillator length $l_0 = 20$ nm and the corresponding energies are obtained in $\hbar\omega_0 = 6.35$ meV units. We calculated the transmission amplitudes of an incident electron from region *I* to region *III*.

In Figure 4.2, we showed the calculated conductance of parabolic QWR as a function of Fermi energy in the presence of Rashba and Dresselhaus spin-orbit interactions. The subfigure a) presents the total conductance whereas b) and c) depict the spin-split level conductance. The Rashba and Dresselhaus spin-orbit coupling parameters are chosen as $\alpha_{R1} = 2$ meV nm and $\alpha_{D1} = 1$ meV nm for the first and third

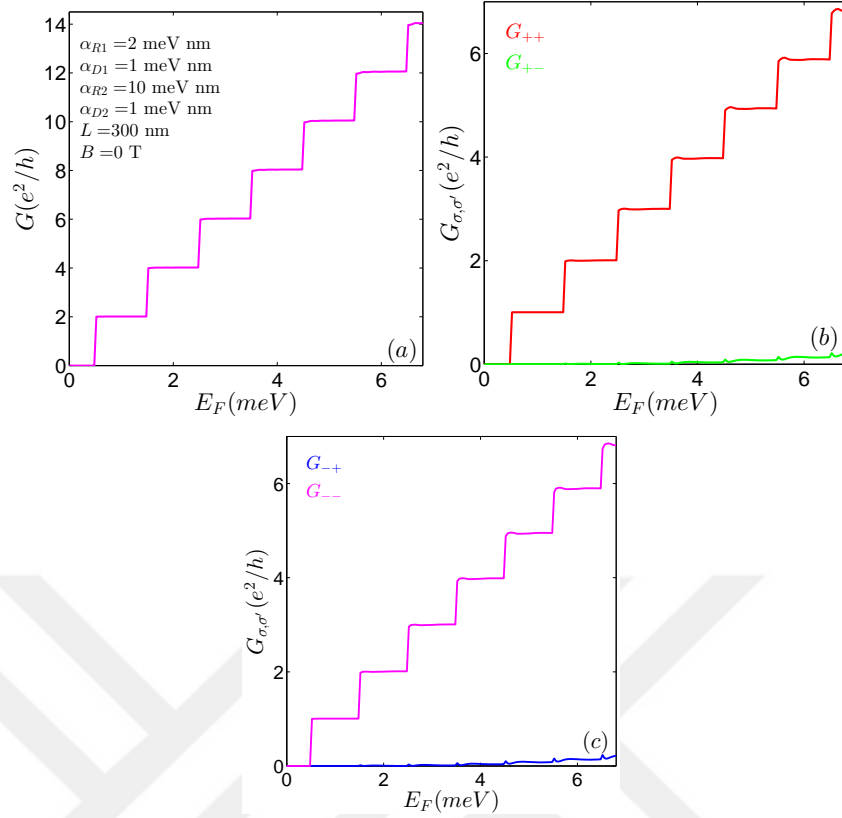


Figure 4.2 The calculated a) total, b) and c) spin-split energy levels conductance as a function of Fermi energy. The spin-orbit coupling parameters are chosen as: in the first and third region $\alpha_{R1} = 2$ meV nm, $\alpha_{D1} = 1$ meV nm and in the second region $\alpha_{R2} = 10$ meV nm, $\alpha_{D2} = 5$ meV nm. In all regions magnetic field is zero.

regions which are assumed identical. In the conductor, namely second region, these parameters are $\alpha_{R2} = 10$ meV nm, $\alpha_{D2} = 5$ meV nm. The magnetic field is zero in all regions. As expected, the total conductance exhibits an increasing stepwise profile by increasing amount of $2e^2/h$. This increment in the conductance can be explained via the components of conductance which are shown in Figure 4.2(b) and Figure 4.2(c). The transmission of an electron from region *I* with mode + transmitted to region *III* with mode + is remarked as G_{++} and with mode - is G_{+-} . Similarly, for the incident electron from region *I* with - mode transmitted to region *III* with mode - the conductance is G_{--} and G_{-+} is with mode +. As seen in subfigures the conductance G_{++} and G_{--} are more dominant than G_{+-} and G_{-+} . The components with incident same mode increase by an amount of (e^2/h) so the total conductance increases $(2e^2/h)$.

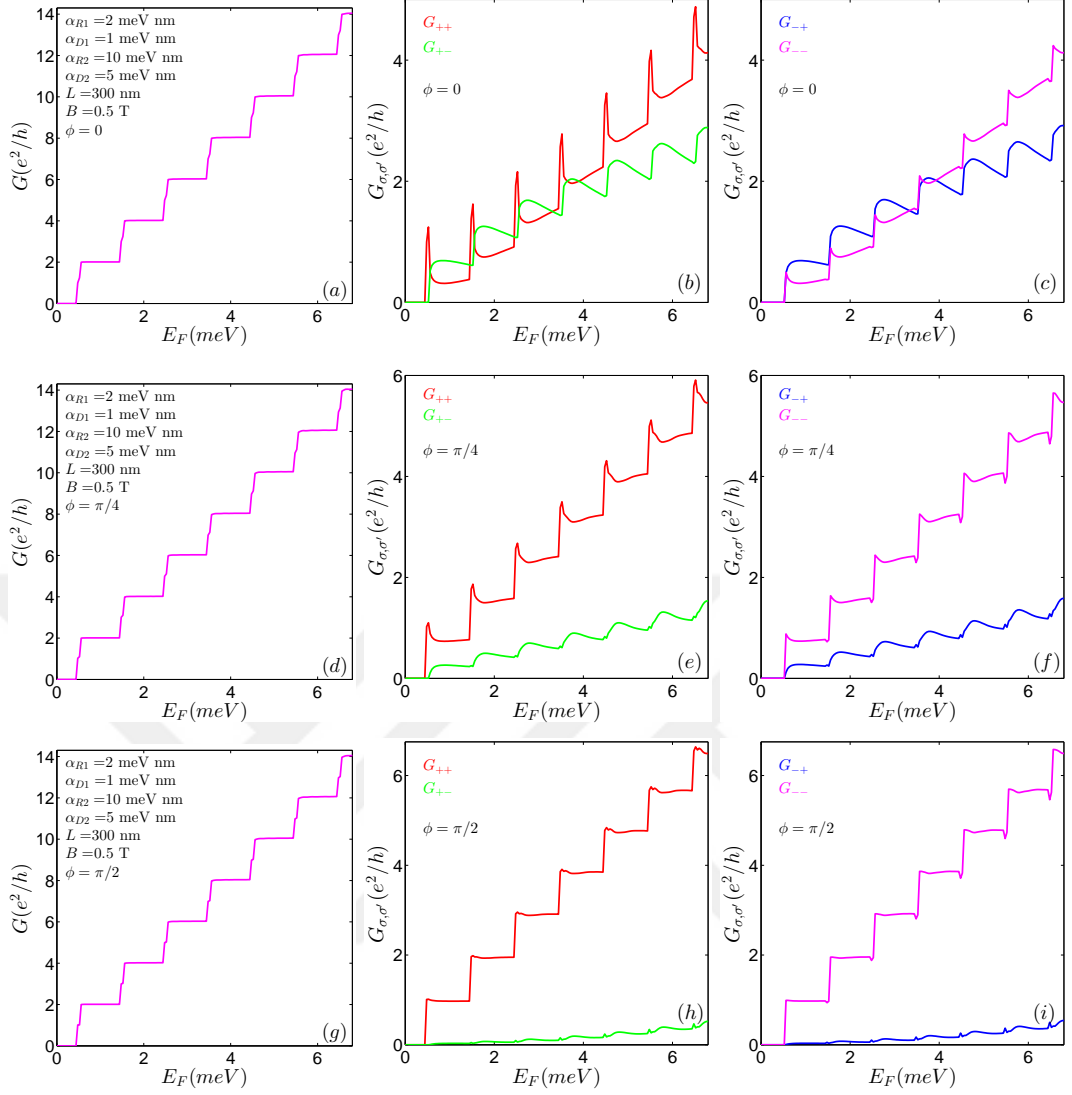


Figure 4.3 The energy spin-split levels conductance as a function of Fermi energy for three different orientations of a constant magnetic field (0.5 T) with the same spin-orbit coupling constants with Figure 4.2.

We turn to a study of effect of an external magnetic field on conductance in the presence of spin-orbit interactions. The spin-orbit coupling constants are chosen the same in with Figure 4.2 and the magnitude of the applied magnetic field is set $B = 0.5$ T. The total conductances for three different field orientations are presented in Figure 4.3(a) $\phi = 0$, (d) $\phi = \pi/4$ and (e) $\phi = \pi/2$. As expected the total conductances increase monotonically for all directions of magnetic field. When magnetic field is applied along the wire axis, the increment in the conductance is amount of $(2e^2/h)$. When the orientation of magnetic field differs from zero, the conductance exhibits an

increasing stepwise profile with integer conductance. There are breaking points at (e^2/h) with odd integers. The orientation of applied magnetic field strongly affects the wave functions of the QWR which constitute the elements of transmission matrices. And this effect can be seen in mode dependent components of conductance. It is clear from all subfigures that the all of mode dependent conductance increases with Fermi energy as expected. When magnetic field is applied along the x -direction, three components of conductance G_{+-} , G_{-+} and G_{--} are efficient and contributes to the total conductance same amount. G_{++} is more dominant than others and its contribution is larger than the others. When magnetic field is applied an angle with $\phi = \pi/4$, the transmission between different modes becomes weaker as shown in Figure 4.3(e) and Figure 4.3(f) with green and blue lines. The transmission of an electron from region I with mode + (-) to region III with mode + (-) is more dominant. The conductance exhibits more smooth behaviour compared the case $\phi = 0$. Finally, when the magnetic field is applied perpendicular to the wire axis, the G_{+-} and G_{-+} are smaller compared to G_{++} and G_{--} as illustrated in Figure 4.3(h) and Figure 4.3(i). The conductance of same modes G_{++} and G_{--} increases in stepwise manner. This observations demonstrate that, the conductance strongly depends on the orientation of magnetic field.

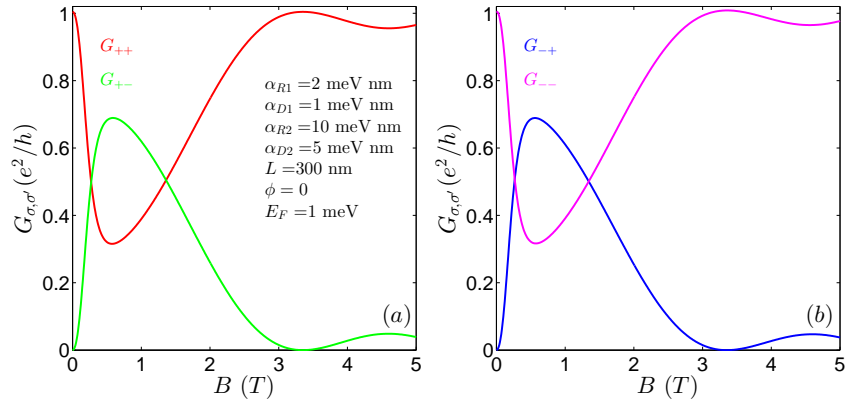


Figure 4.4 The calculated spin-split energy levels conductance a) G_{++} and G_{+-} , b) G_{-+} and G_{--} as a function of applied magnetic field along the wire axis. The spin-orbit coupling parameters are chosen as: in the first and third region $\alpha_{R1} = 2$ meV nm, $\alpha_{D1} = 1$ meV nm and in the second region $\alpha_{R2} = 10$ meV nm, $\alpha_{D2} = 5$ meV nm. The length of conductor is 300 nm and the Fermi energy is $E_F/(\hbar\omega_0) = 1$.

The magnetic field has an important effect on the properties of QWR systems. It leads to observe more complicated energy spectra, spin textures in the presence of

spin-orbit interactions as demonstrated in previous chapter. Therefore investigation of the variation of conductance with respect to the external magnetic field is noteworthy. For this purpose, Figure 4.4 is devoted to the illustrate the conductance as a function of magnetic field. The spin-orbit coupling constants are chosen as: in the first and third region $\alpha_{R1} = 2$ meV nm, $\alpha_{D1} = 1$ meV nm and in the second region $\alpha_{R2} = 10$ meV nm, $\alpha_{D2} = 5$ meV nm. The length of conductor is 300 nm and the Fermi energy is $E_F/(\hbar\omega_0) = 1$. When magnetic field is increased from zero to 0.74 T the same modes conductances G_{++} and G_{--} decreases whereas the different modes conductances G_{+-} and G_{-+} increase for this interval of magnetic field. After this value of magnetic field G_{++} and G_{--} rises with the increment of magnetic field and G_{+-} and G_{-+} decrease. After nearly 3 T, when conductance of the same modes decreases a little, the different modes conductances increase a little. They behave oppositely.

Another important system parameter is the length of the conductor. The total and the components of conductance are illustrated in Figure 4.5 for three lengths of conductor such as $L = 100, 200, 300$ nm. In identical regions *I* and *III* spin-orbit interactions are zero where as in region *II* the strength of Rashba and Dresselhaus spin-orbit couplings are chosen as $\alpha_{R2} = 10$ meV nm and $\alpha_{D2} = 5$ meV nm. The magnitude of magnetic field is 0.5 T and it is applied along the wire axis. The total conductance for all values of L increases stepwise with Fermi energy as depicted in Figures 4.5(a), (d) and (g). We see the effect of conductor length especially in the components of conductance. Figures 4.5(b), (c), (e), (f), (h) and (i) presents the same modes conductance and different modes conductance. When the conductor length is $L = 100$ nm, the same mode conductances G_{++} and G_{--} are larger than the different modes conductances G_{+-} and G_{-+} . With the increment of the conductor length ($L = 200$ nm), the different modes conductances rise and they get close to G_{++} and G_{--} . The length of the conductor is set $L = 300$ nm, the G_{+-} and G_{-+} are greater than G_{++} and G_{--} . At this value of length, the components behaves oppositely compared to the other length values. When the conductor length is increased, the corresponding wave functions changes their behaviours. So the elements of transmission matrix which are formed by the integration wave functions changes. This effect is observed in the components of

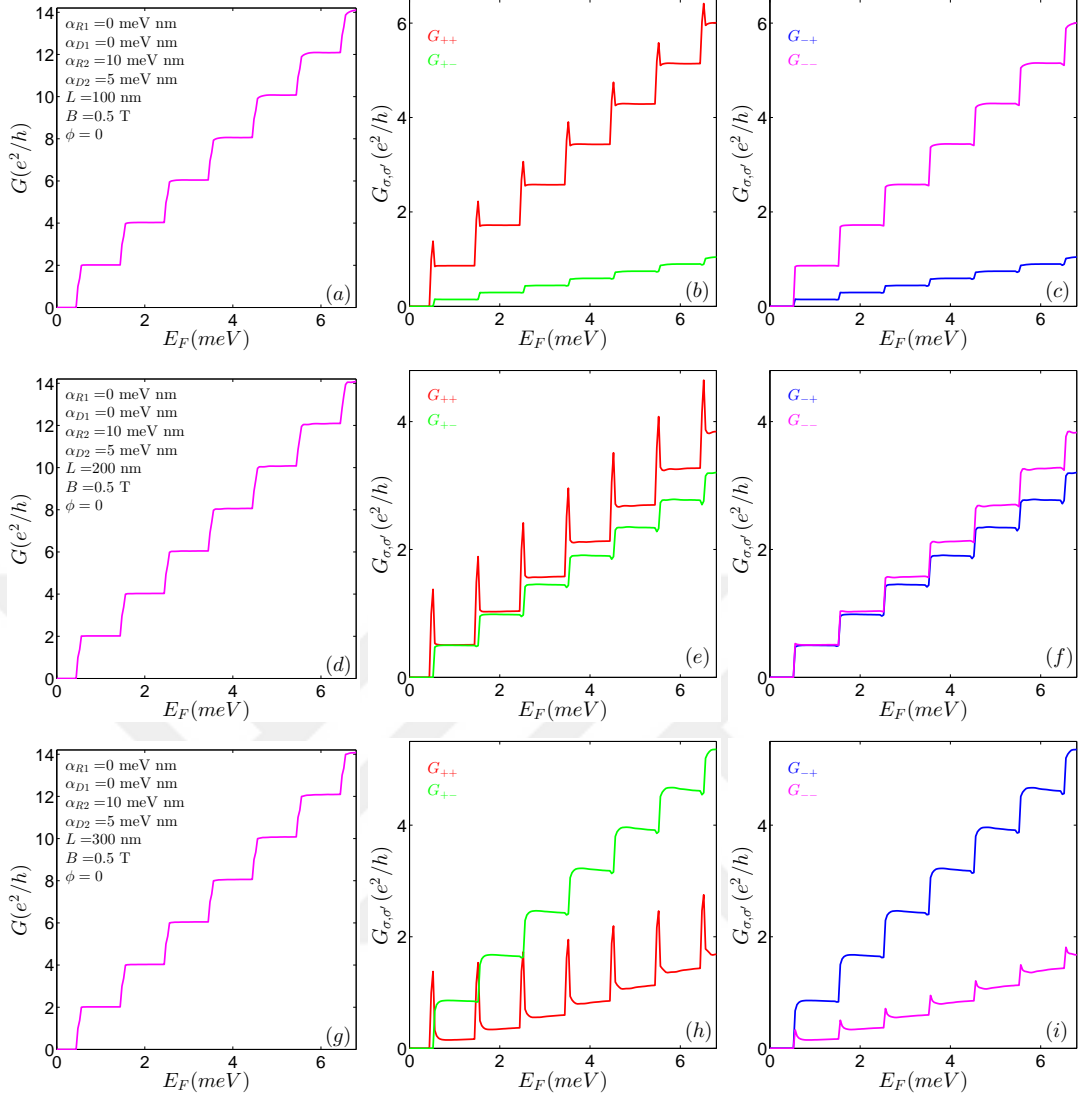


Figure 4.5 Conductance as a function of Fermi energy for three lengths of conductor $L = 100, 200, 300$ nm. The spin-orbit coupling is zero at identical regions and $\alpha_{R2} = 10$ meV nm and $\alpha_{D2} = 5$ meV nm are chosen in the conductor. The magnetic field with strength $B = 0.5$ T is applied along the wire axis in all regions.

conductance.

In Figure 4.6, we present the conductance as a function of conductor length for three different Fermi energies $E_F = 0.56, 1.55, 2.55$. In the region *I* and region *III* the spin-orbit is absent, in the conductor the strength of spin-orbit couplings are chosen as $\alpha_{R2} = 10$ meV nm and $\alpha_{D2} = 5$ meV. The external magnetic field $B = 0.5$ T is applied along the wire axis. When Fermi energy is set to $E_F/(\hbar\omega_0) = 0.56$, the number of subbands under the Fermi energy is one and it includes both + and - spin-split levels.

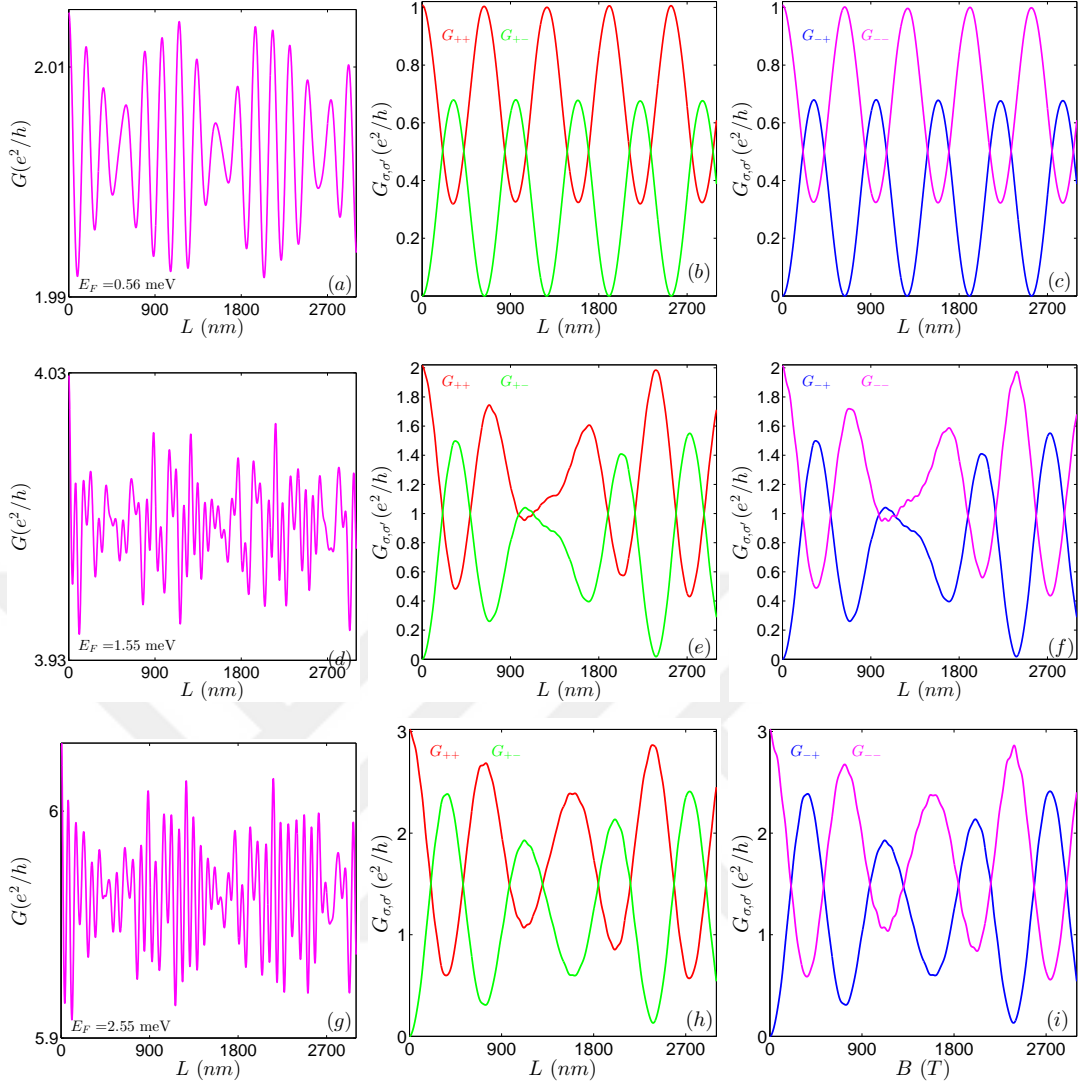


Figure 4.6 The total and mode dependent conductance as a function of conductor length for different Fermi energies $E_F/(\hbar\omega_0) = 0.56, 1.55, 2.55$. The spin-orbit interaction is zero in identical regions, in the conductor the strength of spin-orbit couplings are chosen as $\alpha_{R2} = 10$ meV nm and $\alpha_{D2} = 5$ meV. The magnetic field is $B = 0.5$ T and $\phi = 0$.

So the total conductance oscillates around $2(e^2/h)$ as shown in Figure 4.6(a). Both + and - states contributes the total conductance. The components of conductances G_{++} , G_{+-} , G_{-+} and G_{--} exhibit periodic behaviour with L as illustrated in Figure 4.6(b) and Figure 4.6(c). When Fermi energy is increased to $E_F/(\hbar\omega_0) = 1.55$, the number of subbands under the Fermi energy is two so the total conductance oscillates around $4(e^2/h)$ (Figure 4.6(d)). The components of conductance are presented in Figure 4.6(e) and (f). The periodic behaviour in the previous case breaks down. Lastly, we set Fermi

energy at 2.55 and it cuts three subbands. The total conductance is nearly $6e^2/h$ as seen in Figure 4.6(g). The mode dependent conductances exhibit more regular behaviour compared to the $E_F/(\hbar\omega_0) = 1.55$ case.

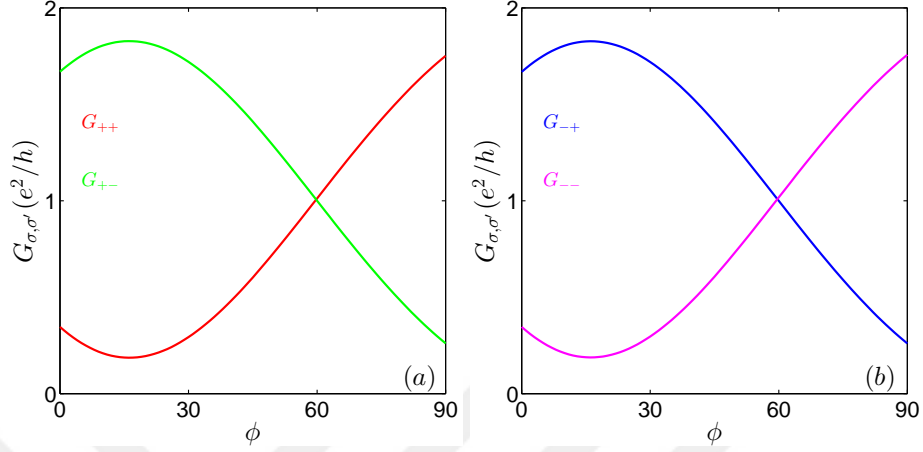


Figure 4.7 The calculated mode dependent conductance a) G_{++} and G_{+-} , b) G_{-+} and G_{--} as a function of orientation of magnetic field ($B = 0.5$ T). In region *I* and region *III*, the spin-orbit interaction is absent. The spin-orbit coupling parameters in the conductor are chosen as: $\alpha_{R2} = 10$ meV nm, $\alpha_{D2} = 5$ meV nm. The length of conductor is 300 nm.

The energies and the wave functions of the QWR are affected from the orientation of magnetic field. So it is useful to investigate the behavior of mode conductances as a function of orientation of magnetic field. We consider that the spin-orbit interactions are zero in region *I* and region *III* whereas they have a value in the second region such as $\alpha_{R2} = 10$ meV nm, $\alpha_{D2} = 5$ meV nm. The magnetic field is applied in the three regions. The Fermi energy is set 2 which cuts two states by including both + and - modes. The conductance of electrons with + modes transmitted to + and - modes is depicted in Figure 4.7(a). And the incident electron with - mode to - and + is illustrated in Figure 4.7(b). The different mode conductances are greater than the same modes conductance with the increment of angle until it takes nearly $\pi/3$. After that value when same modes conductances rise with the increment of angle, the different modes conductances decrease. Similar behavior is observed in Figure 4.3 for different orientations of magnetic field. The different modes conductances decrease for the larger value of ϕ and the same modes conductances ascend.

CHAPTER FIVE

CONCLUSION

In this thesis, we mainly aimed to investigate theoretically the energy spectrum, spin texturing, and zero-temperature ballistic conductance of double quantum wires formed by nonparabolically confinement of a two-dimensional electron gas. Emphasis has also been set on exploring the effects of an in-plane magnetic field on the energy dispersion, spin distribution and conductance by taking into account Rashba and Dresselhaus spin-orbit interactions and the presence of an external static electric field. Also we searched the effect of potential profile on the electronic and spin properties of double quantum wire. In this study the numerical calculations have been carried out with high accuracy by using a powerful Finite Elements Method which is based on Galerkin procedure.

We have studied the energy dispersion relations of the spin-split subbands for different cases such as different types of spin-orbit interaction, in the presence or absence of in-plane magnetic field and electric field. The energy subbands have showed two-fold degeneracy in the absence of Rashba and Dresselhaus spin-orbit interaction, magnetic and electric fields. Switching on spin-orbit interactions lifts the degeneracy between spin-split levels except the point $k_x = 0$. By applying an external magnetic field the time-reversal symmetry has been broken and the degeneracy has lifted all values of k_x . The electric field leads to a shift in the energy spectra. Also the energy spectra has showed intriguing properties for the different potential profile. In strong coupling limits, the tunneling effects are in action whereas in the weak coupling limits the energy subbands grouped are pairs and the wire behaves as two individual quantum wires.

The spin distributions of double quantum wire are searched for different situations. In the presence of spin-orbit interactions spin is not a good quantum number and it is possible to find spin textures across the wire with the spin direction depending on k_x and the wire transversal coordinate y . Spin textures are strongly dependent on the strength of Rashba and Dresselhaus spin-orbit interactions, the strength of electric and the strength and the orientation of magnetic field. We show that the combined effect of

spin-orbit coupling and magnetic field and electric field lead to a complicated energy spectra and affects significantly the spin texturing.

Moreover, we investigate the transport properties of double quantum wires for different potential profiles in the presence of spin-orbit couplings, magnetic/electric fields. The origin of the conductance oscillation is the local extremas in the subband structure. The depth and the width of the square conductance strongly depend on the strength of Rashba and Dresselhaus spin-orbit interactions, magnitude and direction of magnetic field and the strength of electric field, height and width of the double well potential.

Briefly, we found that the interplay of different spin-orbit couplings, magnetic and electric fields brings out the modification of the energy dispersion and consequently the conductance and phase shift between the modulations of the spin density components. Electrostatically modulated spin-orbit interaction and external magnetic/electric field in a quantum wire can be gainfully employed for the future design of spin-field effect transistors and spin filters, which rely on coherent spin transport.

In the other part of the thesis, we search the conductance of quantum wire confined by harmonic potential in the presence of Rashba and Dresselhaus spin-orbit interactions by considering effect of in-plane magnetic field. The conductance is calculated by transfer matrix method. We obtain both total conductance and mode dependent conductance as a function of Fermi energy, magnitude and orientation of magnetic field and the length of conductor. Our numerical results reveal that the total conductance exhibits stepwise profile as a function of Fermi energy for different strengths of spin-orbit interactions and magnetic field whereas the mode dependent conductances changes their behaviours depending on the internal mechanisms and external fields.

REFERENCES

- Alessandro, P. (2005). *Local manipulation of single electrons in semiconductor nanostructures*. PhD Thesis, Swiss Federal Institute of Technology, Zurich.
- Ashcroft, N. W., & Mermin, N. D. (1976). *Solid state physics*. USA: Saunders College Publishing.
- Balsa, R., Plo, M., Esteve, J. G., & Pacheco, A. F. (1983). Simple procedure to compute accurate energy levels of a double-well anharmonic oscillator. *Physical Review D*, 28, 1945–1948.
- Bandyopadhyaya, S., & Cahay, M. (2004). Alternate spintronic analog of the electro-optic modulator. *Applied Physics Letters*, 85, 1814.
- Banerjee, K., & Bhatnagar, S. P. (1978). Two-well oscillator. *Physical Review D*, 18, 4767–4769.
- Bender, C. M., & Wu, T. T. (1973). Anharmonic oscillator. ii. a study of perturbation theory in large order. *Physical Review D*, 7, 1620–1636.
- Bennett, C. H., & DiVincenzo, D. P. (2000). Quantum information and computation. *Nature (London)*, 404, 247.
- Bertoni, A., Bordone, P., Brunetti, R., Jacoboni, C., & Reggiani, S. (2000). Quantum logic gates based on coherent electron transport in quantum wires. *Physical Review Letters*, 84, 5912–5915.
- Bethe, H. A., & Salpeter, E. W. (1957). *Quantum mechanics of one and two electron atoms*. Berlin: Springer Verlag.
- Bhattacharya, S. K. (1985). Modified semiclassical quantization conditions for double minimum potentials: Applications to anharmonic oscillators. *Physical Review A*, 31, 1991–1998.
- Büttiker, M. (1986). Four-terminal phase-coherent conductance. *Physical Review Letters*, 57, 1761–1764.

- Büttiker, M., Imry, Y., Landauer, R., & Pinhas, S. (1985). Generalized many-channel conductance formula with application to small rings. *Physical Review B*, *31*, 6207–6215.
- Capasso, F., Mohammed, K., & Cho, A. (1986). Resonant tunneling through double barriers, perpendicular quantum transport phenomena in superlattices, and their device applications. *IEEE Journal of Quantum Electronics*, *22*, 1853.
- Datta, S. (1995). *Electronic transport in mesoscopic systems*. UK: Cambridge University Press.
- Datta, S., & Das, B. (1990). Electronic analog of the electro-optic modulator. *Applied Physics Letters*, *56*, 665.
- Debald, S., & Kramer, B. (2005). Rashba effect and magnetic field in semiconductor quantum wires. *Physical Review B*, *71*, 115322.
- der Straeten, E. V., & Naudts, J. (2006). The quantum double-well anharmonic oscillator in an external field. *Journal of Physics A: Mathematical and General*, *39*, 933.
- Dresselhaus, G. (1955). Spin-orbit coupling effects in zinc blende structures. *Physical Review*, *100*, 580–586.
- Edelstein, V. (1990). Spin polarization of conduction electrons induced by electric current in two-dimensional asymmetric electron systems. *Solid State Communications*, *73*, 233 – 235.
- Elzerman, J. M., Hanson, R., van Beveren, L. H. W., Witkamp, B., Vandersypen, L. M. K., & Kouwenhoven, L. P. (2004). Single-shot read-out of an individual electron spin in a quantum dot. *Nature London*, *430*, 431.
- Engels, G., Lange, J., Schäpers, T., & Lüth, H. (1997). Experimental and theoretical approach to spin splitting in modulation-doped $\text{In}_x\text{Ga}_{1-x}\text{As}/\text{InP}$ quantum wells for $B \rightarrow 0$. *Physical Review B*, *55*, R1958–R1961.

- Esaki, L., & Tsu, R. (1970). Superlattice and negative differential conductivity in semiconductors. *IBM Journal of Research and Development*, 14, 612.
- Ferry, D. K., Goodnick, S. M., & Bird, J. (2009). *Transport in nanostructures*. New York: Cambridge University Press.
- Fischer, S. F., Apetrii, G., Kunze, U., Schuh, D., & Abstreiter, G. (2006a). Energy spectroscopy of controlled coupled quantum-wire states. *Nature Physics*, 2, 91.
- Fischer, S. F., Apetrii, G., Kunze, U., Schuh, D., & Abstreiter, G. (2006b). Tunnel-coupled one-dimensional electron systems with large subband separations. *Physical Review B*, 74, 115324.
- Fowler, A. B., Fang, F. F., Howard, W. E., & Stiles, P. J. (1966). Magneto-oscillatory conductance in silicon surfaces. *Physical Review Letters*, 16, 901–903.
- Fulton, T. A., & Dolan, G. J. (1987). Observation of single-electron charging effects in small tunnel junctions. *Physical Review Letters*, 59, 109–112.
- Ganichev, S., Ivchenko, E., Bel'kov, V., Tarasenko, S., Sollinger, M., Weiss, D., et al. (2002). Spin-galvanic effect. *Nature(London)*, 417, 153.
- Gışı, B. (2012). *Electronic Structure of quantum wires with spin-orbit interactions under the influence of in-plane magnetic fields*. Master's thesis, Dokuz Eylül University, Turkey.
- Gisi, B., Karaaslan, Y., Sakiroglu, S., Kasapoglu, E., Sari, H., & Sokmen, I. (2016a). Effects of an in-plane magnetic field on the energy dispersion, spin texturing and conductance of double quantum wires. *Superlattices and Microstructures*, 91, 391.
- Gisi, B., Sakiroglu, S., & Sokmen, I. (2016b). Spin texturing in quantum wires with rashba and dresselhaus spin-orbit interactions and in-plane magnetic field. *Chinese Physics B*, 25, 017103.
- González, L., García, J. M., García, R., Briones, F., Martínez-Pastor, J., & Ballesteros, C. (2000). Influence of buffer-layer surface morphology on the self-organized growth of inas on inp(001) nanostructures. *Appl. Phys. Lett.*, 76, 1104.

- Governale, M., & Zülicke, U. (2002). Spin accumulation in quantum wires with strong rashba spin-orbit coupling. *Physical Review B*, *66*, 073311.
- Gudmundsson, V., & Tang, C.-S. (2006). Magnetotransport in a double quantum wire: Modeling using a scattering formalism built on the lippmann-schwinger equation. *Physical Review B*, *74*, 125302.
- Gujarathi, S., Alam, K. M., & Pramanik, S. (2012). Magnetic-field-induced spin texture in a quantum wire with linear dresselhaus spin-orbit coupling. *Physical Review B*, *85*, 045413.
- Handy, C. R. (1992). Application of the eigenvalue moment method to the quartic anharmonic double-well oscillator. *Physical Review A*, *46*, 1663–1666.
- Havu, P. (2005). *Modelling of electronic transport in nanostructures*. PhD Thesis, Laboratory of Physics Helsinki University of Technology, Finland.
- Hayamizu, Y., Yoshita, M., Watanabe, S., H. Akiyama, L., Pfeiffer, N., & West, K. W. (2002). Lasing from a single-quantum wire. *Applied Physics Letters*, *81*, 4937.
- Hodgson, R. J. W., & Varshni, Y. P. (1989). Splitting in a double-minimum potential with almost twofold degenerate lower levels. *Journal of Physics A: Mathematical and General*, *22*, 61.
- Hutton, D. V. (2004). *Fundamentals of finite element analysis*. New York: McGraw-Hill.
- Isailovic, N., Whitney, M., Patel, Y., Kubiawicz, J., Copsy, D., Chong, F. D., et al. (2004). Datapath and control for quantum wires. *ACM Transactions on Architecture and Code Optimization (TACO)*, *1*, 34–61.
- Jalil, M. B. A., Tan, S. G., & Fujita., T. (2008). Spintronics in 2deg systems. *Association of Asia Pacific Physical Societies Bulletin*, *18*, 9.
- Ji, L., & Miao, L. (dt). *Top-down techniques (lithography) for making quantum wires*. Retrieved May 20, 2017 from <http://www.ece.rochester.edu/courses/ECE580/>.

- Kapon, E., Hwang, D. M., & Bhat, R. (1989). Stimulated emission in semiconductor quantum wire heterostructures. *Physical Review Letters*, *63*, 430–433.
- Karaaslan, Y., Gisi, B., Sakiroglu, S., Kasapoglu, E., Sari, H., & Sokmen, I. (2015). Spin-orbit interaction and magnetic field effects on the energy dispersion of double quantum wire. *Superlattices and Microstructures*, *85*, 401–409.
- Karlsson, K. F., Weman, H., Dupertuis, M. A., Leifer, K., Rudra, A., & Kapon, E. (2004). Electroluminescence and photoluminescence excitation study of asymmetric coupled GaAs/Al_xGa_{1-x}As v-groove quantum wires. *Physical Review B*, *70*, 045302.
- Kasapoglu, E., Urgan, F., Sari, H., & Sokmen, I. (2009). Binding energies of donor impurities in modulation-doped double quantum wells under an electric field. *Superlattices and Microstructures*, *45*, 618–623.
- Kassubek, F., Stafford, C. A., & Grabert, H. (1999). Force, charge, and conductance of an ideal metallic nanowire. *Physical Review*, *59*, 7560–7574.
- Kato, Y. K., Myers, R. C., Gossard, A. C., & Awschalom, D. D. (2004). Current-induced spin polarization in strained semiconductors. *Physical Review Letters*, *93*, 176601.
- Könemann, J., Haug, R. J., Maude, D. K., Fal'ko, V. I., & Altshuler, B. L. (2005). Spin-orbit coupling and anisotropy of spin splitting in quantum dots. *Physical Review Letters*, *94*, 226404.
- Korepov, S. V., & Liberman, M. A. (1999). Transport properties of double quantum wires in a magnetic field. *Physical Review B*, *60*, 13770–13775.
- Krishna, S. (2005). Quantum dots-in-a-well infrared photodetectors. *Journal of Physics D: Applied Physics*, *38*, 2142.
- Kukushkin, V. A. (2009). Quantum dot-based tunable inversionless laser for the far infrared and terahertz ranges. *JETP Letters*, *89*, 437–440.

- Landauer, R. (1970). Electrical resistance of disordered onedimensional lattices. *Philosophical Magazine*, *21*, 863.
- Li, Y., Qian, F., Xiang, J., & Lieber, C. M. (2006). Nanowire electronic and optoelectronic devices. *Materials Today*, *9*, 18 – 27.
- Littman, M. G. (dt). *Zeeman and stark effects*. Department of Mechanical and Aerospace Engineering, Princeton Univerctiy.
- Lorenz, M., Gian, S., Ivan, S., Emilio, G., S., S., & E., K. (2007). Measurement of rashba and dresselhaus spin-orbit magnetic fields. *Nature Physics*, *3*, 650.
- Loss, D., & DiVincenzo, D. P. (1998). Quantum computation with quantum dots. *Physical Review A*, *57*, 120–126.
- Lucignano, P., Raimondi, R., & Tagliacozzo, A. (2008). Spin hall effect in a two-dimensional electron gas in the presence of a magnetic field. *Physical Review B*, *78*, 035336.
- Lyo, S. K., & Huang, D. (2001). Multisublevel magnetoquantum conductance in single and coupled double quantum wires. *Physical Review B*, *64*, 115320.
- Majumdar, A., Manquest, N., Faraon, A., & Vukovic, J. (2010). Theory of electro-optic modulation via a quantum dot coupled to a nano-resonator. *Optics Express*, *18*, 3974.
- Malet, F., Pi, M., Barranco, M., Serra, L., & Lipparini, E. (2007). Exchange-correlation effects on quantum wires with spin-orbit interactions under the influence of in-plane magnetic fields. *Physical Review B*, *76*, 115306.
- Manchon, A., Koo, H. C., Nitta, J., Frolov, S. M., & Duine, R. A. (2015). New perspectives for rashba spin-orbit coupling. *Nature Materials*, *14*, 871.
- Marsh, A. C., & Inkson, J. C. (1986). The electronic properties of GaAs/AlGaAs heterojunctions. *IEEE Journal of Quantum Electronics*, *QE22*, 86.

- Martin, T. P., Szorkovszky, A., Micolich, A. P., Hamilton, A. R., Marlow, C. A., Linke, H., et al. (2008). Enhanced zeeman splitting in $\text{Ga}_{0.25}\text{In}_{0.753}\text{As}$ quantum point contacts. *Applied Physics Letters*, *93*, 012105.
- Meijer, F. E. (2005). *Rashba spin-orbit interaction in mesoscopic systems*. PhD Thesis, Technische Universiteit Delft, Australia.
- Meir, Y., Wingreen, N. S., & Lee, P. A. (1991). Transport through a strongly interacting electron system: Theory of periodic conductance oscillations. *Physical Review Letters*, *66*, 3048–3051.
- Miller, D. A. B. (1990). Quantum well optoelectronic switching devices. *International Journal of High Speed Electronics and Systems*, *1*, 19.
- Moon, J. S., Blount, M. A., Simmons, J. A., Wendt, J. R., Lyo, S. K., & Reno, J. L. (1999). Magnetoresistance of one-dimensional subbands in tunnel-coupled double quantum wires. *Physical Review B*, *60*, 11530–11534.
- Moroz, A. V., & Barnes, C. H. W. (1999). Effect of the spin-orbit interaction on the band structure and conductance of quasi-one-dimensional systems. *Physical Review B*, *60*, 14272–14285.
- Nitta, J., Akazaki, T., Takayanagi, H., & Enoki, T. (1997). Gate control of spin-orbit interaction in an inverted $\text{In}_{0.53}\text{Ga}_{0.47}\text{As}/\text{In}_{0.52}\text{Al}_{0.48}\text{As}$ heterostructure. *Physical Review Letters*, *78*, 1335–1338.
- Papageorgiou, C., Raptis, A., & Simos, T. (1990). A method for computing phase shifts for scattering. *Journal of Computational and Applied Mathematics*, *29*, 61 – 67.
- Park, Y. H., Kim, H., Chang, H., Han, S. H., Eom, H., J. and Choi, et al. (2013). Separation of rashba and dresselhaus spin-orbit interactions using crystal direction dependent transport measurements. *Applied Physics Letters*, *103*, 252407.
- Pedram, P., Mirzaei, M., & Gousheh, S. S. (2010). Accurate energy spectrum for double-well potential: periodic basis. *Molecular Physics*, *108*, 1949–1955.

- Pershin, Y. V., Nesteroff, J. A., & Privman, V. (2004). effect of spin-orbit interaction and in-plane magnetic field on the conductance of quasi-one-dimensional system. *Physical Review B*, *69*, 121306(R).
- Petroff, P. M., Gossard, A. C., Logan, R. A., & Wiegmann, W. (1982). Toward quantum well wires: Fabrication and optical properties. *Applied Physics Letters*, *41*, 635.
- Pfeiffer, L., West, K. W., Stormer, H. L., Eisenstein, J. P., Baldwin, K. W., Gershoni, D., et al. (1990). Formation of a high quality two-dimensional electron gas on cleaved GaAs. *Applied Physics Letters*, *56*, 1697.
- Piccinin, S. (2006). *Theoretical modelling of electronic transport in molecular devices*. PhD Thesis, Princeton university, United States.
- Porgilsson, G. (2012). *Modeling transport through semiconductor nanostructures with Rashba spin-orbit interaction*. PhD Thesis, University of Iceland, Iceland.
- Pramanik, S., Bandyopadhyay, S., & Cahay, M. (2007). Energy dispersion relations of spin-split subbands in a quantum wire and electrostatic modulation of carrier spin polarization. *Physical Review B*, *76*, 155325.
- Ram-Mohan, L. R. (2002). *Finite element and boundary element applications in quantum mechanics*. Oxford: Oxford University Press.
- Rashba, E. I. (1960). Properties of semiconductors with an extremum loop. 1. cyclotron and combinational resonance in a magnetic field perpendicular to the plane of the loop. *Soviet Physics Solid State*, *2*, 580–586.
- Reddy, J. N. (1993). *An introduction to the finite element method*. McGraw-Hill.
- Reed, M. A., Zhou, C., Muller, C. J., Burgin, T. P., & Tour, J. M. (1997). Conductance of a molecular junction. *Science*, *278*, 252–254.
- Sakurai, J. J. (1967). *Advanced quantum mechanics*. Wesley: Addison.
- Saravanan, S., John Peter, A., & Lee, C. W. (2015). Combined effects of magnetic and electric fields on the interband optical transitions in InAs/InP quantum wire. *Physica E: Low-dimensional Systems and Nanostructures*, *67*, 99–104.

- Sarikurt, S. (2013). *Electronic structure of parabolic confining quantum wires with Rashba and Dresselhaus spin-orbit coupling in a perpendicular magnetic field*. PhD Thesis, Dokuz Eylül University, Turkey.
- Sarikurt, S., Sakiroglu, S., Akgungor, K., & Sokmen, I. (2014). Spin texturing in a parabolically confined quantum wire with rashba and dresselhaus spin-orbit interactions. *Chinese Physics B*, 23, 017102.
- Scheid, M., Kohda, M., Kunihashi, Y., Richter, K., & Nitta, J. (2008). All-electrical detection of the relative strength of rashba and dresselhaus spin-orbit interaction in quantum wires. *Physical Review Letters*, 101, 266401.
- Schöll, E. (1998). *Theory of transport properties of semiconductor nanostructures*. UK: Chapman and Hall.
- Serra, L., Sánchez, D., & López, R. (2005). Rashba interaction in quantum wires with in-plane magnetic fields. *Physical Review B*, 72, 235309.
- Shi, J.-R., & Gu, B.-Y. (1997). Magnetoconductance oscillations of two parallel quantum wires coupled through a potential barrier. *Physical Review B*, 55, 9941–9948.
- Sidor, Y. (2007). *Theoretical study of excitons in semiconductor quantum wires and related systems*. PhD Thesis, Universiteit Antwerpen, Antwerpen.
- Simos, T. E., & Raptis, A. D. (1990). Numerov-type methods with minimal phase-lag for the numerical integration of the one-dimensional schrödinger equation. *Computing*, 45, 175–181.
- Smit, R. H. M., Noat, Y., Untiedt, C., Lang, N. D., van Hemert, M. C., & van Ruitenbeek, J. M. (2002). Measurement of the conductance of a hydrogen molecule. *Nature*, 419, 906.
- Suárez, F., Fuster, D., González, L., González, Y., García, J. M., & Dotor, M. L. (2006). Self-assembled inas quantum wire lasers on (001)inp at 1.6. *Applied Physics Letters*, 89, 091123.

- Sun, H. (1998). Electronic states of v-shaped semiconductor quantum wires in electric fields. *Physical Review B*, 58, 15381–15384.
- Sze, S. M. (1981). *Physics of semiconductor devices*. New York: Wiley.
- Thomas, K. J., Nicholls, J. T., Simmons, M. Y., Tribe, W. R., Davies, A. G., & Pepper, M. (1999). Controlled wave-function mixing in strongly coupled one-dimensional wires. *Physical Review B*, 59, 12252–12255.
- Tipler, P. A., & Llewellyn, R. A. (2008). *Modern physics*. New York: W. H. Freeman and Company.
- Upadhyaya, P., Pramanik, S., & Bandyopadhyay, S. (2008a). Magnetic field effects on spin texturing in a quantum wire with rashba spin-orbit interaction. *Physical Review B*, 77, 045306.
- Upadhyaya, P., Pramanik, S., & Bandyopadhyay, S. (2008b). Optical transitions in a quantum wire with spin-orbit interaction and its applications in terahertz electronics: Beyond zeroth-order theory. *Physical Review B*, 77, 155439.
- Vaseghi, B., Khordad, R., & Golshan, M. M. (2006). Dynamical properties of spin and subbands populations in 1d quantum wire. *Physica Status Solidi B*, 243, 2772.
- Wagner, R. (2009). *G-factor, effective mass and spin susceptibility of a 2-dimensional electron gas*. Master's thesis, University of Basel, Switzerland.
- Wang, D. W., Mishchenko, E. G., & Demler, E. (2005). Pseudospin ferromagnetism in double-quantum-wire systems. *Physical Review Letters*, 95, 086802.
- Wang, X. F. (2004). Spin transport of electrons through quantum wires with a spatially modulated rashba spin-orbit interaction. *Physical Review B*, 69, 035302.
- Wegscheider, W., Pfeiffer, L. N., Dignam, M. M., Pinczuk, A., West, K. W., McCall, S. L., et al. (1993). Lasing from excitons in quantum wires. *Physical Review Letters*, 71, 4071–4074.

- Witwit, M. (1996). Energy levels for nonsymmetric double-well potentials in several dimensions: Hill determinant approach. *Journal of Computational Physics*, 123, 369 – 378.
- Wolf, S. A., Awschalom, D. D., Buhrman, R. A., Daughton, J. M., von Molnar, S., Roukes, M. L., et al. (2001). Spintronics: A spin-based electronics vision for the future. *Science*, 294, 1488.
- Wrinkler, R. (2003). *Spin-orbit coupling effects in two dimensional electron and hole systems*. New York: Springer.
- Yamamoto, M., Tokura, Y., Hirayama, Y., Stopa, M., Ono, K., & Tarucha, S. (2005). Tunneling between parallel quantum wires. *AIP Conference Proceedings*, 772, 925.
- Yu, P. Y., & Cardona, M. (2010). *Fundamentals of semiconductors: Physics and materials properties*. Berlin: Springer.
- Zhang, L., Brusheim, P., & Xu, H. Q. (2005). Multimode electron transport through quantum waveguides with spin-orbit interaction modulation: Applications of the scattering matrix formalism. *Physical Review B*, 72, 045347.
- Zhang, S., Liang, R., Zhang, E., Zhang, L., & Liu, Y. (2006). Magnetosubbands of semiconductor quantum wires with rashba and dresselhaus spin-orbit coupling. *Physical Review B*, 73, 155316.
- Zhang, T. Y., Zhao, W., & Liu, X. M. (2009). Energy dispersion of the electrosubbands in parabolic confining quantum wires: interplay of Rashba, Dresselhaus, lateral spin-orbit interaction and the zeeman effect. *Journal of Physics: Condensed Matter*, 21, 335501.
- Zienkiewicz, O., Taylor, R., & Zhu, J. (2005). *Finite element method: its basis and fundamentals*. Heinemann: Elsevier Butterworth.